

CHARGED KAON PRODUCTION
IN
TAU LEPTON DECAYS

Thesis by
Geoffrey Blount Mills

In Partial Fulfillment of the Requirements
for the Degree of
Doctor of Philosophy

California Institute of Technology
Pasadena, California

1986

(Submitted June 12, 1985)

Acknowledgements

This work is the product of the efforts of many people. I will attempt to list everyone who was involved to the best of my recollection, but, in case I have omitted anyone, it is not intentional.

Firstly, I would like to express my warm thanks to every member of the DELCO collaboration, who have all devoted time and effort in varying degrees toward making this work possible. They were: W. B. Atwood, P. H. Baillon, B. C. Barish, A. Courau, H. DeStaebler, G. J. Donaldson, R. Dubois, M. M. Duro, E. E. Elsen, S. G. Gau, Y. Z. Huang, G. M. Irwin, R. P. Johnson, H. Kichimi, J. Kirkby, D. E. Klem, D. E. Koop, J. Ludwig, A. Ogawa, D. Perret-Galix, R. Pitthan, D. L. Pollard, C. Y. Prescott, L. Z. Rivkin, L. S. Rochester, W. Ruckstuhl, M. Sakuda, S. S. Sherman, E. J. Siskind, R. Stroynowski, D. Taylor, S. Q. Wang, S. G. Wojcicki, H. Yamamoto, W. G. Yan, and C. C. Young.

Secondly, I would like to acknowledge the invaluable support of the technical staffs of SLAC groups A and G and the technical staff of CalTech without whom this work would not have been possible. They were: B. Bricaud, A. Johnston, O. Saxton, S. Sund, J. Zingheim, D. Chambers, D. Ouimette, C. Pierce, D. Porat, M. Susskind, A. Tillman, R. Cooper, L. Cronk, R. Decker, H. Grau, J. Hanson, L. Mossbarger, D. Sell, S. Sondergaard, and J. Ungerer.

Thirdly, I would like to thank J. Bressler, L. Sartain, and P. Dearborn for their secretarial efforts which were greatly appreciated.

Fourthly, I would like to thank my advisor, Dr. Barry Barish, for steering me on a proper course, by making sure that I did not wander too far astray and for seeing my graduate student career through to its finish.

Lastly and most importantly, I would like to thank my family and my friends for providing the tremendous support which was needed to complete this work, especially my loving wife, Ellen, who has stood by me through all of my efforts.

Abstract

The result of an experiment performed at the PEP e^+e^- storage ring which operated at $29.0 \text{ GeV}/c^2$ is presented. The DELCO detector, which emphasizes Cherenkov particle identification, is used to measure the production of charged kaons in τ decays. The branching ratio of the Cabibbo-suppressed decays $b(\tau^\pm \rightarrow K^\pm \nu_\tau) = (0.57 \pm 0.15)\%$, $b(\tau^\pm \rightarrow K^\pm \nu_\tau + n\pi^0) = (1.59 \pm 0.23)\%$ $n \geq 0$, and $b(\tau^\pm \rightarrow K^\pm \pi^+ \pi^- \nu_\tau (\pi^0)) = (0.22^{+0.16}_{-0.13})\%$ are measured, and the branching ratio of the Cabibbo-favored decay $b(\tau^\pm \rightarrow K^+ K^- \pi^\pm \nu_\tau) = (0.22^{+0.17}_{-0.11})\%$ is measured. These branching ratio measurements provide a test $e - \mu - \tau$ universality and are in agreement with and the predictions of $SU(3)$ sum rules. The invariant mass distribution of the $K^+ K^- \pi$ system in the exclusive $\tau^\pm \rightarrow K^+ K^- \pi^\pm \nu_\tau$ channel is used to set a limit of $157 \text{ MeV}/c^2$ at 95% CL on the τ neutrino mass.

Table of Contents

Acknowledgements	ii
Abstract	iii
Table of Contents	iv
List of Tables	vii
List of Figures	viii
Chapter 1. Introduction	1
Chapter 2. Properties of the τ Lepton	4
2.1 e^+e^- Physics	4
2.2 QED Reactions	5
2.3 Decays of the τ Lepton	11
2.4 Other Processes	18
2.4.1 Hadron Production	18
2.4.2 Two Photon Processes	19
Chapter 3. Apparatus	21
3.1 Environment	22
3.2 The DELCO Detector	24
3.2.1 Spectrometer	25
3.2.2 Tracking Chambers	27
3.2.3 Central Chambers	29
3.2.4 Outer Drift Chambers	36
3.2.5 Drift Chamber Electronics	42
3.2.6 Cherenkov Counter	45
3.2.7 Barrel Shower Counters	47
3.2.8 Time of Flight Counters	50
3.2.9 Pole-tip Shower Counters	53
3.2.10 Luminosity Monitors	55
3.2.11 Trigger	57

3.2.12	Data Acquisition and Online Monitoring	59
3.2.13	Offline Software	61
Chapter 4.	Analysis of the Data	63
4.1	The Data	64
4.1.1	Luminosity Measurement	65
4.2	Event Selection Overview	67
4.3	Kaon Identification	72
4.3.1	Cherenkov Acceptance and Efficiency	73
4.3.2	Track Quality and Momentum Resolution	78
4.4	Single Prong Decays	82
4.4.1	Single Prong Data Selection	84
4.4.2	Backgrounds	88
4.4.3	Single Prong Branching Ratios	94
4.5	Multi Prong Decays	99
4.5.1	Multi-Prong Data Selection	99
4.5.2	Multi Prong Branching Ratios	105
4.5.3	Determination of an Upper Bound on m_{ν_τ}	108
Chapter 5.	Results and Conclusion	121
5.1	Decays Involving the Pseudoscalars π and K	122
5.2	Multiprong Decays	129
5.3	The τ Neutrino Mass	134
5.3.1	The $\tau^\pm \rightarrow K^+ K^- \pi^\pm \nu_\tau$ Decay	134
5.3.2	Cosmological Implications	136
5.3.2.1	Neutrino Decays	139
5.3.2.2	Cosmological Constraints	140
5.4	Conclusion	144
Appendix A.	$e^+e^- \rightarrow \tau^+\tau^-$	145
A.1	$\tau^+\tau^-$ Production	145

A.2	The τ Decay Rate	146
A.3	Radiative Corrections	148
A.4	Monte Carlo Event Generation	150
REFERENCES		153

List of Tables

1	τ Decays	15
2	PEP Parameters	24
3	Drift Chamber Resolutions	35
4	Event Triggers	59
5	Luminosities	67
6	First Pass Selection	71
7	Cherenkov Threshold	74
8	Track Quality Selection	79
9	Wire Hit Distribution	80
10	Track Quality Efficiencies	86
11	Event Selection Efficiencies	87
12	Multi-prong Track Quality	102
13	Multi-prong Kaon Identification Efficiencies	104
14	Multi-prong Event Efficiencies	105
15	Multi-prong Background	105
16	Multi-prong Data	106
17	Multi-prong Event Efficiencies	107
18	Universality Measurements	126
19	Spectral Functions	130
20	K^* Backgrounds	133
21	Resonance Branching Ratio	134
22	Monte Carlo Branching Ratios	152

List of Figures

1	QED Diagrams	7
2	Bhabha Cross Section	9
3	$\mu^+\mu^-$ Cross Section	10
4	Electron Momentum Distribution	13
5	$R_{\tau+\tau^-}$	14
6	Generated Kaon Momenta	16
7	Hadron Production Diagrams	20
8	The PEP Ring	23
9	The DELCO Detector	26
10	Magnetic Field Map	28
11	The $\frac{1}{p}$ Distribution for Bhabha Events	30
12	Drift Chamber Cells	32
13	Electron Drift Trajectories	33
14	Drift Chamber Residual Distribution	34
15	Planar Chamber Layout	37
16	PDC Cell Structure	39
17	PDC Potential Map	40
18	PDC Electric Field and Drift Velocity	41
19	PDC Preamp Circuit	43
20	PDC Data Acquisition	44
21	Cherenkov Optics	46
22	Phototube Assembly	48
23	Cherenkov Pulse Height Distribution	49
24	BSH Counter	51
25	Barrel Shower Counter Response	52
26	TOF Timing Resolution	54
27	Luminosity Counter Schematic	56

28	The Data Acquisition System	60
29	QED Angular Distributions	68
30	QED Acolinearity	69
31	P.E. vs p	76
32	P.E. vs $\cos\theta$	77
33	$\mu^+\mu^-$ Resolution	81
34	Pion Attenuation	83
35	The Opposite Jet Multiplicity	89
36	$\cos\theta$ and Charged Energy Distributions	90
37	Kaon Momentum Distributions	91
38	N_{opp} Distribution	93
39	$\frac{1}{p}$ Distribution	95
40	Shower Counter Pulseheight	97
41	Multi-prong $\frac{1}{p}$	103
42	Branching Ratio Likelihood	109
43	Misidentification Probability	112
44	Event 1	113
45	Event 2	114
46	Event 3	115
47	Event 4	116
48	τ Decay Rate	117
49	Event Mass Resolutions	119
50	Universality	123
51	Pseudoscalar Universality	127
52	$\rho(1600)$ and CVC	137
53	$\rho(1580)$ Decay Rate	138
54	Neutrino Decay Diagrams	141
55	Limits on Neutrino Masses	142

Chapter 1. Introduction

The discovery of the τ lepton in 1975¹ led to a new view of the theory of quarks and leptons. The fact that there were now three generations of leptons meant that a third generation of quarks could be expected to be found. The first member of this generation was soon to be discovered at Fermilab² in a proton beam dump experiment. The studies of the τ lepton have centered around verifying that it is indeed a sequential lepton³ a fact which has been born out experimentally. An obvious next step in studying the decays of the τ lepton is to use them as a tool to test our concepts of universality of the weak interactions. Since the τ particle is a simple system and is the only lepton which is able to decay into hadrons, it provides a unique setting in which to study interactions of the lepton current with the hadronic currents. It has not yet been possible to observe τ production in hadron beams or neutrino beams. This implies that the only means of studying the τ is via the reaction $e^+e^- \rightarrow \tau^+\tau^-$.

The discovery of the τ was made in e^+e^- collisions at beam energies just above the mass of the τ of $1.784 \text{ GeV}/c^2$. Because of this the background from regular hadron production was relatively large. The event multiplicities for hadronic events were rather low and precluded the study of tau decays with more than one charged track. The $\tau^+\tau^-$ events were selected by requiring that there be a charged lepton in the event from one of the τ 's produced in the reaction. This led to a relatively low efficiency for selecting events from the $e^+e^- \rightarrow \tau^+\tau^-$ sample.

The data used in this thesis were recorded at a beam energy of $14.5 \text{ GeV}/c^2$,

well above the threshold for $\tau^+\tau^-$ production. This allowed for the separation of $\tau^+\tau^-$ events from hadronic events on a topological (*e.g.*, multiplicity) basis with high efficiency in the selection procedure. The increased production energy of the τ 's in the lab frame meant that the decay products were also at higher energy. This enabled the use of a Cherenkov counter system for the separation of charged π 's and K 's in the decays. In this respect the DELCO (an acronym for Direct Electron Counter) experiment, which was used to collect the data used in this thesis, was unique from all other detectors in the field⁴.

The Cherenkov counter in the DELCO experiment made possible the measurement of decay modes containing charged kaons. The relatively large momentum range over which kaons could be separated from pions meant good efficiency for event selection for a number of decay modes. The modes containing charged kaons have not yet been explored thoroughly and this thesis represents the first attempt to do so. With the exception of a measurement of the $\tau^\pm \rightarrow K^\pm \nu_\tau$ channel⁵, which suffered from large systematic and statistical errors, these channels remained unexplored.

Another aspect of the τ lepton which remains uncertain experimentally is the partner of the τ , *viz.*, the τ neutrino ν_τ . There are, of course, many interesting properties which should be determined regarding the ν_τ . The only one which has been experimentally accessible thus far is the neutrino mass, m_{ν_τ} . The mass of the τ neutrino has not yet been determined. For that matter, no neutrinos have been found to have a nonzero mass with the exception of a controversial result from Lubimov et al.⁶. This question remains to be settled, but for the moment it can be ignored. The history of mass limits on the τ neutrino started with a $250 \text{ MeV}/c^2$ limit⁷ which used the shift in the electron momentum distribution due to a finite neutrino mass but assumed a V-A interaction between the leptonic currents. At PEP, where it is possible to study the τ multi-prong decays, the decay $\tau^\pm \rightarrow \rho^\pm(1580)\nu_\tau \rightarrow 3\pi\pi^0\nu_\tau$ provided a limit of $164 \text{ MeV}/c^2$. The end point of the invariant mass distribution was used to limit the neutrino mass. In this thesis

a similar technique was used to set a better limit on the neutrino mass using the $\tau^\pm \rightarrow K^+ K^- \pi^\pm \nu_\tau$ channel.

This document is organized into five chapters, the first of which you are reading now. In the second chapter an effort is made to give an overview of the status of the τ lepton theoretically and experimentally. The history of e^+e^- colliding beam physics is discussed briefly followed by a discussion of τ decays and the production of $\tau^+\tau^-$ pairs in e^+e^- beams.

The third chapter deals with the DELCO detector apparatus used to observe and record the data. A discussion of both the hardware and the software aspects of the detector, data acquisition, and offline analysis systems is presented.

The analysis of the data, its selection and the measurements made, are the subject of Chapter 4. There are three separate topics in the chapter. The first is the τ decays which contain a single charged kaon with possibly other neutral particles present such as the τ neutrino. Next come the three charged particle decays that have an identified kaon present in the decay. Finally, the neutrino mass limit using the exclusive $\tau^\pm \rightarrow K^+ K^- \pi^\pm \nu_\tau$ decay mode is discussed.

The last chapter casts the measurements presented in Chapter 4 in terms of the theoretical predictions and attempts to determine what has been learned with regard to the fundamental properties of nature.

Chapter 2. Properties of the τ Lepton

In this chapter the general setting regarding the physics of e^+e^- collisions will be discussed. There will be an emphasis on the production and decay to τ leptons, the main subject of this thesis. In addition there will be a discussion of some other physical processes which are useful in calibration of equipment, luminosity measurements, and in determining backgrounds.

§2.1 e^+e^- Physics

The history of e^+e^- colliding beam physics began in the 1950's when the concept of e^+e^- colliding beam machines was first envisioned⁸. The development of such machines did not occur until the 1960's. The first physics to come from such machines concerned the reactions⁸ $e^+e^- \rightarrow e^+e^-$, $\mu^+\mu^-$, and $\pi\pi$ which were feasible in the energy range of the early machines.

In the late 1960's it was proposed that a higher energy e^+e^- machine be developed. This project was eventually approved and constructed at the Stanford Linear Accelerator Center where an already existing linear electron accelerator served as the injector to the ring. This project, called the SPEAR project, became

operational in the early 1970's and provided researchers with colliding e^+e^- beams in the range of energies $1.5 \text{ GeV}/c^2$ to $3.0 \text{ GeV}/c^2$. Many important discoveries were made in that energy range including discovery of the τ lepton, the discovery of charmed quarks, and many other measurements. Machines of higher energy were soon planned in the anticipation of yet further discoveries. The CESR e^+e^- storage ring was constructed at Cornell University with an energy range of 4-7 GeV/c^2 at the same time that the b quark with a mass of $5 \text{ GeV}/c^2$ was discovered at Fermilab². This provided a unique setting to explore the upsilon resonances and study the properties of mesons containing the b quark.

A larger e^+e^- ring was installed at SLAC in 1979 which was called PEP. This ring covered the energy range above the upsilon resonances and extended to an energy of $16 \text{ GeV}/c^2$ per beam. The goal of the machine was to search for the expected companion of the bottom quark, the top quark. Alas, the top quark was not to be found in this energy range. The storage ring did provide, however, an abundant supply of hadronic events containing b and c quarks, $\tau\bar{\tau}$ lepton events, and $\mu^+\mu^-$ events all of which provided much information with regard to the known elementary particles. Experiments have yielded lifetime values for the τ lepton, the b and c quarks, the charge asymmetry due to the Z^0 boson interfering with the photon and other important experimental results.

§2.2 QED Reactions

The physics of e^+e^- collisions is deeply rooted in the acceptance of the theory of quantum electrodynamics or QED. QED has proven to provide an accurate

description of physics processes involving the interaction of charged particles. It is the deviation of the behavior of some particles from pure QED interactions which determines the new physics found in e^+e^- machines. For this reason I would like to begin by discussing briefly some of the simple QED reactions. This leads naturally into the discussion of the production of $\tau^+\tau^-$ pairs in e^+e^- collisions.

The reaction $e^+e^- \rightarrow e^+e^-$ is the first reaction which comes to mind. This reaction, which is dominated by the diagrams shown in Fig. 1, has a large cross section in the forward direction due to the second diagram shown. This makes it a convenient source of high energy electrons for calibration and provides an accurate determination of the luminosity. However, the two graphs shown in Fig. 1 a) are not the entire story. There are large radiative contributions and virtual contributions to the cross section which need to be dealt with if the process is to serve as a measure of the luminosity. These corrections have been calculated (see Reference 9) and incorporated into a Monte Carlo event generator¹⁰ which allows one to calculate acceptances.

The result of selecting these events is shown in Fig. 2. In this figure the differential distribution in $\cos\theta$ of the positively charged electron is plotted after the data have been selected by the DELCO apparatus. The efficiency for the selection criteria was $(18.1 \pm 0.4)\%$ for a generated cross section of 0.451 nb . One can see the forward peaking of the differential cross section. Also visible are the acceptance limits of the apparatus at $\cos\theta \approx 0.6$. The use of the cross section in the backward hemisphere is due to the influence of the first annihilation diagram shown in Fig. 1. The Monte Carlo prediction of this process, after detector simulation, (although with lower statistics) is plotted over the data points. Another process which can be calculated by using QED is the reaction $e^+e^- \rightarrow \mu^+\mu^-$. This process is also useful in calibrating the detector and also provides a cross section for the luminosity measurement. The differential cross section is given by the formula:

$$\frac{d\sigma_{\mu^+\mu^-}}{d(\cos\theta)} = \frac{\alpha^2}{3s} \beta_\mu (1 + \cos^2\theta) [1 + \delta_{rad}(\cos\theta) + \delta_{weak}(\cos\theta)]$$

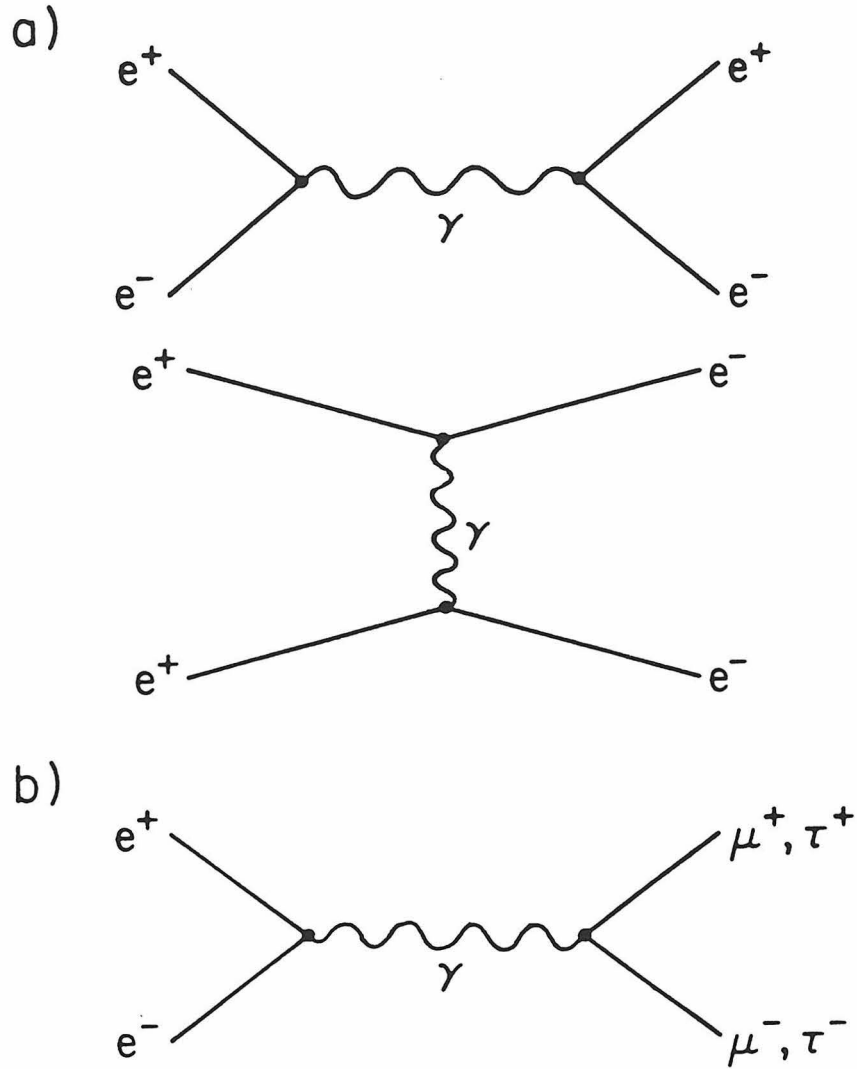


Figure 1. The QED graphs for reactions which lead to a final state that contain a pair of leptons. The first two contribute to Bhabha scattering. This process can proceed through both an exchange diagram and an annihilation diagram as is shown in a). The annihilation channel is the only channel available to produce a pair of leptons other than electrons as is shown in b).

where $\delta_{rad}(\cos \theta)$ is the contribution from radiative corrections and $\delta_{weak}(\cos \theta)$ is the correction due to the interference of the weak neutral current (Z_0) with the electromagnetic current (γ). The weak correction contributes a term which is linear in $\cos \theta$; *i.e.*, there is a term proportional to $\cos \theta$ in the differential cross section. This fact gives rise to an asymmetry in the angular distribution of the μ^+ (or μ^-). The cross section thus becomes larger in the backward hemisphere. In Fig. 3 the differential distribution in $\cos \theta$ of the positive muon is shown. The result of a fit of the form $A(1 + \alpha \cos \theta + \cos^2 \theta)$ is drawn on top of it and the charge asymmetry is clearly evident. The fit yielded a value of g_A^2 of (0.25 ± 0.18) which is consistent with the theoretical expectations.

The next topic is the production of $\tau^+\tau^-$ pairs. This process is almost the same as $\mu^+\mu^-$ production. The only difference is in the mass of the final state lepton. Thus the production cross section:

$$\frac{d\sigma_{\tau^+\tau^-}}{d(\cos \theta)} = \frac{\alpha}{3s} \beta_\tau (1 + \cos^2 \theta) (1 + \delta_{rad} + \delta_{weak})$$

has the same form as that for $\mu^+\mu^-$. One of the differences in the two processes is that the τ has a very short decay path compared with the muon. Instead of observing the final state lepton, as in the case of the muon, only the decay products of the τ are observed. This has the consequence that the polarizations of the τ^+ and τ^- play a role in the observed decay product distributions. The effect is seen in correlations in the momentum and angular distributions between the τ^+ decay products and the τ^- decay products. Therefore, it is necessary to use the differential cross section for $\tau^+\tau^-$ which includes the polarization of the τ leptons. The effect is not large and amounts to corrections of the order of 2.5% for efficiencies. This depends upon the details of the selection criteria, of course. The full differential cross section is given in Appendix A along with the various differential decay rates for polarized τ decay. This cross section, when multiplied by the normal radiative corrections, yields a close approximation to the true radiatively corrected cross section.

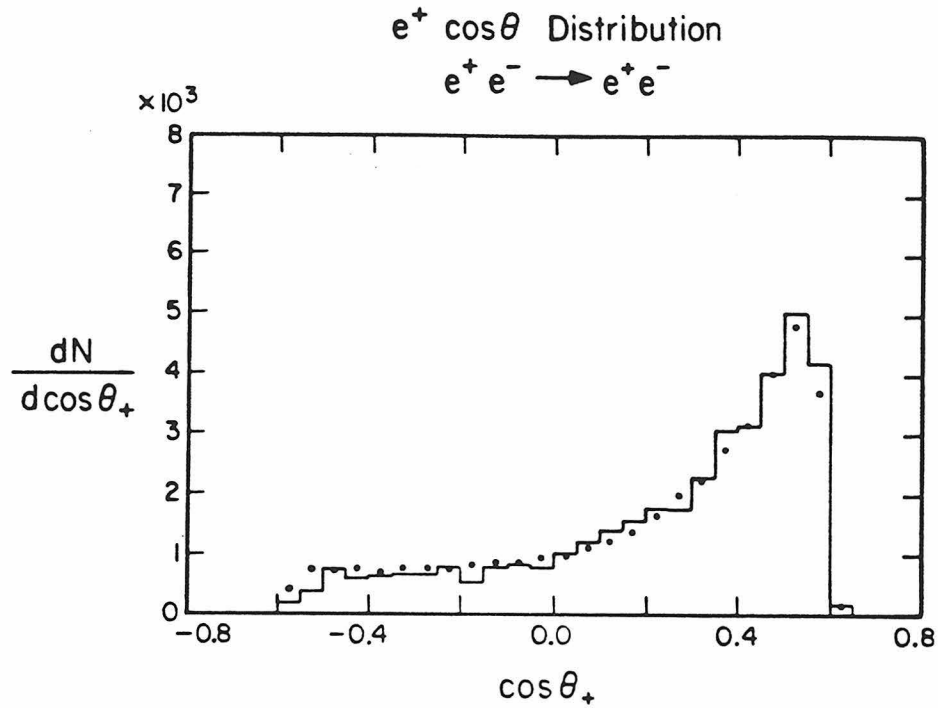


Figure 2. The observed differential distribution for Bhabha scattering events in DELCO. The events were selected by demanding two tracks in the event with shower counter responses consistent with $14.5 \text{ GeV}/c^2$ electrons. One can clearly see the forward peaking of the cross section. The Monte Carlo simulation of the process in the apparatus is shown by the solid line.

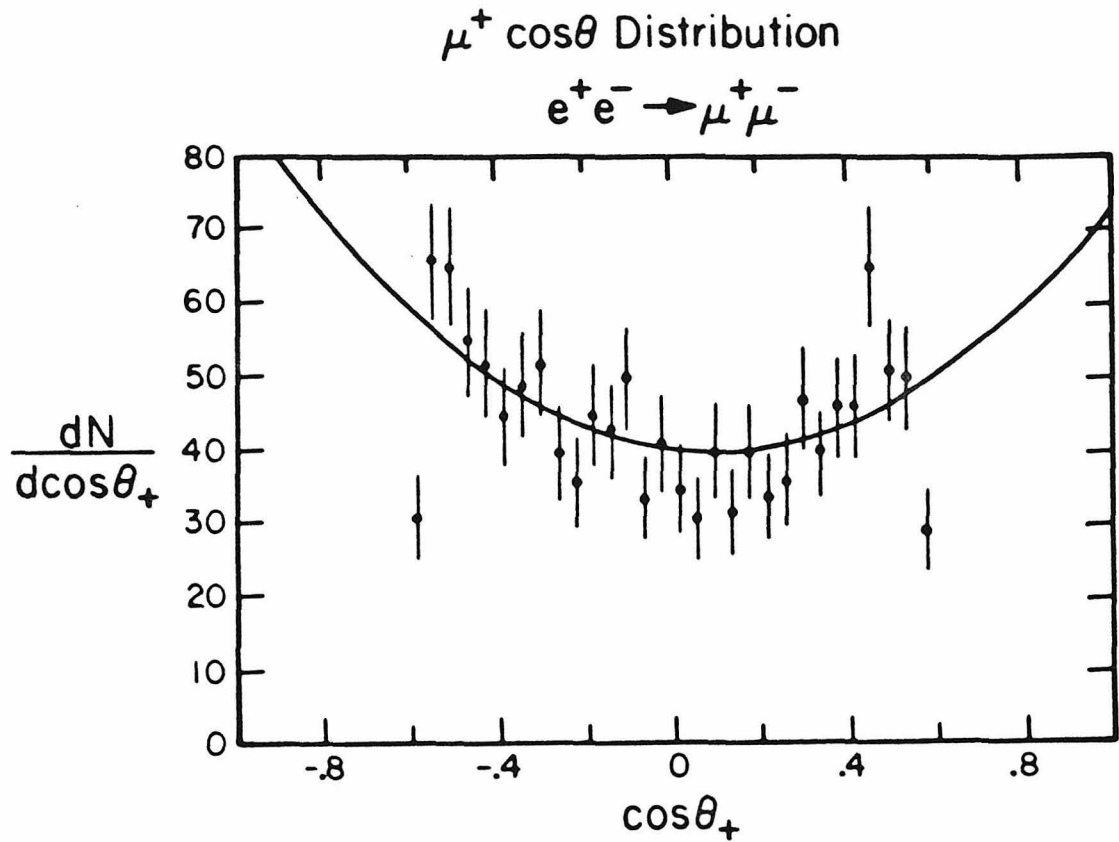


Figure 3. The observed differential distribution for $e^+e^- \rightarrow \mu^+\mu^-$ events in DELCO. The events were selected by demanding two tracks in the event with shower counter responses consistent with minimum ionizing particles. The acolinearity of the two tracks was required to be less than 100 mrad. The fit to polynomial form $A(1 + \cos^2\theta + \alpha\cos\theta)$ in the region $|\cos\theta| < 0.5$ is shown drawn over the data.

The decay rate of a polarized τ lepton has been calculated for a variety of decays (see Ref. 6). The results are presented in Appendix A. The τ particles are produced with nearly the beam energy, which at PEP is $14.5 \text{ GeV}/c^2$ per beam. This implies that the τ 's, with a mass of $1.784 \pm 4 \text{ GeV}/c^2$, have a Lorentz γ_τ of nearly 8.2 and consequently the average opening angle for decay products is $\langle \theta \rangle \sim \frac{1}{\gamma_\tau} = 123 \text{ mrad}$. Thus the decay products typically follow the direction of the parent τ closely. This fact is very useful in distinguishing τ events from other types of processes. It also aids in separating τ events from Bhabha and $\mu^+\mu^-$ events which are very highly anti-colinear (back to back) since radiative corrections only contribute an r.m.s. smearing of 10 mrad to the acolinearity of the two scattered leptons.

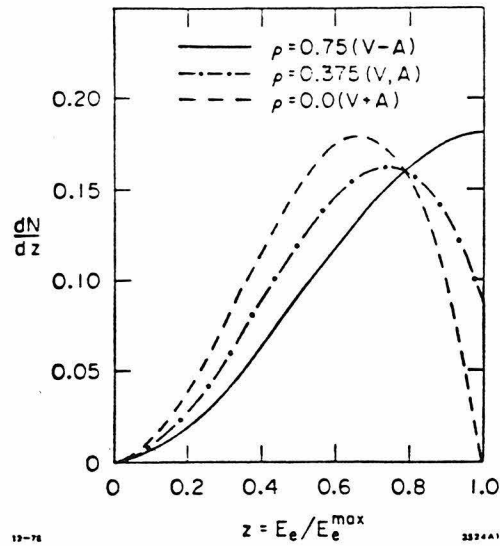
§2.3 Decays of the τ Lepton

In general, there are two types of decays of the τ lepton, leptonic and semi-leptonic. The leptonic decay modes are $\tau \rightarrow e\bar{\nu}_e\nu_\tau$ and $\tau \rightarrow \mu\bar{\nu}_\mu\nu_\tau$. These decays are identical to the well-known decay $\mu \rightarrow e\bar{\nu}_e\nu_\mu$ which, in the context of weak interaction theory, is well understood and provides a good deal of the known information on weak interactions. The $\tau \rightarrow e\bar{\nu}_e\nu_\tau$ is perhaps the best studied decay mode. The information gained by studying its properties has verified many aspects of τ decays. The chiral structure of the decay was determined to be V-A by studying the momentum spectrum of the electron in the decay $\tau^\pm \rightarrow e^\pm\bar{\nu}_e\nu_\tau$. For V-A structure one expects the standard Michel¹¹ spectrum (with $\rho=.75$) shown in Figure 4 a). The DELCO experiment at SPEAR, which took data at several

beam energies, observed an electron momentum distribution which when fitted to the Michel parameter preferred V-A structure. In the same experiment the shape of the threshold for the cross section of $e^+e^- \rightarrow \tau^+\tau^-$ was studied yielding a determination of the spin and mass to be $\frac{1}{2}$ and $1748 \pm 4 \text{ MeV}/c^2$, respectively. These data are shown in Figure 5. The $\tau^\pm \rightarrow \mu^\pm \bar{\nu}_\mu \nu_\tau$ decay mode is similar to the $\tau^\pm \rightarrow e^\pm \bar{\nu}_e \nu_\tau$ decay mode. The branching ratios are predicted to be nearly equal, with the $\tau^\pm \rightarrow \mu^\pm \bar{\nu}_\mu \nu_\tau$ branching ratio being less by a factor of 0.974 due to differences in the available phase space in the two decays. The measured values for the branching ratios are shown in Table 1. The measured values are consistent with equality although the measurements are only accurate at the 5-10% level. This leaves significant room for additional interactions that the τ might have.

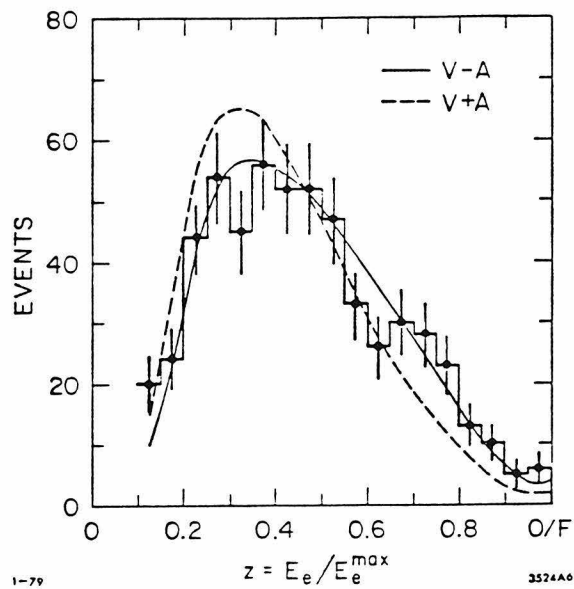
The semileptonic decays are less understood but in many cases can be calculated with a few theoretical assumptions. The simplest decays involve the lowest mass pseudoscalar particles, the π and K . The decays $\tau^\pm \rightarrow \pi^\pm \nu_\tau$ and $\tau^\pm \rightarrow K^\pm \nu_\tau$ are related to the $\pi \rightarrow e\nu(\mu\nu)$ and $K \rightarrow e\nu(\mu\nu)$, respectively. These decays will be discussed later on in the thesis. They are two body decays and hence the momentum distribution in the lab frame is relatively flat. Figure 6a) shows the prediction for the momentum distribution of the charged kaon in the decay $\tau^\pm \rightarrow K^\pm \nu_\tau$ and other decays. In this thesis a measurement of the branching ratio for the decay $\tau^\pm \rightarrow K^\pm \nu_\tau$ is made.

In the context of SU(3) symmetry the τ lepton couples to the hadronic current through pseudoscalar, vector, and axial vector states. These states are listed along with their quantum numbers in Tsai¹². The first notable states after the pseudoscalar lowest lying states are the vector states, the $\rho(770)$ and the $K^*(890)$ which are Cabibbo favored and Cabibbo suppressed respectively. The $\rho(770)$ branching ratio has been measured⁸ as shown in Table 1. This channel, $\tau^\pm \rightarrow \pi^\pm \pi^0 \nu_\tau$, is expected to be dominated by the $\rho(770)$ channel. In fact, the expected decay rate can be related to the I=1 (isospin) component of the reaction



13-78

3524A1



1-79

3524A6

Figure 4. The expected shape of the momentum distribution for electrons in τ decay in the rest frame of the τ . The data shown in the second graph, as measured by the DELCO experiment at SPEAR, are a superposition of several beam energies. These data were fitted to the Michel spectrum with the Michel parameter, ρ , as a free parameter in the fit. The result favors $\rho = .75$, a V-A leptonic current structure.

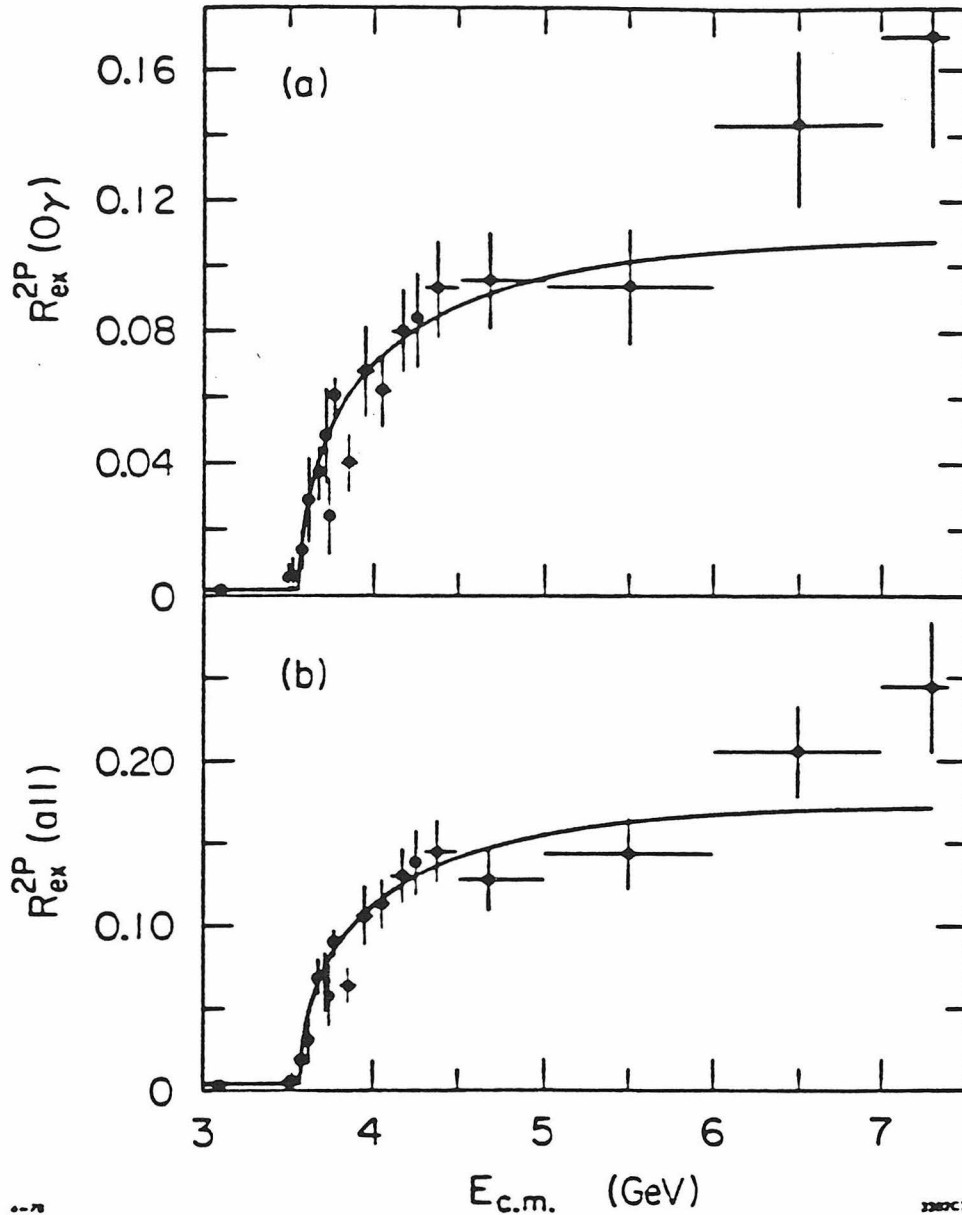


Figure 5. The measurement of the threshold behavior of the $e^+e^- \rightarrow \tau^+\tau^-$ production cross section allowed the determination of both the mass and the spin of the τ lepton. The data shown here, recorded by the DELCO at SPEAR group, show the measured rate of events containing two tracks, one of which is an electron, divided by the point cross section, $\sigma_{\mu\mu}$. For a spin $\frac{1}{2}$ lepton this rate is proportional to the β of the produced lepton, as shown by the curve drawn over the data points.

Table 1. Decays of the τ lepton (see the text for references).

τ Branching Ratios		
Decay Mode	Measured	Predicted
$\tau^\pm \rightarrow e^\pm \bar{\nu}_e \nu_\tau$	$(16.5 \pm 0.9)\%$	-----
$\tau^\pm \rightarrow \mu^\pm \bar{\nu}_\mu \nu_\tau$	$(18.5 \pm 1.1)\%$	$(16.1 \pm 0.9)\%$
$\tau^\pm \rightarrow \rho^\pm \nu_\tau$	$(22.1 \pm 2.4)\%$	$(20.1 \pm 1.1)\%$
$\tau^\pm \rightarrow A_1^\pm \nu_\tau$	$(10.8 \pm 3.4)\%$	$(18.2 \pm 0.5)\%$
$\tau^\pm \rightarrow \pi^\pm \nu_\tau$	$(10.3 \pm 1.2)\%$	$(9.91 \pm 0.5)\%$
$\tau^\pm \rightarrow K^{*\pm}(890) \nu_\tau$	$(1.7 \pm 0.7)\%$	$(1.4 \pm 0.1)\%$
$\tau^\pm \rightarrow K^\pm \nu_\tau$	$(1.3 \pm 0.5)\%$	$(0.71 \pm 0.1)\%$

$e^+e^- \rightarrow 2\pi$ by making the assumption of CVC. This relation is given by:

$$\Gamma_{\tau^\pm \rightarrow \pi^\pm \pi^0 \nu_\tau} = \frac{G^2 \cos^2 \theta_c}{96\pi^3 m_\tau^3} \int_0^{m_\tau^2} dq^2 (m_\tau^2 - q^2)^2 (m_\tau^2 + 2q^2) \times \frac{\sigma_{e^+e^- \rightarrow \pi\pi}^{I=1}(q^2)}{\sigma_{\mu^+\mu^-}(q^2)} \quad (1)$$

where $\sigma_{\mu^+\mu^-}(q^2)$ is the point cross section for muons, G is the Fermi coupling, θ_c is the Cabibbo angle, q is the invariant mass of the $\pi\pi$ system, and $\sigma_{e^+e^-}(q^2)$ is the cross section for the reaction $e^+e^- \rightarrow \pi^+\pi^-$ in the $I=1$ channel. The predicted branching ratio value of 23.5% agrees well with the measured value. This provides strong evidence for the validity of CVC in τ decays.

The decay $\tau^\pm \rightarrow K^{*\pm}(890) \nu_\tau$ is related to the $\tau^\pm \rightarrow \rho^\pm \nu_\tau$ decay via SU(3) sum rule predictions¹². Apart from phase space differences the couplings are related

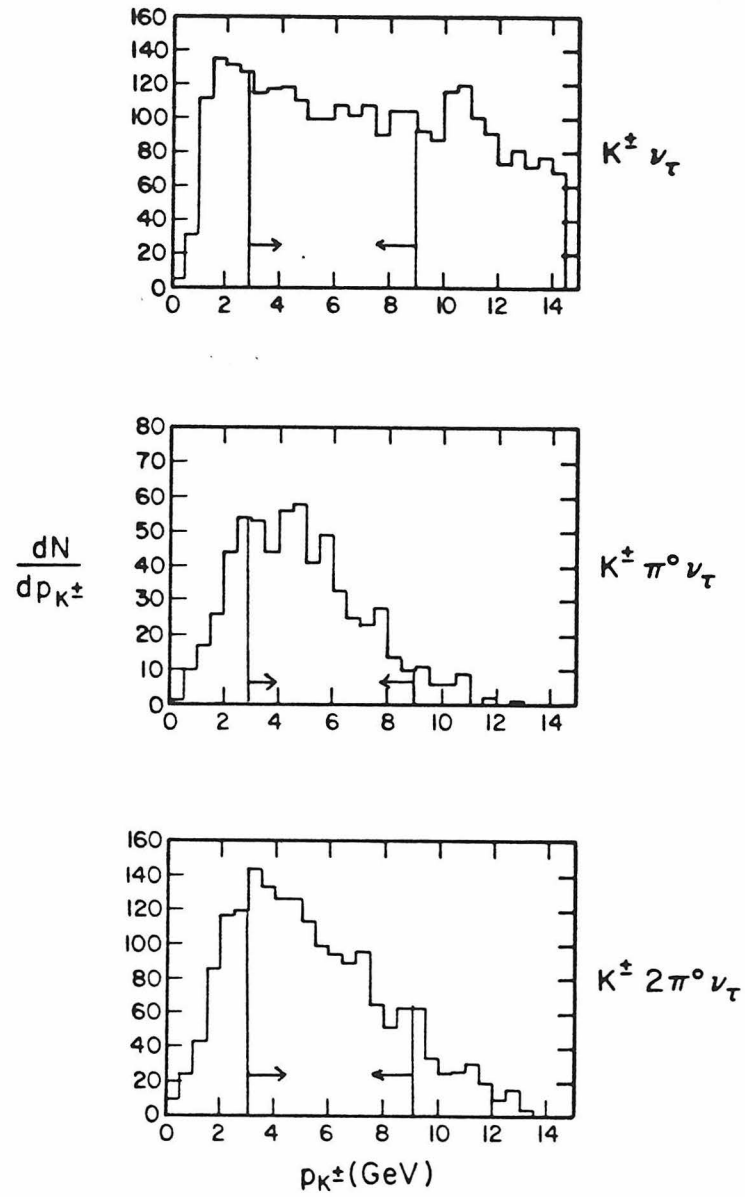


Figure 6. These figures demonstrate the kaon momentum range over which the DELCO Cherenkov counter is able to separate pions from kaons. The acceptance for several of the decay modes containing charged kaons is shown.

as the ratio of the masses¹²:

$$\frac{f_\rho^2}{m_\rho^2} = \frac{f_{K^*}^2}{m_{K^*}^2} \quad (2)$$

and also the Cabibbo suppression, $\tan^2\theta_c$. This decay has been observed¹³, albeit with low statistics, and the measured branching ratio agrees with the predicted value, hence lending some support to the SU(3) sum rule predictions.

The axial vector resonances should also couple to the τ due to the V-A structure of the interaction. The lowest lying axial vector state is the $A_1(1100)$ which decays into three pions. This mode has indeed been observed and more recently there have been attempts to analyze its spin and parity¹⁴. These results are consistent with predicted values. Again, SU(3) sum rules predict the relation $f_{A_1}^2 = f_\rho^2$ between decay rates of the A_1 and ρ .

The Cabibbo-suppressed counterpart to the A_1 channel is the Q(1300) which decays into $K\pi\pi$ dominantly. There have been no measurements available on this decay mode prior to this thesis. The branching ratio can be predicted by SU(3) sum rules. Observation of this decay would provide strong support for SU(3) symmetry in τ decays.

The final decay channel which has been observed is the $\tau^\pm \rightarrow \rho^\pm(1580)\nu_\tau$. This decay rate can be related as in the case of the $\rho(770)$, to the cross section for the reaction $e^+e^- \rightarrow \rho^\pm(1580)$ in the I=1 channel as in equation 1. The dominant decay of the ρ' is into four pions; however, the $\rho' \rightarrow K^*\bar{K}$ channel also has a respectable branching ratio of $(9 \pm 2)\%$. The four pion channel has been studied in the channel $\tau \rightarrow 3\pi^\pm\pi^0\nu_\tau$ and the branching ratio is in agreement¹⁴ with theoretical predictions¹⁵. These predictions have been made possible by the recent measurements of the cross section $e^+e^- \rightarrow 4\pi^\pm$ at ORSAY¹⁶. The $K^*\bar{K}$ channel has not yet been observed in τ decays but the branching ratio is expected to be very small due to phase space suppression of the decay rate. The phase space in this decay is available only near the endpoint of the $K^*\bar{K}$ invariant mass distribution just below the mass of the τ , $1.784 \pm 4 \text{ GeV}/c^2$. This feature will be discussed later

in the context of the τ neutrino mass.

A discussion of τ decays would not be complete without a mention of the sister particle the τ neutrino. This particle has never been directly observed; only its absence has been observed. However, it seems to couple with the standard V-A structure⁷. The remaining parameter of interest is the mass of the neutrino. There is very little experimental evidence for massive neutrinos, with the exception of a highly controversial electron neutrino mass measurement by Lubimov et al.⁶. If Lubimov's result is taken to be correct, there might well be implications regarding the masses of other neutrinos. Several models¹⁷ involving the gauge group $U(1) \times SU_L(2) \times SU_R(2)$ predict neutrino masses which are roughly proportional to the mass of their associated lepton. This type of model would then, by using Lubimov's result of an electron neutrino mass on the order of a few electron volts, predict a τ neutrino mass in the range of $100 \text{ MeV}/c^2$. However there is no evidence one way or the other regarding the τ neutrino mass. Current published experimental limits range from $250 \text{ MeV}/c^2$ as measured in the $\tau^\pm \rightarrow e^\pm \bar{\nu}_e \nu_\tau$ channel to $164 \text{ MeV}/c^2$ in the $\tau^\pm \rightarrow 3\pi^\pm \pi^0 \nu_\tau$ channel. In this thesis a new limit was placed by using the $\tau^\pm \rightarrow K^+ K^- \pi^\pm \nu_\tau$ channel.

§2.4 Other Processes

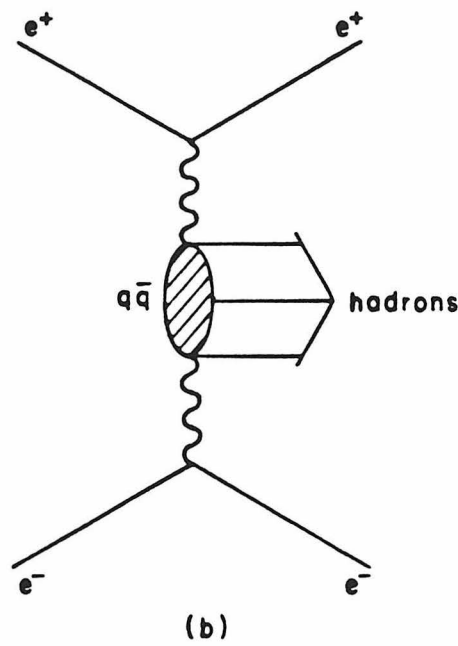
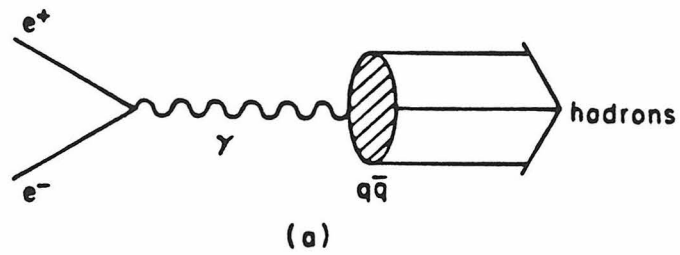
§§2.4.1 Hadron Production

So far the discussion has centered around the production of charged leptons

in e^+e^- annihilation. Another equally important process is the reaction $e^+e^- \rightarrow \text{hadrons}$. This process has been studied extensively in e^+e^- annihilation and has been shown to proceed through the reaction $e^+e^- \rightarrow q\bar{q}$ where q stands for either the u, d, c, s, or b quark as in Figure 7. A model for this process which fits the observed data very well has been developed by the LUND group¹⁸. This model has been reviewed elsewhere. In this analysis it is used to help estimate the backgrounds to the process $e^+e^- \rightarrow \tau^+\tau^-$ decays. These turn out to be small although not completely negligible.

§§2.4.2 Two Photon Processes

The two photon process shown in Fig. 7 is a higher order QED process and therefore suppressed by roughly $\alpha^2 \sim 10^{-4}$ relative to the standard annihilation channel event processes. However, the cross section also is proportional to the inverse of the invariant mass of the hadronic system produced so that at low invariant mass large cross sections can be observed. The process can be modeled, as in the case of the $e^+e^- \rightarrow q\bar{q}$ channel¹⁸, by the LUND mechanism, at large q^2 . This process potentially could be a background to $e^+e^- \rightarrow \tau^+\tau^-$; however, it turns out to be straightforward to eliminate these events from $\tau^+\tau^-$ data samples because of their low energy and their distinct kinematical features.



5 - 84

4769A4

Figure 7. The lowest order Feynman diagrams for production of hadronic events in the annihilation channel and in the two-photon channel. These events serve as possible backgrounds to charged kaons from τ decays.

Chapter 3. Apparatus

This experiment was performed using the DELCO apparatus which is located on the PEP e^+e^- storage located at the Stanford Linear Accelerator Center. In this chapter the DELCO apparatus and its setting on the storage ring will be described. In addition there is a vast amount of software analysis code which deserves some attention and will be described along with the apparatus. Finally, an important part of the analysis is the simulation of the data via Monte Carlo techniques, so a section of the chapter will be devoted toward describing it.

It does not seem appropriate in this thesis to give a detailed description of the operation of the PEP e^+e^- storage ring itself; the theory and principles of operation may be found elsewhere¹⁹. The discussion will concentrate on the aspects of the storage ring which were important to or had an effect on the experiment.

The detector apparatus was constructed through the effort of several groups of people both at Stanford and at Caltech. I will try to do justice to the various components of the detector although I did not have direct responsibility for the construction of equipment which was built at SLAC.

§3.1 Environment

The DELCO experiment was performed at the PEP e^+e^- colliding beam storage ring. The PEP ring was capable of storing counter-rotating beams of positrons and electrons of equal energy in an energy range from 5 GeV/c² to 17 GeV/c² per particle per beam. The beams were brought into collision via strong focusing quadrupole magnets in six buildings, called interaction regions, around the ring as shown in Figure 8. Since the ring has a radius of roughly 350 meters there is ample room to construct experimental equipment around these collision points or interaction points (IP's), as they are called. The effective luminosity at each of the IP's is roughly $1 - 2 \times 10^{31} \text{ cm}^{-2}\text{s}^{-1}$ and allowed a collection of 220 pb⁻¹ of integrated luminosity of over a period of three years of experimental running.

The beams themselves have a very small angular divergence and cross-sectional size at the IP and in addition have small energy spread. Table 2 shows several of the parameters describing the beam²⁰. The absolute calibration of the beam energy is taken from a measurement of the magnetic field of the ring and the known radius of curvature. The position of the beam centroid is monitored on an event-to-event basis by beam position monitors (BPM's) which are located 270 cm on either side of the IP. These monitors are described later on in this chapter. At the IP the beams have cross-sectional dimensions of 50 microns vertically (y) and 400 microns horizontally (x) while along the beam direction (z) the beam is approximately 2.5 cm long. In the transverse dimensions (x & y) the beam is found to be nearly Gaussian and in the longitudinal dimension (z) it is nearly triangular.

An enormous effort had to be made in order to shield the detectors from background radiation induced by the beams. The end result of this effort was a relatively quiet environment for data taking.

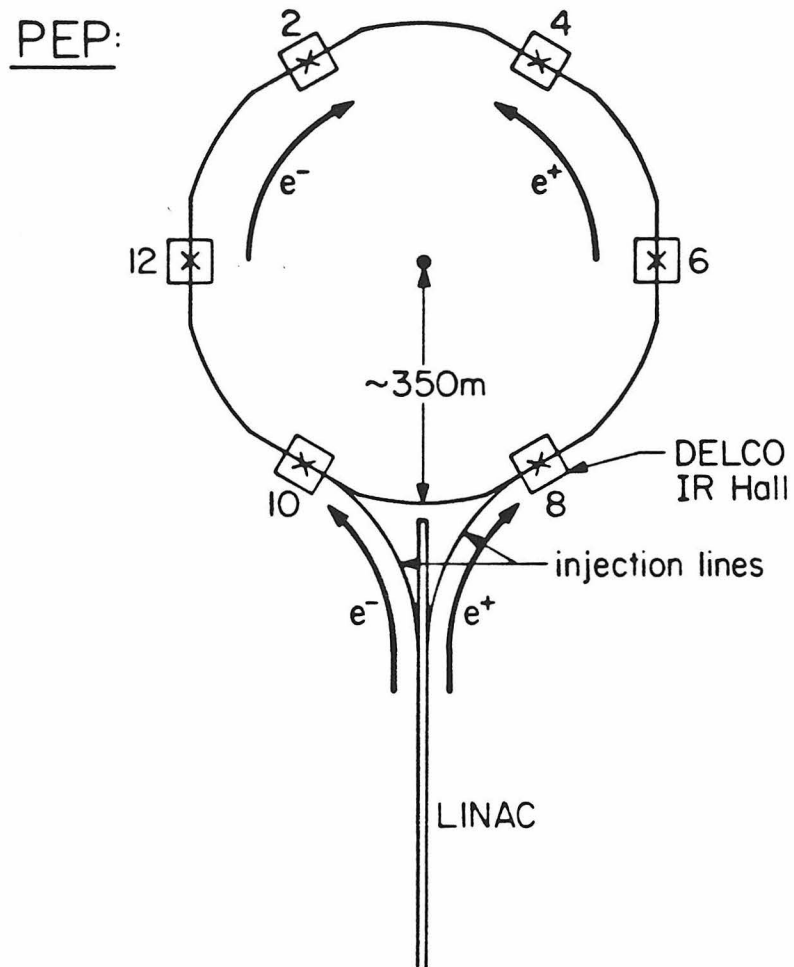


Figure 8. The PEP ring provided six interaction regions for experimental purposes. It used the SLAC LINAC as a source of positrons and electrons.

Table 2. Typical PEP machine parameters for 1983 and 1984 running years.

PEP Machine Parameters	
Beam Energy	14.5 GeV/c ²
Radius	~ 350 m
β_y^*	11 cm
β_x^*	3.0 m
ν_x	21.15
ν_y	18.19
η_x^*	0.0
I_{max}	24.8 ma/beam
L_{max}	$32.0 \times 10^{30} cm^{-2} s^{-1}$

§3.2 The DELCO Detector

The DELCO apparatus was designed to identify particles, primarily electrons and kaons by using a gas Cherenkov counter. It is a magnetic spectrometer, capable of measuring charged particle momenta, and is augmented by gas threshold Cherenkov counters, E&M shower counter and a time of flight scintillator counter system which provides particle identification over various momentum ranges. The detector is shown in Fig. 9. The main components of the detector are: a magnetic spectrometer which uses drift chambers to track charged particles and which covers 90% of 4π , a system of lead-scintillator sandwich shower counters which cover nearly 90% of 4π , and a large solid angle coverage Cherenkov counter which covers 70%

of 4π , as shown in Fig. 9.

The detector ran synchronously with the beam collisions. After a beam collision, which occurs at a frequency of 480 kHz, a fast electronic trigger system determines whether or not an e^+e^- collision has happened and, if so, all of the drift chamber and counter information is read out onto magnetic disk drives and finally onto magnetic tape. These tapes are then scanned by offline computer algorithms and a first pass tape of important events is written. These first-pass tapes are then further processed until a series of tapes are produced for each specific physics topic, in this case $e^+e^- \rightarrow \tau^+\tau^-$ events.

The calibration of equipment is done by filtering out events useful for a specific calibration task and then using these events to generate a set of calibration parameters for that particular data set. The offline analysis programs read in these calibrations prior to processing each event.

Next a brief discussion of each component of the apparatus will be given.

§§3.2.1 Spectrometer

In describing the detector, it seems that the heart of the apparatus is the magnet and the spectrometer system. The spectrometer is used to define charged particle tracks and measure their momenta. After this, the various counter systems may be used to determine the particle type and other properties.

The magnet itself is a dipole magnet which is constructed to support a Helmholtz coil arrangement. The advantage of such an arrangement is to allow particles to pass through the tracking and counter systems without having to pass

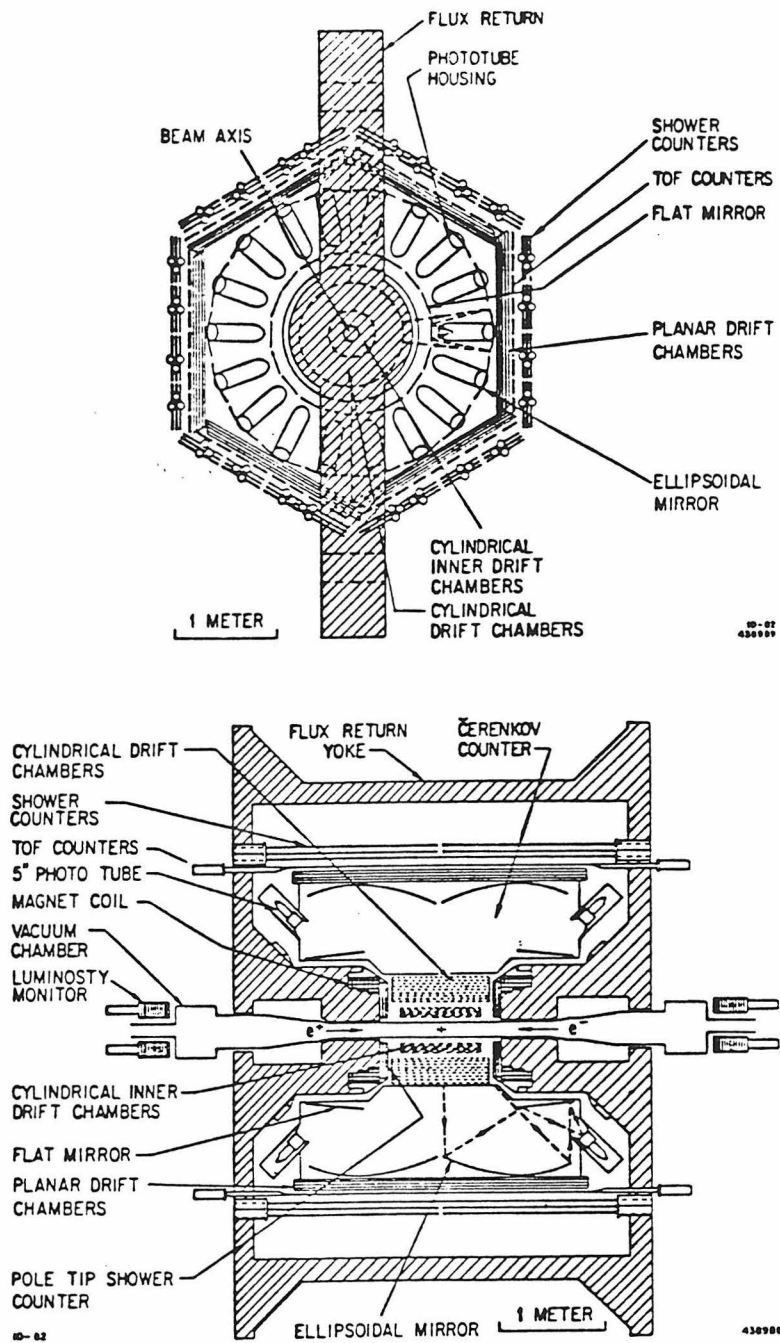


Figure 9. The DELCO apparatus in two views. The first view is the $y - z$ view which shows the segmentation of the apparatus in $\cos\theta$. The second view is in the $x - y$ projection perpendicular to the beam direction. The segmentation of the counter systems in the azimuthal angle ϕ is shown.

through the coil of the magnet as would be necessary in the case of a solenoidal coil. The disadvantages over a solenoidal coil are that the magnetic field is not as high and the field is nonuniform over the tracking volume. The spectrometer is shown in Fig. 9.

The two copper coils mounted on either side have 116 windings, carrying 3000 amperes of current, generate a field of 3.0 k-gauss at the midpoint between the pole-tips. The line integral of the field, $\int \mathbf{B} \cdot d\mathbf{l}$, along a path from the IP through the tracking chambers is roughly 1.5 kg-m. The field was measured by using an NMR probe which had an absolute accuracy of 0.01% . This value agreed with a computer simulated field map²¹ which was fit to the measured field map and is shown in Figure 10. The field map was made by using a HALL probe which rotated around the z axis on an aluminum pipe which ran through the pole-tips of the magnet and yielded a three-dimensional vector grid of field values. This grid was used by the track reconstruction programs to track particles through the apparatus and to determine particle momenta.

§§3.2.2 *Tracking Chambers*

The particle tracking chambers consisted of three separate systems, two cylindrical chambers and one array of planar chambers. The innermost chamber, the IDC, contained 384 sense wires arranged in six cylindrical layers around the beam pipe. The CDC, the second cylindrical chamber, directly followed the IDC and contained 860 sense wires arranged in ten layers around the beam pipe. Finally, positioned outside the Cherenkov counter, is an array of six planar chamber

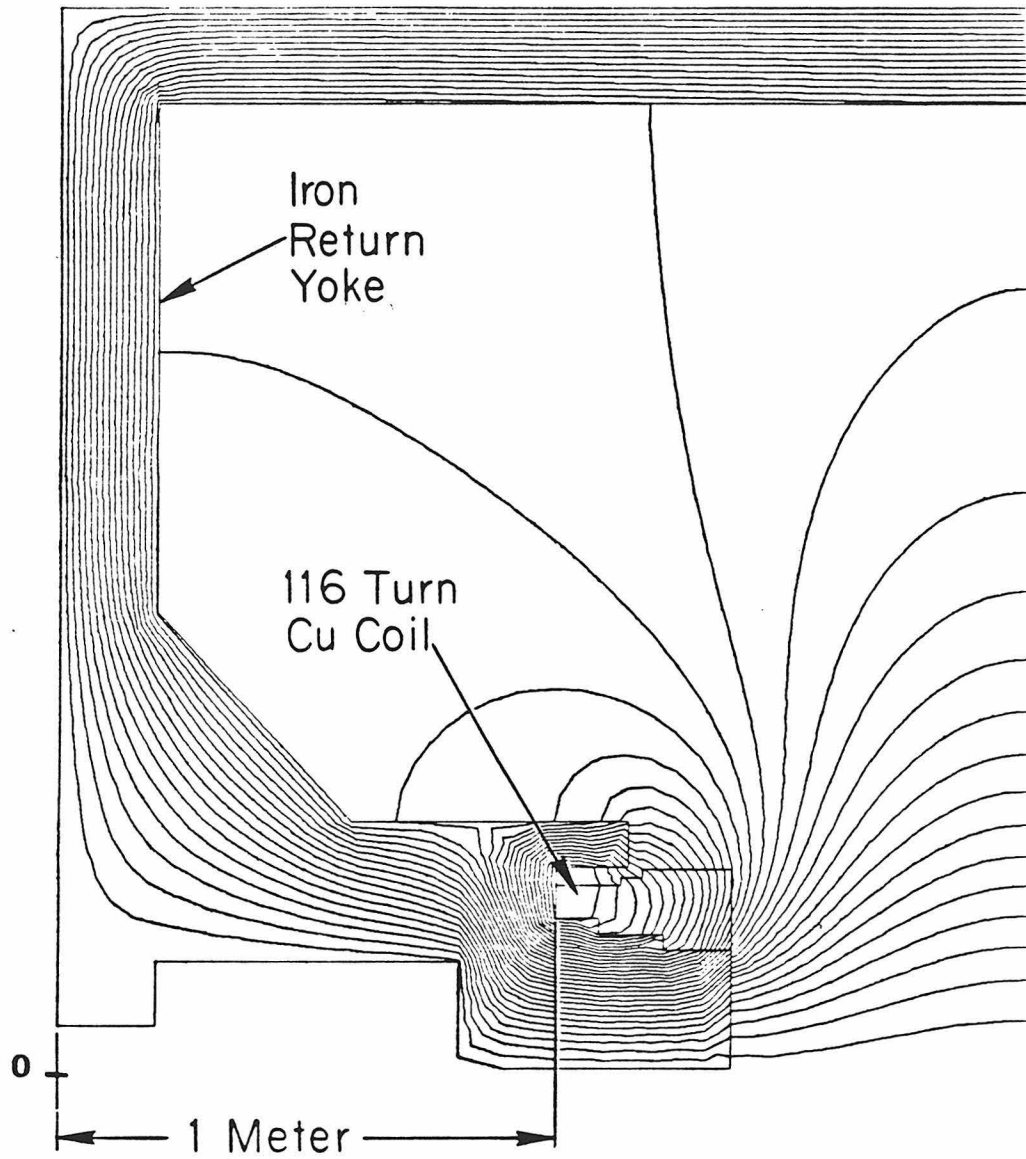


Figure 10. The DELCO magnetic field map.

modules each containing six layers. This system, the PDC system, contains a total of 960 sense wires. Thus a particle passing through the tracking system is measured by a total of 22 drift chamber layers. The sense wires in these layers are arranged so that 12 layers give measurements in the bend plane of the magnet and 10 layers measure the angle of the track with respect to that plane. For particles originating at the interaction vertex there is the additional constraint of the beam position. The performance of the spectrometer is shown by using $e^+e^- \rightarrow e^+e^-$ scattering events. The electrons which are scattered into the detector are, ignoring radiative corrections, relatively monochromatic with an energy of $14.5 \text{ GeV}/c^2$. The spectrometer is expected to have roughly Gaussian response in the variable $\frac{1}{p}$. In Figure 11 the distribution in $\frac{1}{p}$ is shown.

§§3.2.3 Central Chambers

The central chambers are made up of two sections, the IDC and the CDC. The IDC is mounted directly to the beam pipe at a radius of 8 cm. It is constructed in six concentric cylindrical layers of cells and has a total of 384 cells. The first two layers nearest the beam pipe are positioned so that the sense wires in the cell run parallel to the beam direction, *i.e.*, along the z axis. The remaining four are mounted at a 2° stereo angle with respect to the z axis and allow for tracking in three dimensions.

The layout of the cells and sense wires is shown in Figure 12. There are eight cathode field shaping wires per cell which are held at a negative high voltage. The anode wires (sense wire) are held at ground potential. The gas volume is filled with

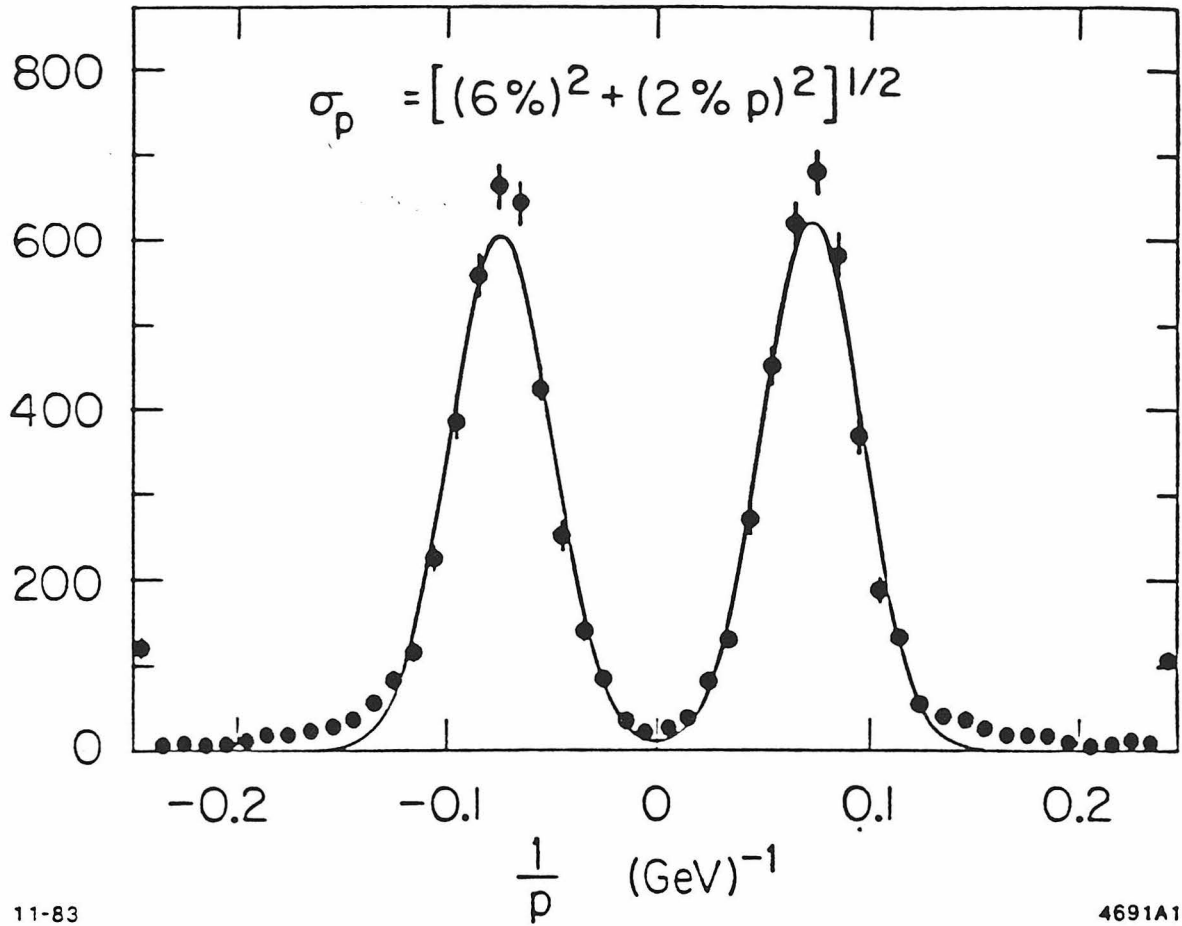


Figure 11. The spectrometer performance for Bhabha electrons. The response is roughly Gaussian in $\frac{1}{p}$.

a mixture of argon and carbon dioxide in the proportion of 89:10:1, (Ar:CO₂:CH₄).

The CDC chamber is constructed in two half-cylinders allowing the removal of the chamber without having to remove the beam pipe. The cell structure, shown in Figure 12, is similar to that of the IDC.

Both the IDC and CDC chambers are filled with the same gas mixture (Argon:CO₂:CH₄, 89:10:1). The electric field inside each drift cell determines the drift characteristics of electrons which come from the ionization of the gas as particles pass through the cell. These electrons drift towards the anode sense wire and, once they are close enough to the wire, generate an electron avalanche thus generating a signal on the wire. An example of the electron drift trajectories is shown in Figure 13. Thus a single electron is multiplied to an avalanche containing 10^7 electrons with a pulse duration of roughly 100 ns. The line impedance is roughly 300, Ω resulting in a signal voltage in the 10 millivolt range. This signal is then amplified and discriminated and sent a TDC timing device. By knowing the velocity of the electrons' drift through the gas mixture, the radial position from the wire of the initial ionization left by the track may be determined. This velocity, as it turns out, is a function of the electric and magnetic field at each point in the cell. In principle this may be calculated and used in calibrating the cell; however, in practice it is simpler to use empirical data and generate a time-to-distance relationship for the cell. These relations were fit to a fifth-order polynomial expansion which was quite adequate in describing the data.

The inner chambers were positioned by mounting surveying tooling balls onto the chambers and adjusting their positions relative to a reference coordinate system relative to the IP. Afterwards, they were adjusted by using tracks from real events to remove any rotations or misalignments introduced in the initial positioning.

The final chamber position resolution obtained varied from layer to layer depending upon the cell size. In the IDC and CDC the resolutions (an example is shown in Figure 14) ranged from 150 μm to 250 μm . Table 3 shows the measured resolutions by layer for the system.

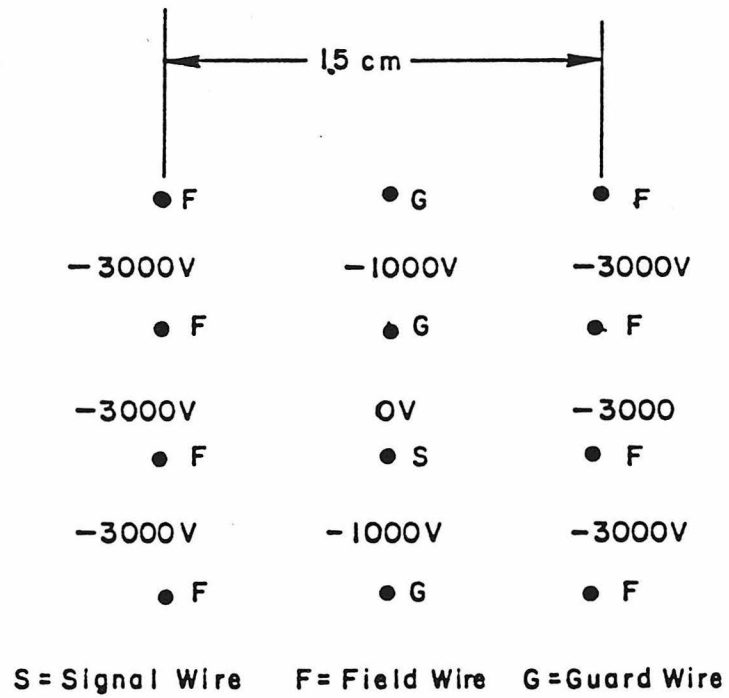


Figure 12. The geometry of the central drift chamber cells used in DELCO. The central chambers used field wires to form the cell electrostatic boundaries.

Central Chamber Electron Drift Trajectories

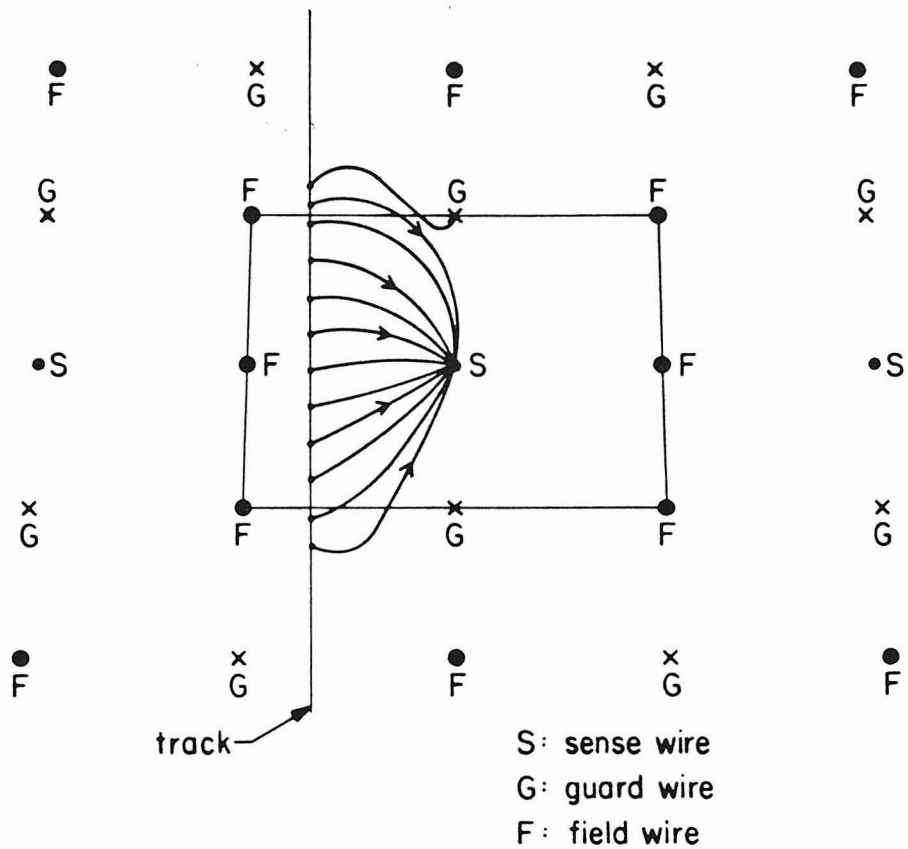


Figure 13. The electron drift trajectories for the central drift chamber cells. The field wires (F) are held at negative high voltage, the guard wires at an intermediate negative high voltage, and the sense wires at ground potential forming the anode of the cell. The ratio of field wire voltage to guard voltage was held at 1.4:1 in this case.

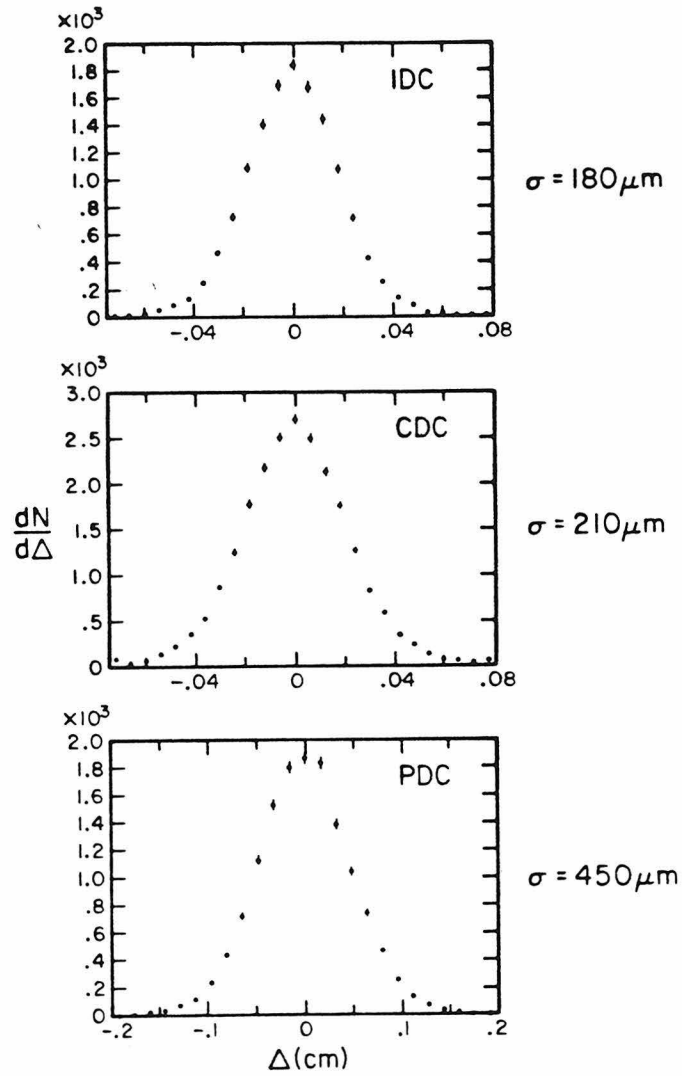


Figure 14. Drift chamber residual distributions for the three drift chamber systems. The average resolution increases with the cell size due to the diffusion of the electrons in the gas as they drift. The residual, Δ , is defined as the drift distance minus the distance of the track to the sense wire.

Table 3. Drift chamber resolutions as measured in $\mu^+\mu^-$ events.

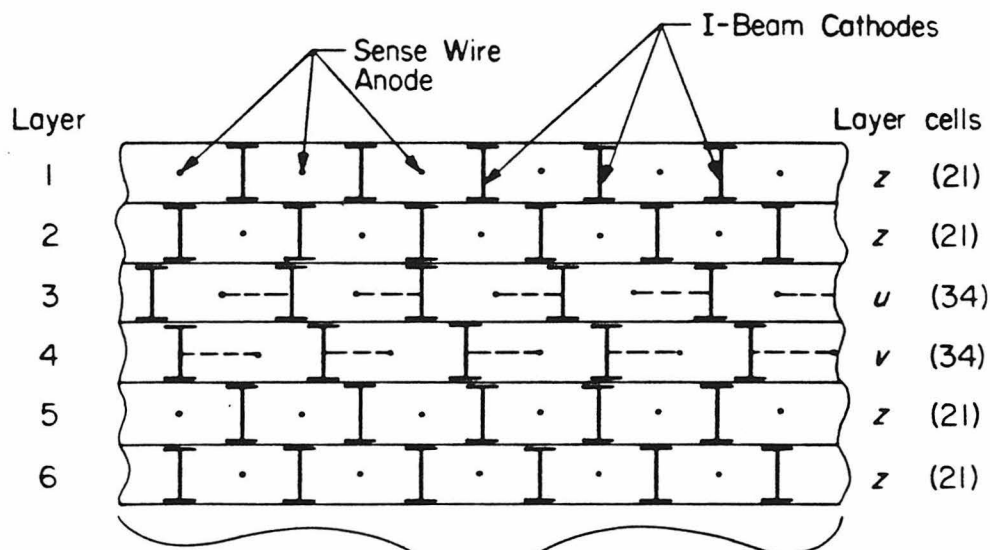
Drift Chamber Resolutions		
Layer	Argon-Ethane	Argon-CO ₂ -Methane
IDC 1(z)	160 μm	212 μm
IDC 2(z)	159 μm	205 μm
IDC 3(u)	188 μm	198 μm
IDC 4(u)	176 μm	211 μm
IDC 5(v)	139 μm	185 μm
IDC 6(v)	143 μm	191 μm
CDC 1(z)	208 μm	269 μm
CDC 2(z)	160 μm	209 μm
CDC 3(u)	174 μm	211 μm
CDC 4(u)	176 μm	229 μm
CDC 5(z)	161 μm	217 μm
CDC 6(z)	167 μm	227 μm
CDC 7(v)	163 μm	227 μm
CDC 8(v)	194 μm	227 μm
CDC 9(z)	173 μm	198 μm
CDC 10(z)	223 μm	251 μm
PDC 1(z)	447 μm	501 μm
PDC 2(z)	477 μm	533 μm
PDC 3(u)	410 μm	428 μm
PDC 4(v)	407 μm	421 μm
PDC 5(z)	458 μm	551 μm
PDC 6(z)	482 μm	566 μm

§§3.2.4 Outer Drift Chambers

The outer chambers were arranged in six planar sextants arranged in a hexagonal cylinder about the beam axis. Each sextant contained six layers of drift cells. The two layers closest to the beam and the two layers farthest from the beam had wires which were parallel to the beam direction (z axis). The two middle layers were set at a 30° stereo angle with respect to the beam axis. This was to allow an accurate measurement of the particle trajectory in z dimension perpendicular to the bend plane of the magnet. The four wires parallel to the z axis helped determine the particle momentum, especially at high momentum where the curvature of the trajectory is very small. At the highest momentum of 14.5 GeV/c the particle deflection is about 2 mm at the PDC chambers position. The layout of the PDC system is shown in Figure 15.

There were two types of planar chambers constructed, axial or z chambers and large stereo angle or u/v chambers. The z chamber design had 21 cells per chamber; the chamber was formed from two sheets of $\frac{1}{16}$ in. AL sheet metal separated by 1 in. AL extrusions having the shape of an I-beam. The long edges of the chambers were 1 in. \times $\frac{1}{2}$ in. AL bars forming the gas seal. The short edges of the chamber were 1 in. by 1 in. AL bars which contained the feedthrough positioning holes for the sense wires. The feedthrough holes were positioned using a drill guide which was made by an interferometric positioning technique with the holes for the wire feedthroughs. An individual cell is shown in Figure 16. The I-beam extrusions were electrically isolated from the $\frac{1}{16}$ AL sheets by 30 mil Mylar insulation. The whole assembly was glued with Versimid glue and the edges of the aluminum sheets fastened with screws to the edge bars. This formed a rigid box-like structure necessary to support the sense wires. The sense wire was made of gold-plated tungsten wire which had a 38 mm diameter. This was glued inside a Delrin feedthrough and held at a tension

a) PDC Layer Arrangement:



b) Sextant Arrangement:

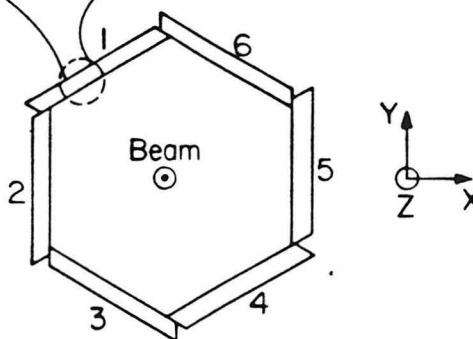


Figure 15. The layout of the PDC chamber system. The chambers were grouped into six sextants each containing six chambers. The sextants were mounted to the Cherenkov counter body. The wire directions inside a sextant were arranged in a $z - z - u - v - z - z$ configuration which gave information on the track position in three dimensions.

of approximately 0.16 N/m .

The cell electrostatics was determined by three voltages: the cathode voltage on the I-beams, the ground voltage of the aluminum sheets, and the anode voltage of the sense wire. The cathode and anode voltages were -3000V and 2025V . This produced the electrostatic potential shown in Figure 17. Electrons, which come from ionization along the particle trajectory, drift toward the sense wire under the influence of the electric field in the cell. The first few electrons to reach the wire start an avalanche which produces the electrical pulse observed on the wire. The arrival time or drift time of the electrons is a function of not only the perpendicular distance of the track (*i.e.*, distance of closest approach or DOCA) from the wire but also upon the incident angle of the track on the cell plane. The measured drift velocity²², along with the electric field versus distance from the sense wire are shown in Figure 18 for the PDC cell structure.

The alignment of the chambers was a major part of the calibration. Each sextant of six chambers was held together by aluminum clamps along the long edge of the chamber. The precise positions of the individual chambers relative to tooling balls mounted on the sextant were measured with optical microscopes. The sextants were then mounted to the Cherenkov counter and installed in the experiment. The sextant tooling balls were then remeasured in the coordinate system of the experiment. The tooling ball positions in both positions yielded the transformation between the coordinate system used to measure the chambers and the experimental coordinate system. This allowed the preliminary positioning of the chambers with an accuracy of 1-2 mm. By using this rough survey as a starting point the exact positions of the chambers were obtained by using tracks from real data and adjusting the relative position of each chamber in the sextant so that the predicted positions matched the measured positions. This yielded a relative position accuracy of 100 μm in the plane of the chamber wires transverse to the wires. Once the chambers in a given sextant were aligned relative to one another the sextant itself was aligned with respect to the central chambers using tracks from real events,

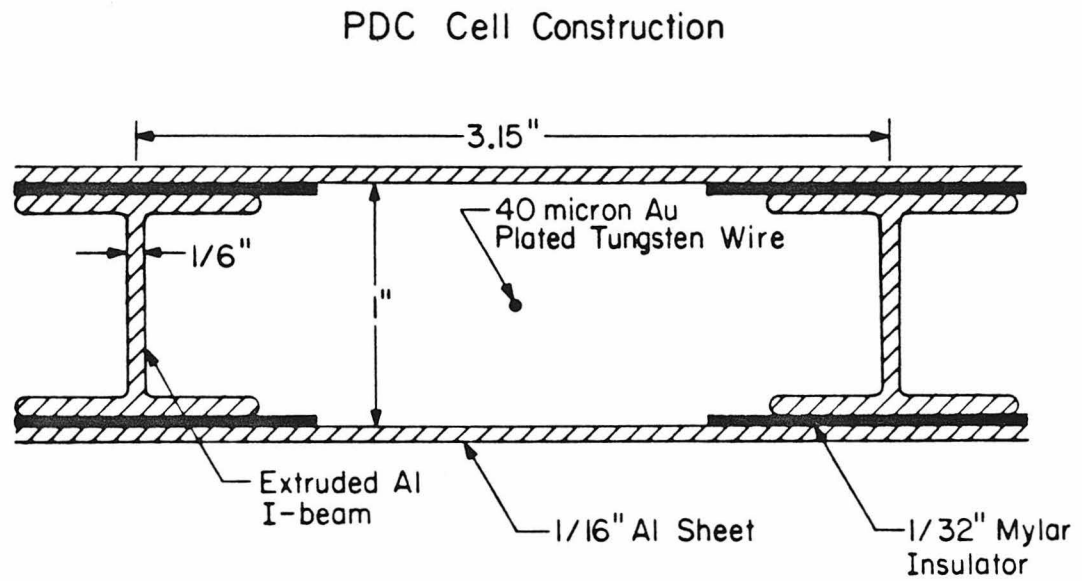


Figure 16. A drawing of a PDC drift chamber cell. The I-beams are electrically isolated from the aluminum ground plane using 30 mil Mylar plastic.

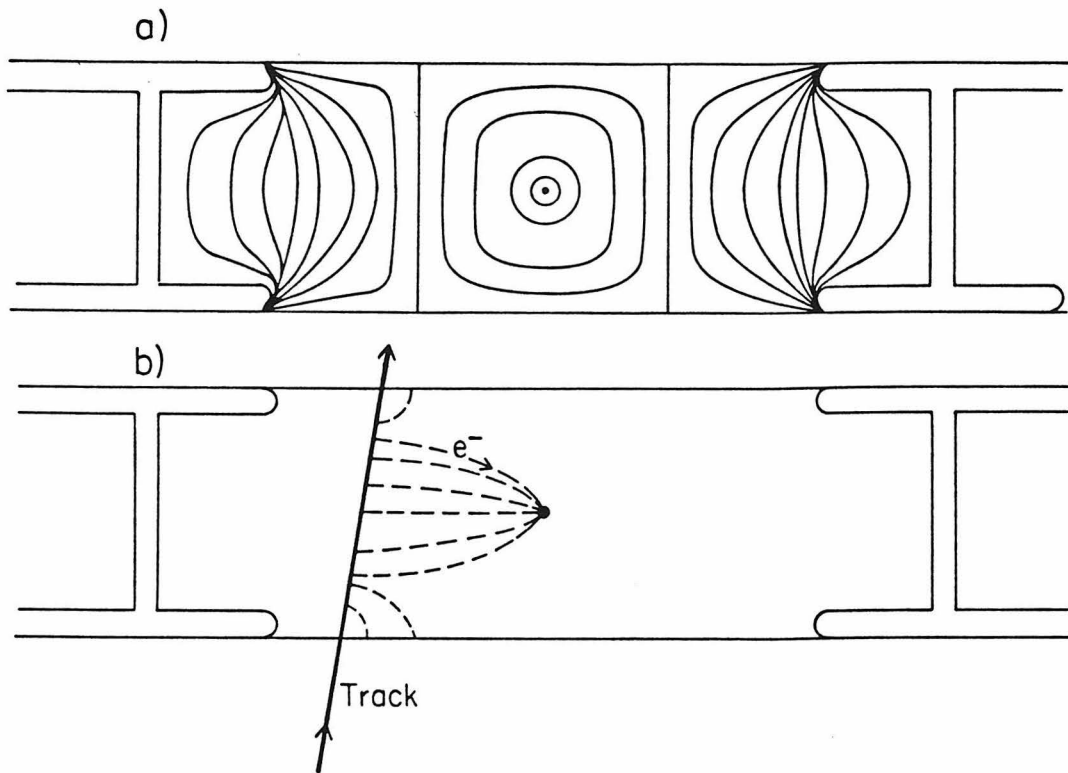


Figure 17. a) The electrostatic potential map for a PDC drift cell. b) The dashed lines show the drift trajectories of electrons traveling toward the sense wire from a track (solid line) which has passed through the cell.

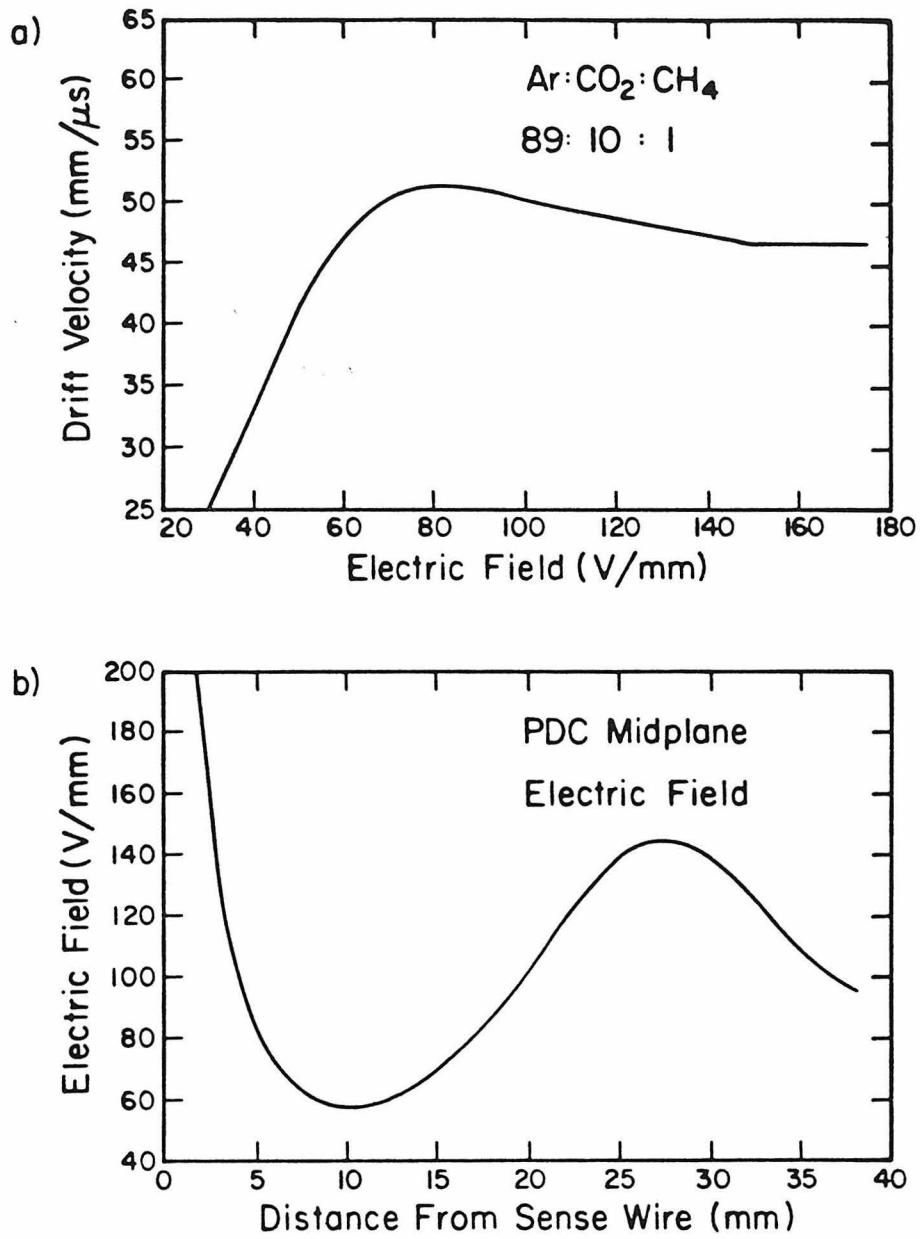


Figure 18. a) The drift velocity versus electric field strength for Ar : CO₂ : CH₄.
b) The PDC cell electric field strength versus distance from the sense wire along the midplane of the cell.

primarily Bhabha scattering events containing two high energy electrons.

§§3.2.5 *Drift Chamber Electronics*

The drift chamber signals were fed into preamplifier/discriminator circuits which were mounted directly on the chamber. The signal preamplifier/discriminator circuit is shown in Figure 19. It consisted of preamplifier transistor pair with a gain of roughly 10. The output of the preamp was fed into a differential line driven with a biased input line. The threshold level of the discriminator was determined by the bias voltage on this input line. The output of this line driven is then fed into another ECL line driver and finally onto long runs of 110Ω twisted pair cables which carried the signal into the experimental counting house. In the counting house the signals latched the pulse arrival time in the TDC modules, whose clock was started every beam crossing by a signal from a pickup electrode mounted on the beam pipe. A schematic of the system is shown in Figure 20. The TDC modules were multi-hit TDC's in the sense that, for every module of eight channels, up to 16 pulses could be timed every event. Thus a wire could have pulses from several tracks timed in the same event. In practice the minimum allowable track separation was found to be around 5 mm; below that value the pulses tended to overlap and track separation was not possible.

The drift chamber electronics was cycled every beam crossing; that is, the arrival times of all signals were digitized for a period of 500 ns (1000 ns) for the IDC/CDC (PDC) resp. The longer gate time in the case of the PDC's is necessary because of the longer drift time. If an event passes the trigger logic, then all of

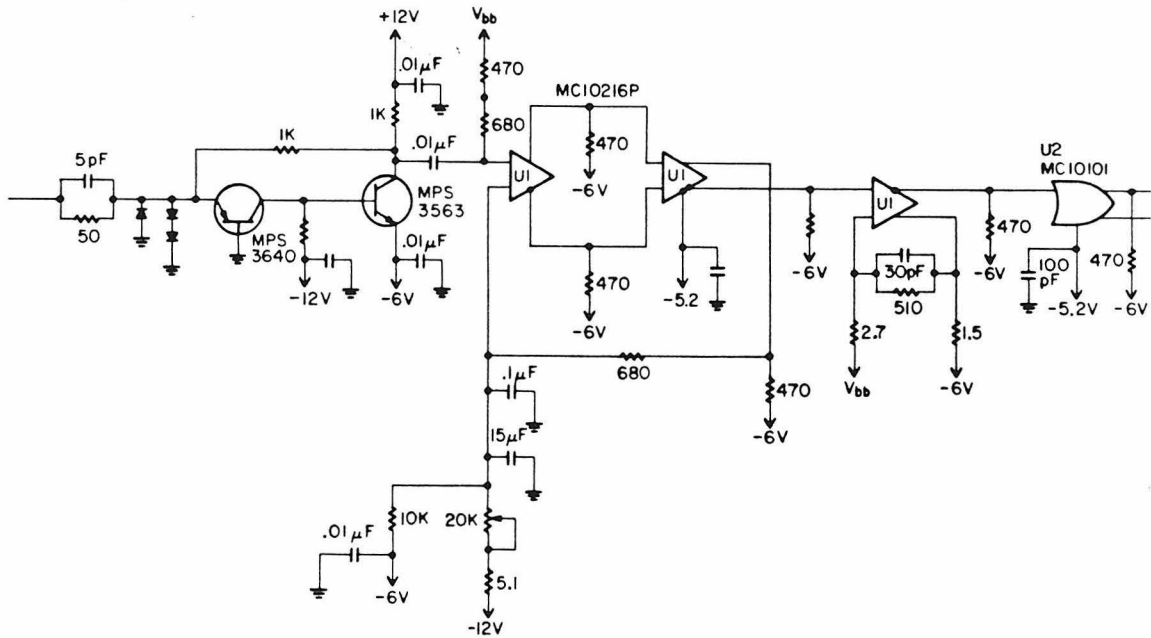


Figure 19. A schematic of the preamplifier/discriminator circuit used to sense pulses coming from the PDC wires. The circuit had a discriminator threshold in the range 1-5 *mV*.

PDC Data Pathway:

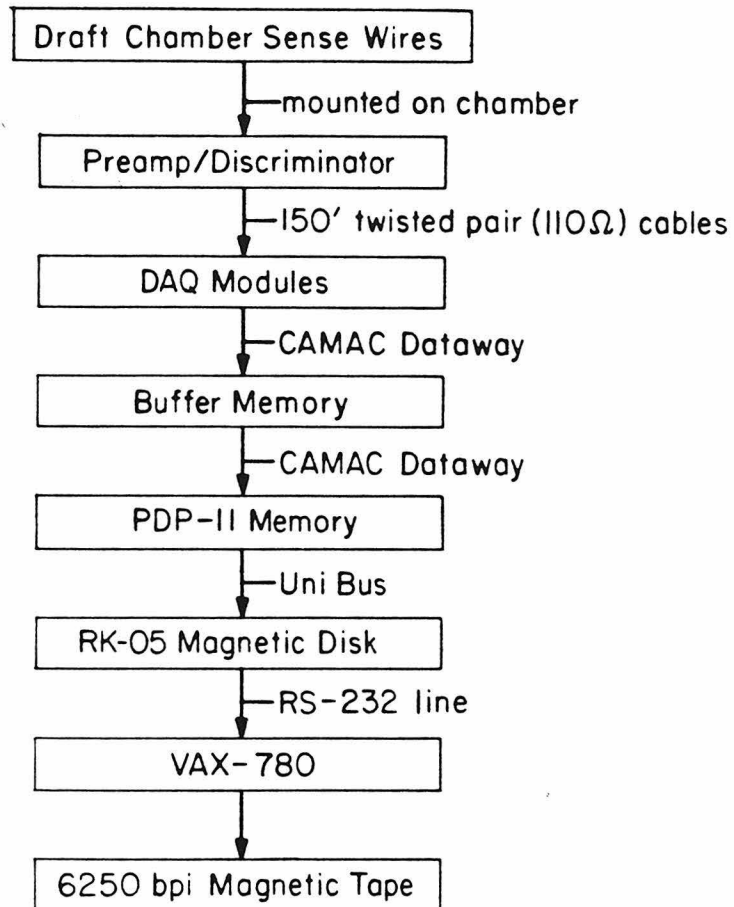


Figure 20. A schematic of the PDC data acquisition system.

the CAMAC crates in the drift chamber systems and counter systems are read into buffer memories and finally into the computer. The read cycle took approximately 2.0 ns to complete. The system was dead for that period of time. The typical deadtime fraction was 0.5% - 2.0% during operation.

§§3.2.6 *Cherenkov Counter*

The DELCO Cherenkov counter was designed both to provide substantial coverage of the solid angle around the IP (interaction point) and to provide a large enough amount of light to give good efficiency for particle separation. The counter container itself was divided into two halves. These halves were mounted to steel beam support structures which moved on 'multi-ton' rollers allowing access to the pole-tip and central regions of the detector. The PDC chambers were mounted directly to the Cherenkov container via aluminum brackets.

The interior of each half of the Cherenkov counter is optically divided into nine sections azimuthally (the angle about the beam axis) and two sections in the polar angle (angle from the combined two halves provide Z or beam axis). The 36 equal size cells cover 75% of the 4π solid angle from $45^\circ < \theta < 135^\circ$ and $0 < \phi < 2\pi$.

Each cell contains a focusing optical system made out of an ellipsoidal mirror combined with a flat mirror. The mirrors have one ellipsoidal focus at the IP and the other at the phototube face. In addition, there is a non-focusing compound parabolic collection (Winston cone) located at the phototube face providing supplementary light collection. A diagram of the optical system is shown in Figure 21.

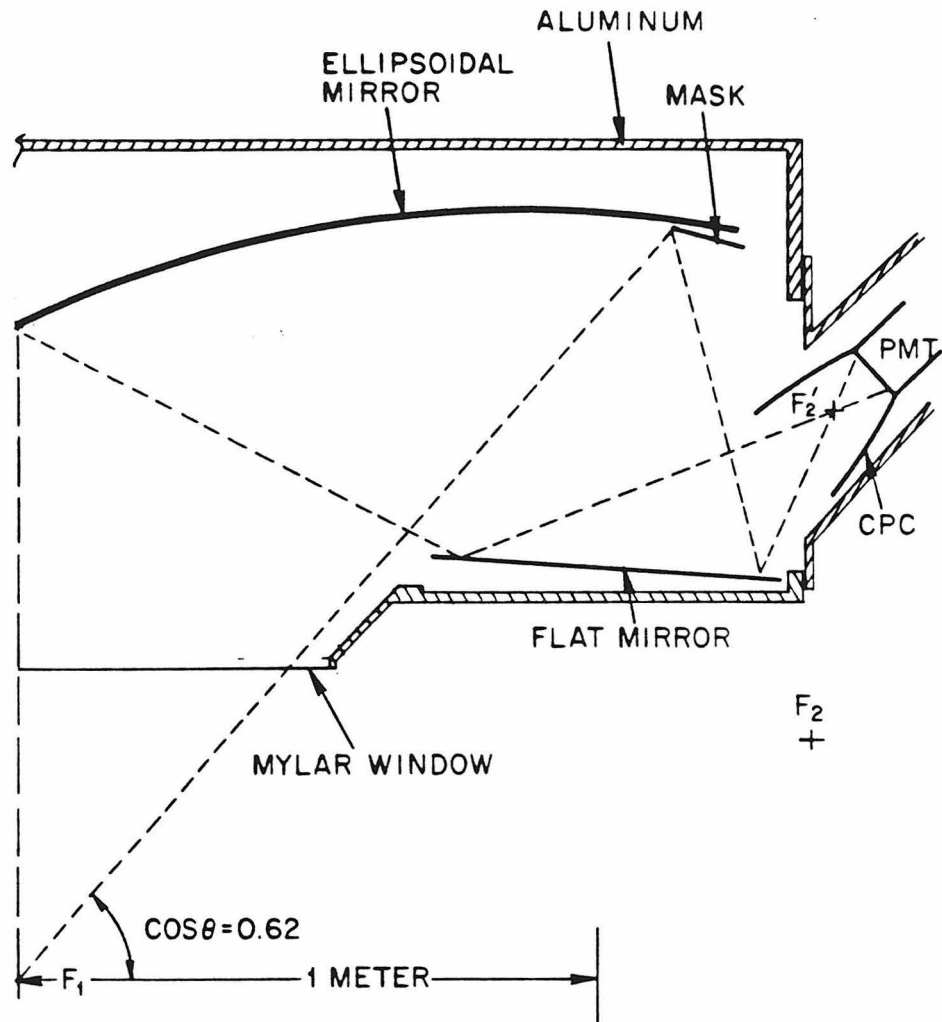


Figure 21. The optics of the Cherenkov counter cells consisted of two mirrors plus a light collection cone. One mirror was a section of an ellipsoid of revolution while the other was a flat mirror. The collection cone was a compound parabolic collector and fit inside the magnetic shielding of the phototube.

The phototube (RCA8854) was held in an assembly formed by a cast aluminum housing bolted to the Cherenkov counter container. The casting was lined with magnetic shielding to protect the phototube from the fringe fields produced by the magnet. This shielding was formed from four concentric cylinders of metal, the outer two of high purity iron and the inner two of a nickel-iron alloy as shown in Figure 22. Combined, the effective shielding factor was roughly 200-500. Any additional field in the vicinity of the tube face was removed by a small 15 cm diameter bunching coil of 100 windings carrying approximately .1 amp of current. This coil was located inside the magnetic shielding at the phototube face, concentric with the phototube.

The counter was calibrated by using electrons from Bhabha scattering events and electrons from hard initial state electron brehmsstrahlung processes. These latter events resulted in a single low energy electron in the detector and were hence named '1e' events. The pulse-height distribution for electrons from Bhabha events is shown in Figure 23. This pulse height has been corrected for path length in the counter and shows the expected yield for a 100 cm path length. The path length varies over each cell from 55 cm to 100 cm. A more detailed description of the Cherenkov system may be found in Reference 23.

§§3.2.7 *Barrel Shower Counters*

The barrel shower counter (BSH) system was taken directly from the SPEAR DELCO apparatus²⁴. It has 24 segmentations azimuthally and two segmentations in the polar angle. The counters are arranged in six sextants forming the sides of a

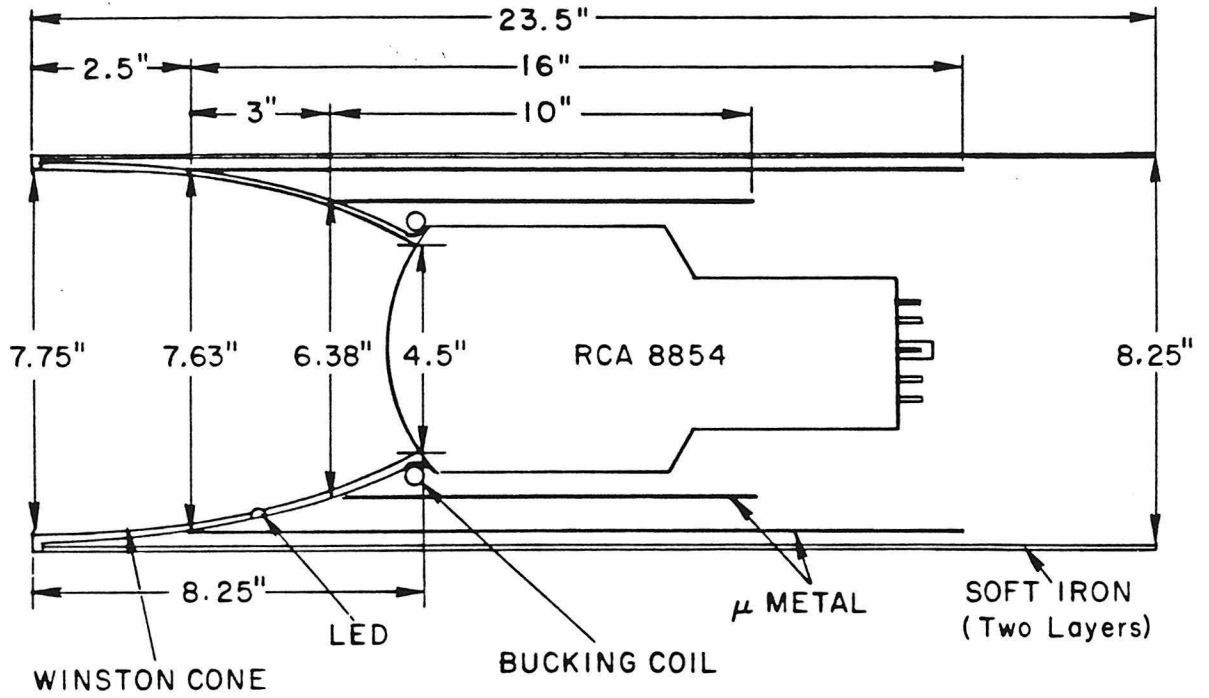


Figure 22. The Cherenkov phototube assembly which includes the magnetic shielding, light collection cone, and phototube.

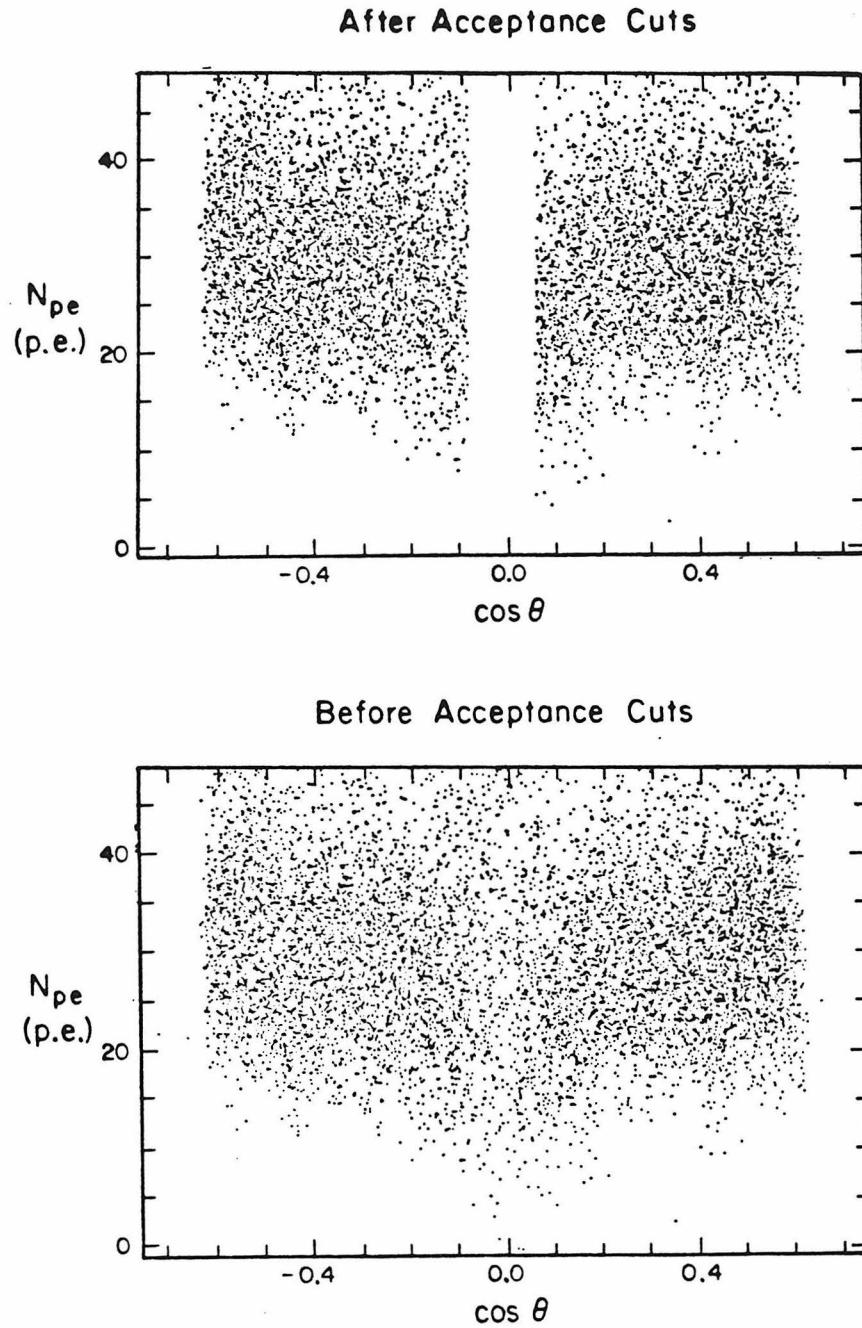


Figure 23. The pulseheight distribution in the Cherenkov counter vs. $\cos \theta$ as measured for electrons from Bhabha scattered events. this is shown both before and after the acceptance cuts used in the kaon analysis.

hexagonal cylinder. Each of the 48 shower counters is divided into three layers, A, B, and C, which are each viewed by a AMPEREX 56 DVP phototube. Each layer of NE-110 scintillator is preceded by a plate of lead which is two radiation lengths thick (1.1 cm), as shown in Figure 24.

The shower counters allow the detection of photons and electrons which cause electro-magnetic showers in the lead and scintillator of the counter. A treatment of the physics of electron and photon showers may be found in Reference 25. The calibration of these counters was done using muons and pions from $2 - \gamma$ interactions and also the 1e sample (hard electron bremsstrahlung). The pulse height distributions for tracks from μ -pairs and Bhabha events is shown in Figure 25. The electron shower distribution in the three layers was modeled using the universal shower curve as may be found in Ref. 26.

§§3.2.8 *Time of Flight Counters*

The time of flight (TOF) counters were simple bars of 1.0 in. by 8.0 in. scintillator with AMPEREX 56 AVP phototubes at either end. Their purpose is to accurately measure the arrival time of particles at the scintillator. This allowed for the determination of the particle velocity and enabled one to identify particles which have a β less than ~ 0.85 . The 52 TOF counters were organized into 6 sextants with either 8 or 9 counters in a given sextant. The scintillator was PILOT-Y and NE-110 with good timing characteristics.

Calibration of the TOF counters was done using the 1e (one electron) data sample where corrections to the time were made according to the pulse height

Barrel Shower Counter Module

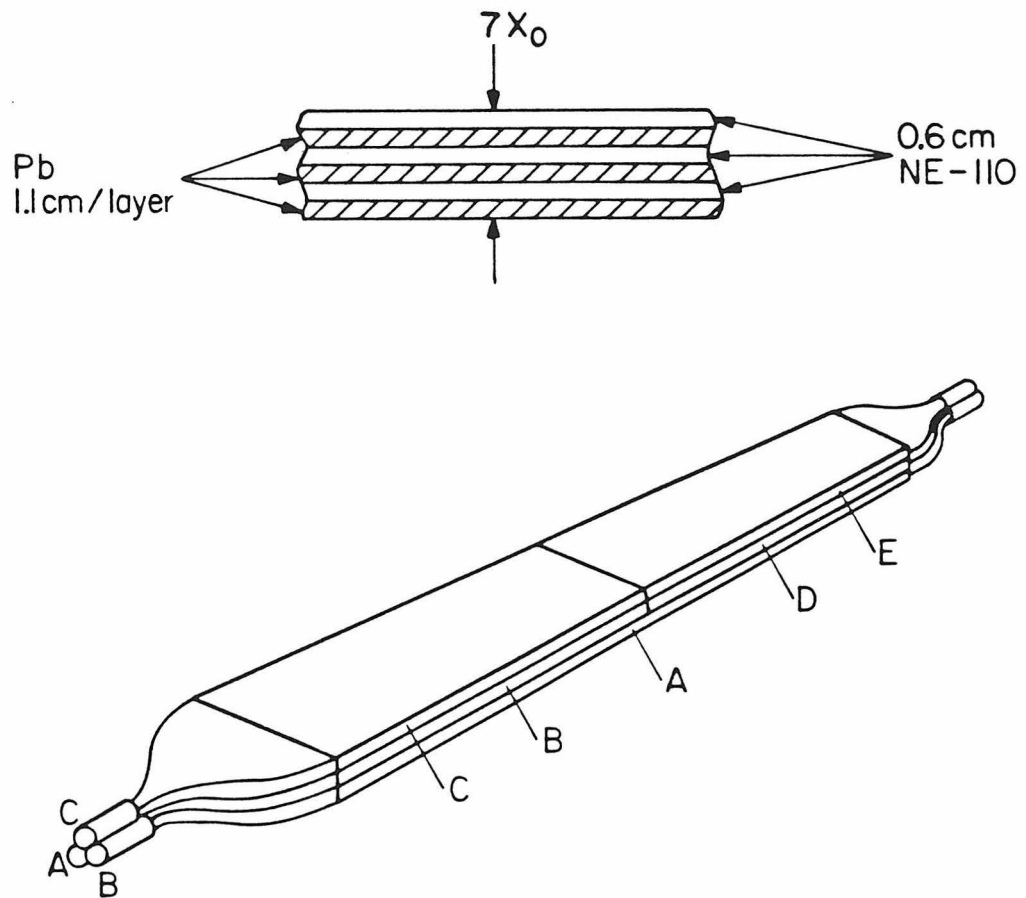


Figure 24. The Barrel Shower Counter (BSH) system consisted of three alternating lead/scintillator layers. The three layers were viewed by separate phototubes.

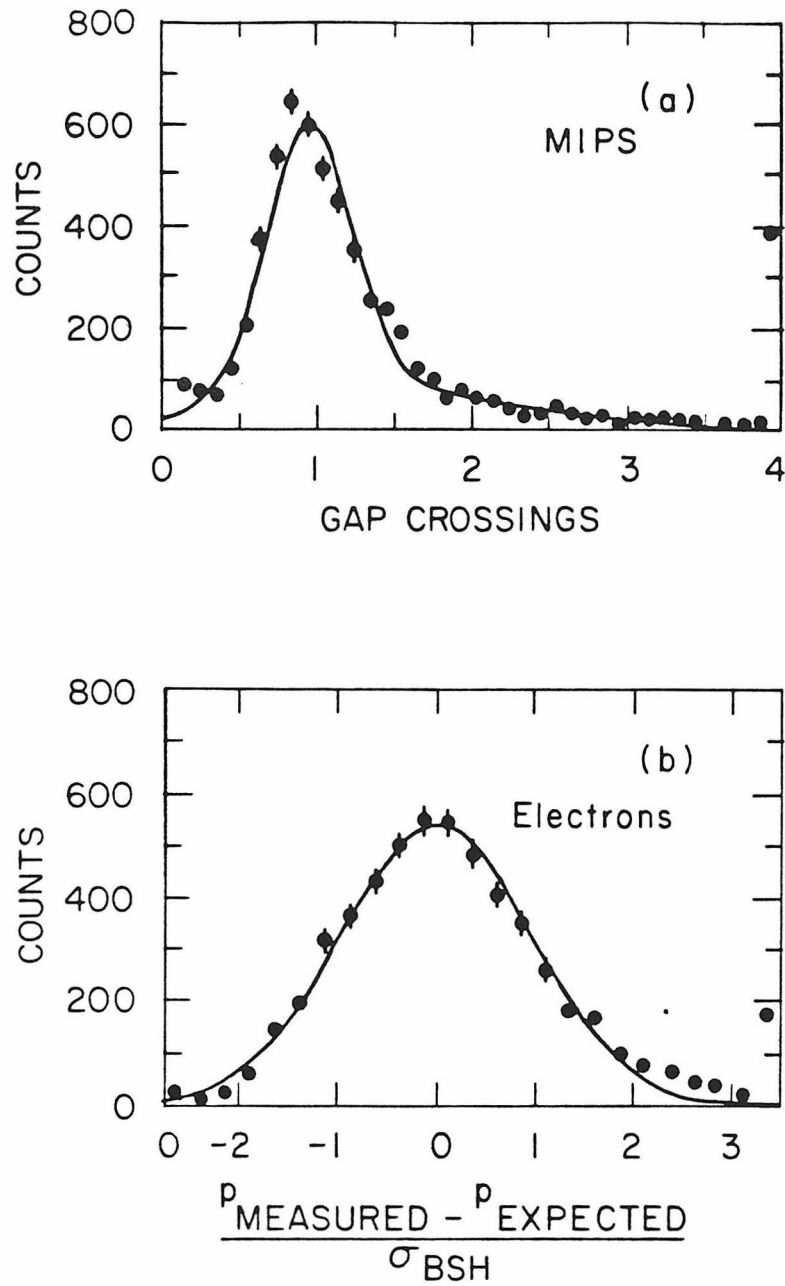


Figure 25. The Barrel Shower Counter response to minimum ionizing particles and to electrons. The electron response is shown as the difference between the measured response and the response predicted by the universal shower curve.

observed in the phototube. The counters were found to have a resolution of 0.30 ns as shown in Figure 26. These counters were primarily used in analysis other than the τ analysis. In this thesis they are used to discriminate against cosmic rays which may be distinguished by their early arrival times and late exit times from the detector.

§§3.2.9 Pole-tip Shower Counters

The pole-tip shower counters were designed to cover the pole-tip regions of the magnet with a device sensitive to both charged particles and photons. The shower counters were arranged in pie-slice shaped wedges on the pole-tip of the magnet. There were eighteen wedges per pole of the magnet, covering the pole-tip from an inner radius of 15 cm to an outer radius of 50 cm. Each wedge of the pie was a five-layer sandwich of NE-110 scintillator (6.35 mm thick) with one radiation length (5.5 mm) of lead. The light was conducted from the scintillator via a BBQ wave shifter bar and then a light pipe to a phototube located outside the magnetic field region.

The pole-tip counters were calibrated by using Bhabha's scattering events which were recorded by a special event trigger. The pulse height calibration was adjusted so as to match expectations for electron showers of $14.5 \text{ GeV}/c^2$.

The pole-tip counters were used mainly as a veto against unwanted particles in the pole-tip region. In this way the tracking chambers were complemented in the pole-tip region by counters which were sensitive to both photons and charged particles.

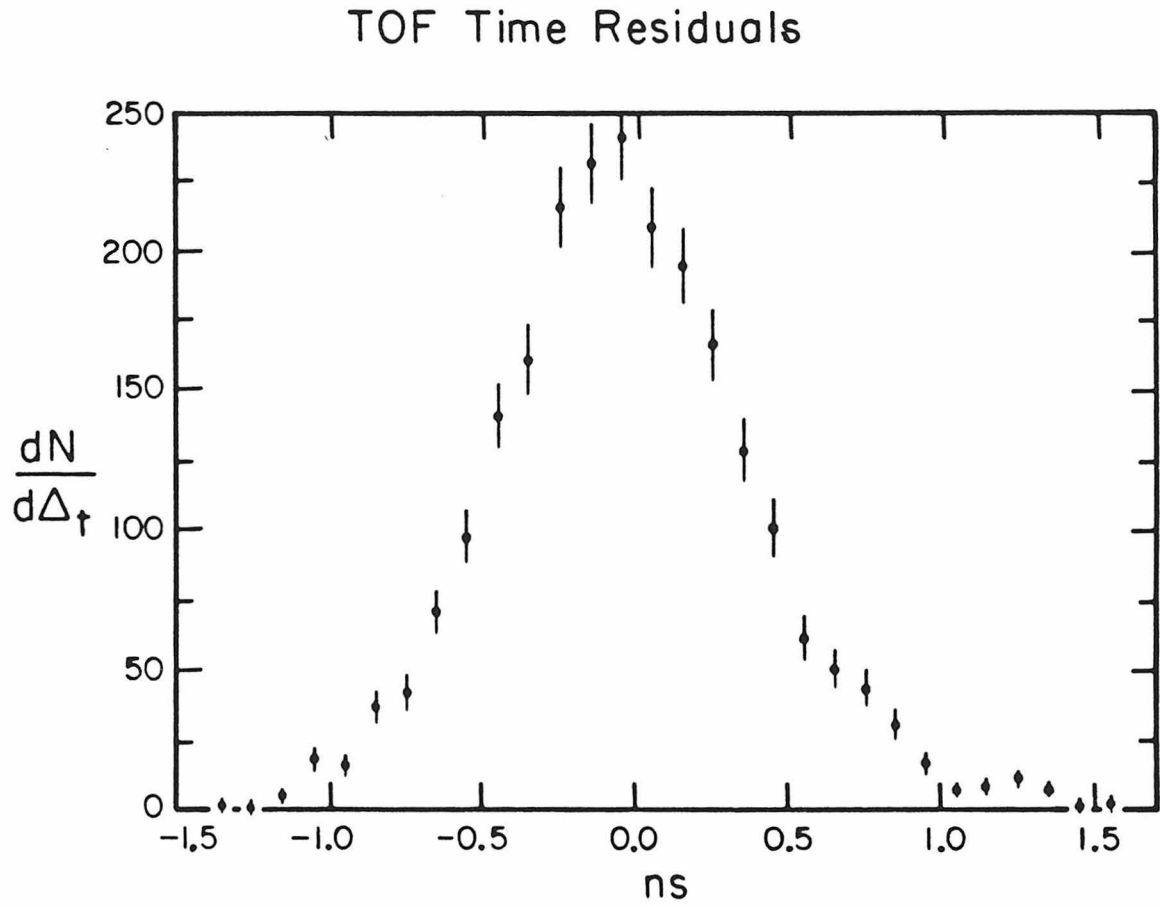


Figure 26. The time residual distribution for muons from $e^+e^- \rightarrow \mu^+\mu^-$ events. The counters were able to determine the masses of particles with a β less than 0.85.

§§3.2.10 Luminosity Monitors

The luminosity monitors served as the run-to-run measure of the integrated luminosity of the colliding beams. They counted the number of Bhabha scattered events, per run interval, while the experiment was alive (*i.e.*, waiting to trigger on an event). In addition, a number of event's containing these Bhabha's were recorded onto tape via a special trigger. These were used later for calibration purposes.

The monitors themselves consisted of six pairs of shower counters positioned at a distance of 270 cm on either side of the interaction point. The monitor itself is divided into two halves each containing six shower modules. The modules were constructed of a lead scintillator sandwich of sixteen radiation lengths with sixteen plates of lead and sixteen plates of NE-110 scintillator. The light as in the case of the pole-tip shower counters is collected via a BBQ wave shifter plus a light guide. A cool beer for anyone reading this sentence (on the author). A diagram is shown in Figure 27.

The monitor's luminosity scale was calibrated by directly calculating the acceptance of the monitor and by comparing it with wide and Bhabha events in the central detector region. The latter method proved to be more accurate because of uncertainties in the monitors transverse position. The monitor, because of its high event rate, was used to measure all luminosities after being calibrated by the wide angle Bhabha events.

Luminosity Monitor:

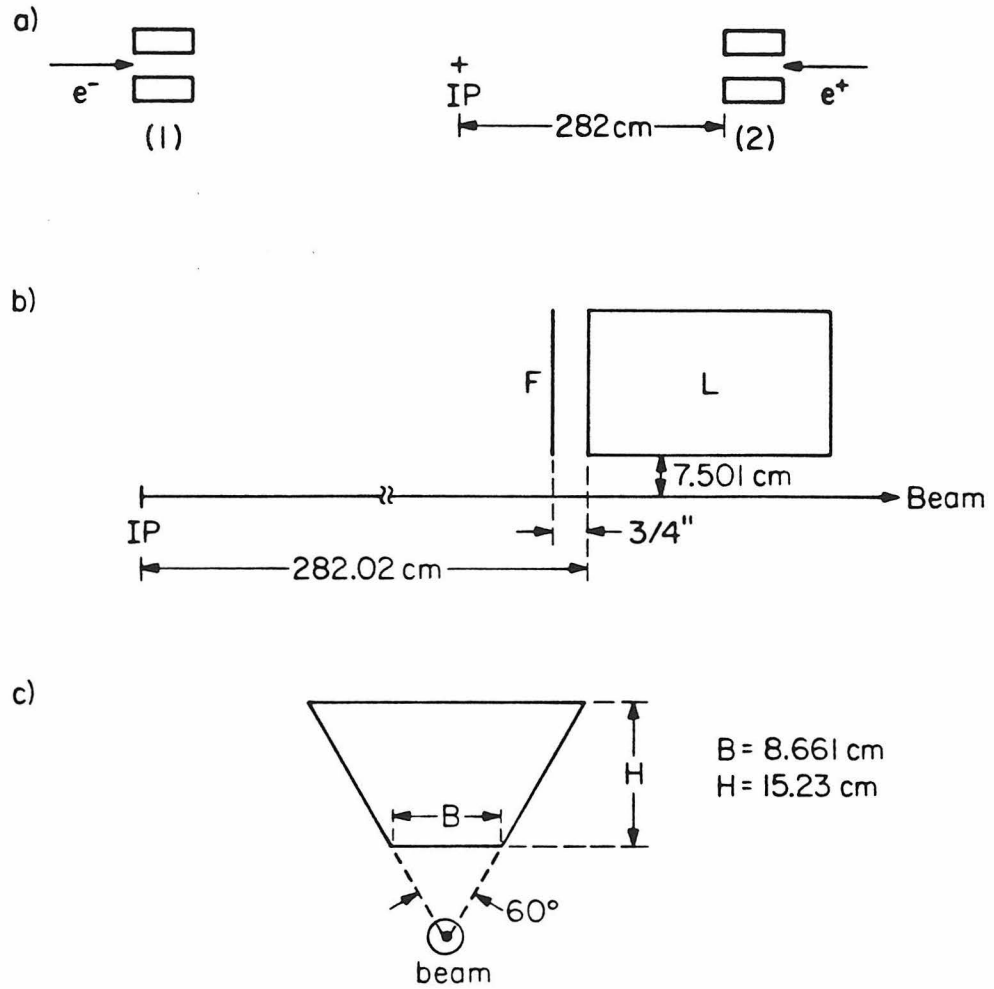


Figure 27. The luminosity monitor system. This counter system was designed to measure the rate of Bhabha scattered events at small angles with respect to the beam (in the polar angular range of 26-93 mrad).

§§3.2.11 *Trigger*

The hardware trigger was designed to reduce the online trigger rate to a level which could be written onto magnetic tape. A further requirement was that it have a minimum bias towards events coming from e^+e^- interactions. The trigger decision had to be made within the 2.2 ns between beam collisions so that there were severe limitations on what type of scheme could be employed.

There were four primary components to the trigger scheme: the central drift chambers, the barrel shower counters, the Cherenkov counter, and the pole-tip/luminosity monitor shower counters. The pole-tip/luminosity shower counters play an important role in the triggers used for making the luminosity measurement. The triggers using these counters were designed to trigger on Bhabha scattered events where two high energy back-to-back electrons impact the shower counters. These triggers, because of their high frequency, were prescaled so that only a fraction of them were written to tape.

The central drift chambers were used to decide whether or not a charged particle had passed through the chamber on a given event. In order to do this each wire was latched at the input of its time digitizer. These latches were then strobed out of each chamber layer synchronously. The presence of a charge particle was indicated if several pairs of layers recorded latches within a window in azimuthal angle. The system checked itself by feeding a test bit at the end of the strobe chain which was checked at the end of each strobe cycle. An alarm sounded if this bit failed the test.

The barrel shower counters were used in two ways in the trigger in order to obtain overlapping and redundant trigger schemes. The first scheme was to combine the latches of the three individual phototubes in a given shower module to form a coincidence (two out of three) which indicated the presence of a particle traversing

the counter. For example, a trigger was subsequently devised using the requirement that two shower modules latch in conjunction with the presence of a charged track in the event. This trigger requirement was called the 'X2S' trigger. The second way in which the shower counters were used in the hardware trigger was to sum the pulse height from all of the phototubes in the system in a linear fan-in module to obtain a crude measure of the energy deposited into the system for the event. By discriminating this signal, a rough energy threshold was set at $1.5 \text{ GeV}/c^2$ (electrons and photons only). As an example a trigger which was completely independent of the charged track requirement of the chambers was obtained by requiring this energy latch in conjunction with two of the individual shower module latches. This allowed a check on the charged track trigger systems and showed an inefficiency at the 1% level in the charged track trigger system.

The Cherenkov counter system was used in the trigger in order to overlap with the shower counter system trigger. The latches in each sextant (6 latches per sextant) were logically summed and similarly the shower counter modules in a sextant were logically summed to form a latch for each sextant. These latches were then to form a coincidence for each sextant between Cherenkov latches and shower counter module latches in the sextant.

These and other triggers allowed data to be taken at a rate of 1-2 Hz during normal operation. A summary of triggers is shown in Table 4. The triggers responsible for the events in this analysis were primarily the 'X2S' trigger, the 'X2SG' trigger, and the 'XKS' trigger.

Table 4. The event triggers which were used in the DELCO experiment to select $e^+e^- \rightarrow \tau^+\tau^-$ events. They are overlapping and their efficiencies were 98%.

Event Triggers	
Trigger	Requirement
X2S	2 S Counters plus charged track
XKS	S and K Counters plus charged track
X2SG	2 S Counters plus neutral energy

§§3.2.12 Data Acquisition and Online Monitoring

A schematic of the data acquisition system is shown in Figure 28. It provided a fast (≈ 2 ms) event reading cycle through a set of scanners which loaded data into a buffer memory. The buffer memory was in turn read by the PDP-11 computer where the data were written to a magnetic disk and then shipped over to a VAX 780 computer which finally wrote the event to tape. A subsample of the data was analyzed by a monitor program which ran on a VAX 780. A software filter selected events of the '1e' category containing one low energy (200 MeV and above). These events were then analyzed with respect to the counter and chamber responses. Thus online efficiencies, gain changes, and other quantities were available on a run-by-run basis. In particular, the shower counter efficiencies and gains, the Cherenkov counter efficiency and pulse heights, and drift chamber efficiencies and resolutions were all monitored in this manner.

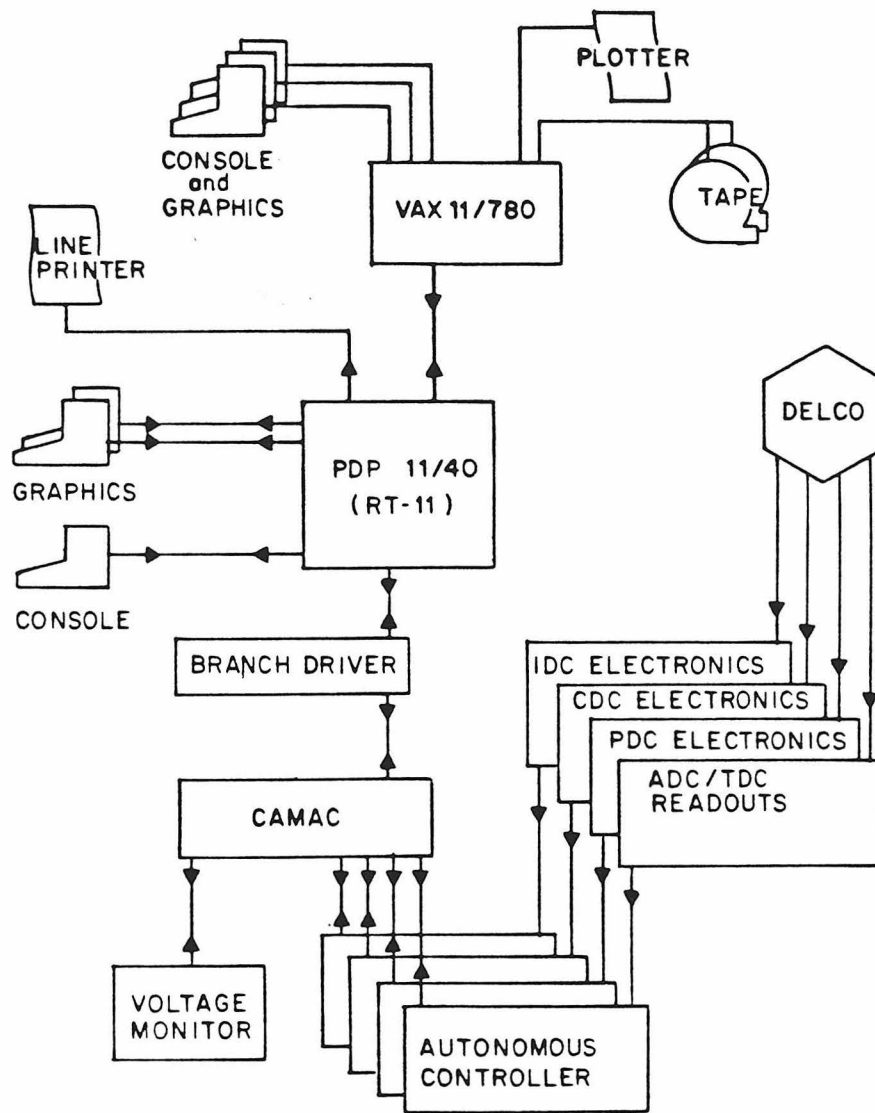


Figure 28. The data acquisition system for DELCO.

§§3.2.13 *Offline Software*

This subject, it seems to me, has always been given less attention than it rightfully deserves. A great deal of effort was put into the software code and, in fact, there is a good chance that more time was spent developing it than was spent developing the hardware. In any case, if I fail to describe it in enough detail to give justice to it, I hope I will not be criticized too greatly.

The software was arranged in two streams. One was concerned with finding tracks in the detector and extracting momentum and location information from the tracks. The other was concerned with counter (*e.g.* , Cherenkov , shower, and TOF counter) information and correlating it with the track information.

The tracking code first unpacked the raw event drift times and wire numbers and then transformed these raw numbers into drift distances from the wire locations. After this, a 'road' finding algorithm found groups of hit wires, called roads, which had common azimuthal angles. These roads were then searched individually for tracks in the $x - y$ plane (perpendicular to the beam axis).

In order to determine whether or not a real track existed, a fit was made to the recorded drift time positions. The coordinates were chosen so that a simple linear fit was possible in order to reduce the amount of computer CPU time spent in the algorithm. The coordinates chosen for the fit were the ϕ (azimuthal) angle of the track and a rescaled radius, \tilde{r} , which was a function of true radius and the momentum of the track. The form of the rescaled radius was generated using the measured field map and was generated so that the following equation was valid:

$$\phi = \frac{K}{\tilde{r}} \quad ,$$

hence making a linear fit possible. The other projection of the track ($r - z$ projection) was found using a similar technique. Once a track candidate was found, along

with a crude estimate of its momentum, a precise determination of the momentum, position, and direction is made by fitting the drift chamber measurements to an exact model of the track. This model was provided by numerically integrating the Lorentz force equation using the measured field map as the magnetic field. The equation is a function of the variables: $\frac{1}{p_{\perp}}$, the momentum perpendicular to the beam axis; $\tan\lambda$, where λ is the dip angle of the track out of the $x - y$ plane; ϕ , the azimuthal angle; z , the position along the z axis; and X_T , which is the transverse position of the track from the beam axis at the closet point of approach. It is then possible to calculate the derivatives of the χ^2 function of predicted minus measured drift distances with respect to the track parameters $(\frac{1}{p_{\perp}}, \tan\lambda, \phi, z, X_T)$ in a linearized approximation and perform an iterative minimization to find the optimum track parameters. The χ^2 function is given by:

$$\chi^2 = \frac{1}{2} \sum_{wires} \sum_i \frac{(d_i^{pred} - d_i^{meas})^2}{\sigma_i^2} \quad (3)$$

where d is the distance to the wire and σ is the measurement error of the wire.

Once tracks are found, it is possible to predict the response they induce in the counters under the assumption of a given particle type. This response is then compared with the measured values in the given counters. This allows for particle identification over various momentum ranges. In this analysis kaons are identified from a sample of kaons, pions, electrons, and muons by comparing the expected Cherenkov response for kaons with the observed momentum value. Kaon identification will be discussed in the next chapter.

Chapter 4. Analysis of the Data

This chapter discusses the analysis of the data. The objective of this analysis is to measure the branching ratios for the decay modes: $\tau^\pm \rightarrow K^\pm \nu_\tau$, $\tau^\pm \rightarrow K^\pm \nu_\tau + n\pi^0$, $\tau^\pm \rightarrow K^+ K^- \pi^\pm \nu_\tau$, and $\tau^\pm \rightarrow K^\pm \pi^+ \pi^- \nu_\tau (\pi^0)$ and to obtain a limit on the τ neutrino mass from the mode $\tau^\pm \rightarrow K^+ K^- \pi^\pm \nu_\tau$. In order to achieve this goal there are several preliminary steps needed to describe how the data were processed into a usable form. In addition the luminosity for the data set is needed for the branching ratio measurements. These topics are discussed in the first section.

This chapter would not be complete without a discussion of the classification of the data sets and in particular how the τ data sets were arrived at, even though the cuts used to form them do not have a dramatic effect on the final results. To this end, the second section describes these data filters and the philosophy behind them. The general properties of $\tau^+ \tau^-$ events are compared to possible background sources to justify these filters.

The principal tool used in this investigation is the Cherenkov identification of kaons. Since this plays a central role in the analysis, the third section is devoted to describing how this is accomplished in our apparatus for the case of $\tau^+ \tau^-$ events. The criteria used for kaon identification are then used in the fourth and fifth sections as part of the event selection procedures used to obtain the final data samples.

The single charged particle, or single prong, decays of the τ , where the single prong is identified as a kaon, form the data sample from which the branching ratios of the decays $\tau^\pm \rightarrow K^\pm \nu_\tau$ and $\tau^\pm \rightarrow K^\pm \nu_\tau + n\pi^0$ are determined. The

fourth section follows the selection of these events. After making the selection and estimating the backgrounds present in the data sample, the sample is divided into two categories by using the amount of neutral shower counter energy observed coming from the decay to detect the presence of π^0 's in the decay. These samples then yield the required branching ratios.

The selection of the events with multi-prong decays which contain charged kaons is somewhat similar to the single prong decay event selection. The selection criteria and data sample backgrounds are described in the final section on multi-prong decays. We are able to separate the events into different groups by the number of charged kaons found and by the sign of the charge of the kaon with respect to the parent τ charge. These groups of data then allow for the determination of the branching ratios $\tau^\pm \rightarrow K^+K^-\pi^\pm\nu_\tau$ and $\tau^\pm \rightarrow K^\pm\pi^+\pi^-\nu_\tau(\pi^0)$, where the (π^0) denotes the possibility of a π^0 in the final state. The events where two charged kaons have been identified are then used to obtain an upper bound on the τ neutrino mass. To do this, the difference between the invariant mass of the τ particle and the invariant mass of the $KK\pi$ system is used as a measure of the energy which is available to the τ neutrino.

§4.1 The Data

The DELCO apparatus was operated over a period of four years, from the fall of 1980 until the summer of 1984. During that time the luminosity of the PEP ring was increased almost tenfold, from $1 - 3 \times 10^{30} \text{cm}^{-2} \text{s}^{-1}$ to $1 - 3 \times 10^{31} \text{cm}^{-2} \text{s}^{-1}$ as the magnet lattice of the ring was improved over time.

The 1980-1981 running season was a trial run for DELCO. The inner proportional chamber used for tracking was found to be inadequate and hence was replaced by a six-layer drift chamber. In addition, the outer planar drift chambers were increased from four layers to six layers. After these changes the detector hardware remained essentially stable through the end, 1984. This was the configuration of the detector for the data used in this thesis. Other minor changes include a change of drift chamber gas at the end of 1982. The gas was changed from a mixture of argon-ethane (55:45) to a mixture of argon-carbon dioxide-methane (89:10:1). The primary reason for this change was the degradation, induced by the polymerization of carbon (from the ethane gas) onto the chamber wires, of the drift chamber performance in a high radiation environment near the beam pipe. Concurrently, another small change was implemented. A set of pulse shaping amplifiers were added to the inner 16 layers of the drift chamber system in order to obtain a cleaner signal. The combined effect of these last two changes was to worsen the position resolutions somewhat. However, this loss was recovered by improving the rise time characteristics of the pulse shaping circuits after 1983. These effects have been included in the simulation of the drift chambers.

§§4.1.1 *Luminosity Measurement*

In order to determine the branching ratios for the processes we are considering it is necessary to determine the luminosity normalization of the data set that is to be used. There are many ways to determine the data sample luminosity. The method chosen in the present analysis is to use the normalization derived from

wide angle Bhabha²⁷ events (e^+e^-) which are present in the same data sample as the τ data. The Bhabha scattering process has a production cross section which is well understood theoretically. A Monte Carlo generator¹⁰, which includes radiative corrections to order α^3 , is used to calculate the efficiency after full simulation of the detector is performed on the generated events. Since the events are contained in the central region of the detector, they can be studied using tracking information.

Another method of calculating the luminosity is to use the luminosity monitor which records the rate of narrow angle Bhabha events near the beam axis. Because the differential cross section for this process, $\frac{d\sigma}{d\cos\theta}$, is peaked in the forward direction, the luminosity monitor records many more events than the wide angle Bhabha events in the central detector. The optimum method for finding the luminosity for a particular data set is to use the luminosity monitor result for the data set calibrated by the wide angle Bhabha measurement.

There is another well-understood process which can be used to determine the luminosity. This is muon pair ($\mu^+\mu^-$) production and since it is a purely QED process it is well understood theoretically. It provides a cross check to the Bhabha process luminosity but is limited by poorer statistics. The $\mu^+\mu^-$ result is consistent with the Bhabha result within errors as shown in Table 5. In Fig. 29 and in Fig. 30 there are shown angular distributions for the Bhabha and $\mu^+\mu^-$ event samples used to measure the luminosity.

Table 5. Luminosity results for Wide Angle Bhabha events and $\mu^+\mu^-$ events for each year.

Luminosity (pb^{-1})		
	e^+e^-	$\mu^+\mu^-$
1982	23.6 ± 1.2	22.4 ± 1.1
1983	71.4 ± 3.6	65.8 ± 3.3
1984	50.6 ± 2.5	47.7 ± 2.4
total	145.6 ± 7.3	135.6 ± 6.8

§4.2 Event Selection Overview

The properties of events produced in the reaction $e^+e^- \rightarrow \tau^+\tau^-$ at $29GeV/c$ center of mass energy differ greatly from events produced in other e^+e^- reactions at the same energy. It is therefore useful to examine some of these properties and contrast them with the other reactions which serve as possible sources of backgrounds. These other reactions are composed of the first order QED processes, such as $e^+e^- \rightarrow e^+e^-$, $\mu^+\mu^-$, and $q\bar{q}$, and higher order processes such as $e^+e^- \rightarrow e^+e^-e^+e^-$, $e^+e^-\mu^+\mu^-$, and $e^+e^-q\bar{q}$.

The decays of the τ have, as mentioned in Chap. 2, one charged track in the final state 85% of the time and three tracks only 15% of the time. Hence, events of the reaction $e^+e^- \rightarrow \tau^+\tau^-$ will appear in the detector with two, four, or six tracks in the event. Furthermore, because of the high velocity of the τ particle ($\beta \approx 0.98$) the daughter charged particles are generally collimated in the direction of the parent τ 's original trajectory. When events are divided into two hemispheres

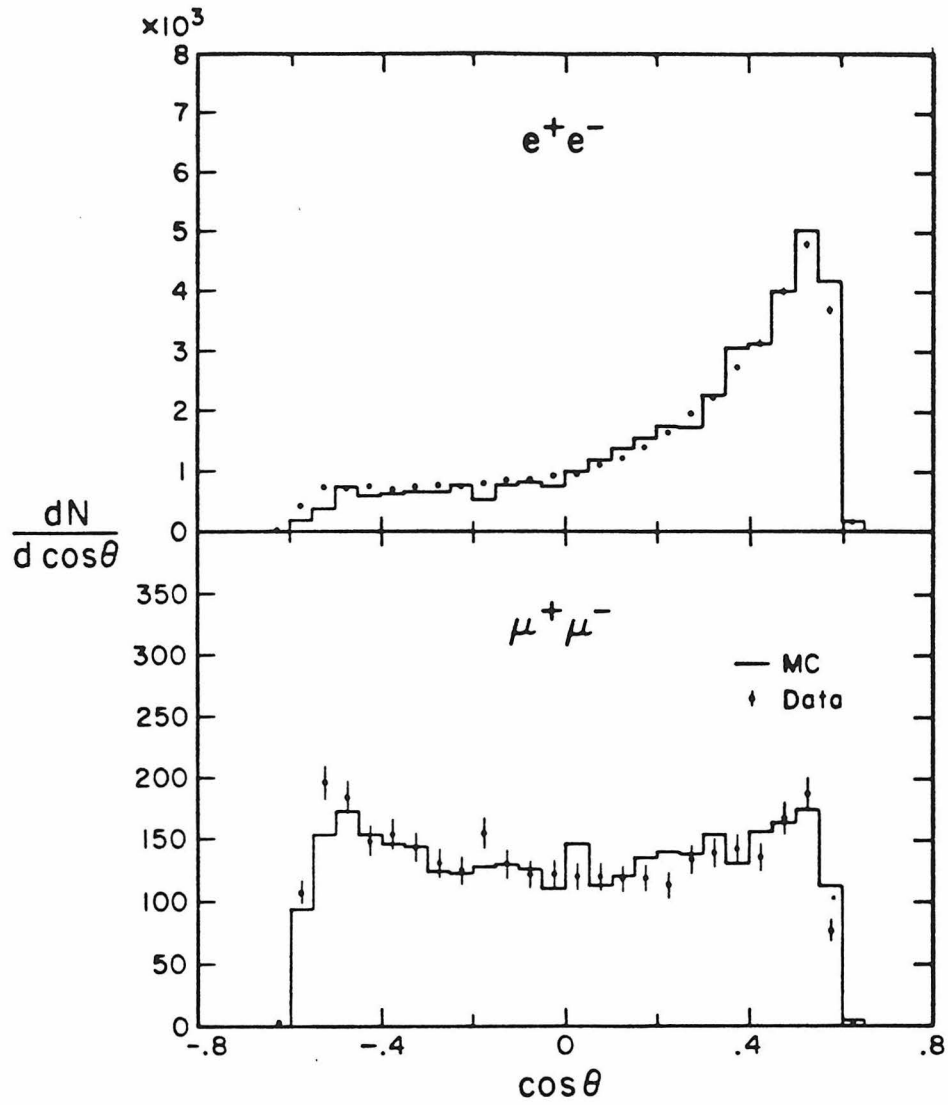


Figure 29. Distributions in $\cos\theta$ for the positive particle in Bhabha and $\mu^+\mu^-$ events. The Monte Carlo predictions are shown in solid lines.

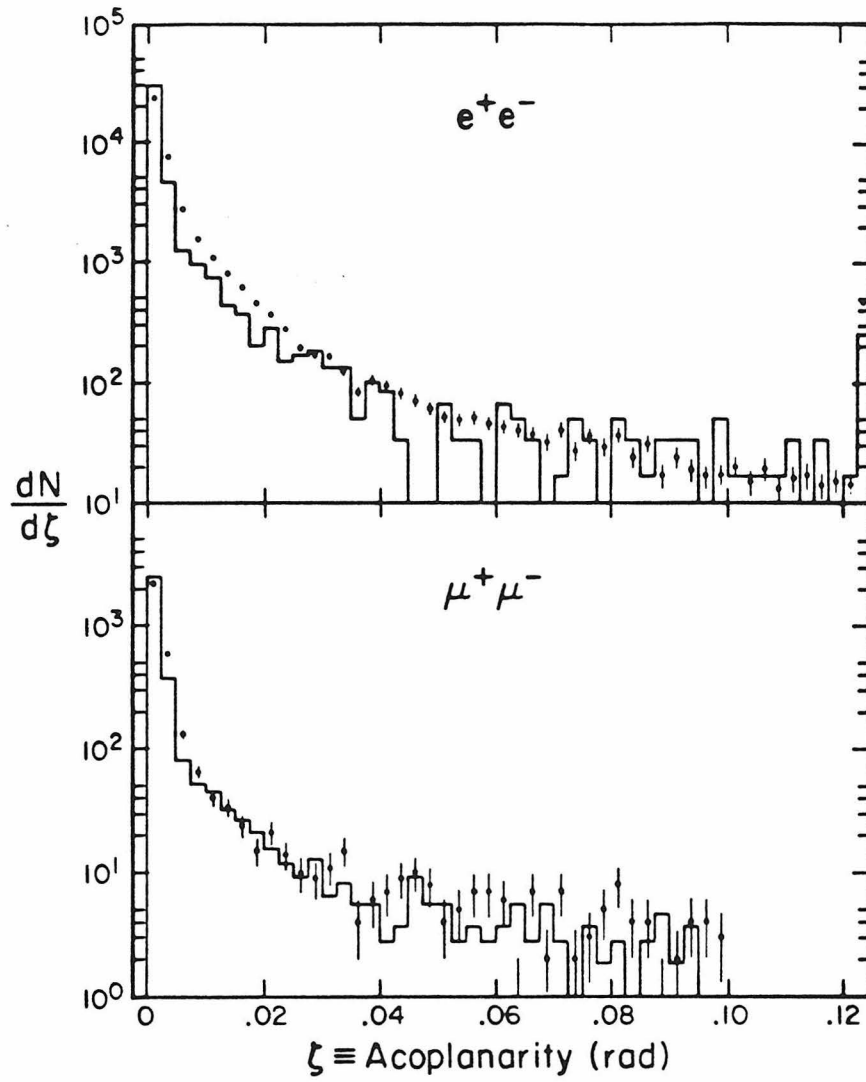


Figure 30. Distributions in acoplanarity for Bhabha and $\mu^+\mu^-$ events. The Monte Carlo predictions are shown in solid lines.

by the plane normal to the $\tau^+\tau^-$ flight axis and the number of tracks counted in each hemisphere, the events typically fall into three classes: 1-1 events (one track in each hemisphere) 72% of the time, 1-3 events (one track in one hemisphere and 3 tracks in the other) 25% of the time, and 3-3 events (three tracks per hemisphere) 2% of the time. Since most of the events fall into the 1-1 and 1-3 categories and since they have the lowest background, the analysis uses them exclusively.

The decay products of a τ also include a τ neutrino which passes out of the apparatus unobserved. The neutrinos can carry, depending upon the decay mode, a substantial fraction of the parent τ 's energy. The energy in the event, which never contains the two neutrino energies, is always less than the center of mass energy of the beams. However, because of the relatively low particle multiplicities, the observed energy contained in charged particles is still relatively high. The kinematics of $\tau^+\tau^-$ production dictates that the τ^+ flight direction be nearly anti-collinear with the τ^- flight direction. Consequently, the daughter particles also tend to be anti-collinear. The fact that the daughter particles are not precisely anti-collinear is useful to separate $e^+e^- \rightarrow \tau^+\tau^-$ events from $e^+e^- \rightarrow e^+e^-$ and $e^+e^- \rightarrow \mu^+\mu^-$ events.

The DELCO experiment recorded several million triggers(events) during the course of its operation. The expected number of $\tau^+\tau^-$ events for a $150pb^{-1}$ data sample with DELCO's trigger efficiency of approximately 65% is nearly 11,000 events. In order to obtain a data set of suitable size for analysis, these millions of trigger events were reduced through a two-step software process to a manageable size of roughly 30,000 events. The filters used in this data reduction were designed to be very efficient for $\tau^+\tau^-$ events and to reject unwanted events such as Bhabha, $\mu^+\mu^-$, hadronic($q\bar{q}$), and $\gamma\gamma$ events. Since most of these requirements are overlapping with later requirements, only those criteria that have an effect on the final answer will be discussed thoroughly. For the sake of posterity all of the first pass selection criteria will be included in Table 6.

Two requirements have an effect on the final result. The first is the 2-prong

Table 6. Data section criteria used to generate the preliminary $\tau^+\tau^-$ data sample. These criteria have a minimal effect beyond defining the acceptance of the apparatus.

First Pass Selection Criteria	
Hardware Trigger	X2S,XKS, or X2SG
In-Time Counter	Cherenkov ,TOF, or BSH
Charged Energy	$E_{ch} > 3.0\text{GeV}/c$
Acoplanarity (1-1 events)	$\alpha > 10.0\text{mrad}$
Thrust/jet (1-n events)	$T > 0.95$
Event Topology	1-n topolgy (n=1,2,3,4,5,6) or 3-3, 3-5, 5-5 topology

acoplanarity cut. This has only a 5% inefficiency for $\tau^\pm \rightarrow K^\pm \nu_\tau$ events which have already passed all other selection criteria, while it removes 65% of the Bhabha events. This proves to be necessary with regard to the Cherenkov efficiency analysis. The second is the requirement on the thrust of the multi-prong jets. This is 98% efficient for $\tau^+\tau^-$ events while removing 80% of the hadronic events from the preliminary data sample.

The largest inefficiency introduced at this point is the hardware trigger, *i.e.* , the inefficiency imposed by the acceptance of the apparatus. The triggering system, discussed in Chap. 3, is modeled in the simulation by checking the predicted responses in the counters to see whether or not they satisfy any of the hardware triggers. Each of the overlapping trigger efficiencies was checked independently against each other using Bhabha and $\mu^+\mu^-$ data. The primary trigger, the X2S trigger, used for $\tau^+\tau^-$ events was found to be greater than 98% efficient over the detector acceptance for $\mu^+\mu^-$ events. The $\mu^+\mu^-$ events give a sensitive test for

inefficiencies of the trigger system because they have only two tracks and deposit a minimal amount of energy into the shower counters. The $\tau^+\tau^-$ events, on the other hand, often have more than two tracks or have photons from π^0 decays. These extra particles mean that the $\tau^+\tau^-$ events will be much less sensitive than $\mu^+\mu^-$ events to trigger inefficiencies so that the measured $\mu^+\mu^-$ inefficiencies may be regarded as an upper bound on $\tau^+\tau^-$ event inefficiencies.

§4.3 Kaon Identification

The DELCO apparatus was designed to allow for the Cherenkov identification of particles. The TOF counters, combined with the momentum measurement, can also be used to separate kaons from pions at momenta below $1\text{ GeV}/c$ and protons from kaons and pions at momenta below $2\text{ GeV}/c$. However, this is not useful in the present case because, at PEP energies, the momentum of the kaons from τ decays is too high. On the other hand, the Cherenkov counter is ideally suited for the identification of kaons from these τ decays. The useful momentum range over which Cherenkov identification of charged kaons is possible is roughly $3.5\text{ GeV}/c$ to $9.4\text{ GeV}/c$. This allows for 45-65% of the kaons produced in a given τ decay channel to be identified, depending on the particular decay channel, as discussed in Chapter 2.

The identification of a particle as a kaon is possible when the momentum of the particle is both above pion threshold and below kaon threshold. In this momentum range, all charged decay products of τ leptons except kaons will produce light in the counter, so that kaons are readily distinguished. There are two ways in which

other particles such as pions can contribute background to the kaon signal. In the first case, if the Cherenkov counter is inefficient, a pion may give a photoelectron signal below the zero level resulting in a false kaon tag. Secondly, a pion which does not emit Cherenkov light because it has a true momentum just below pion threshold may have a measured momentum above pion threshold and also give a false tag. The question of backgrounds from both of these effects is addressed in what follows.

§§4.3.1 Cherenkov Acceptance and Efficiency

To understand the efficiency of the Cherenkov counter we first look at some of the characteristics of Cherenkov light. The number of Cherenkov light photons, per unit length and frequency, given off by a particle of velocity β which is traversing a medium with index of refraction n can be expressed as ^{28,29}

$$\frac{d^2 N}{d\nu dl} = \frac{2\pi\alpha}{c} \left[1 - \frac{1}{\beta^2 n^2} \right] \quad (4)$$

where: α is the fine structure constant, c is the speed of light, and ν is the frequency of the Cherenkov light. For our purposes a more convenient form is

$$\frac{d^2 N}{d\nu dl} = \frac{2\pi\alpha}{c} \frac{n^2 - 1}{n^2} \left[1 - \frac{p_0^2}{p^2} \right] \quad (5)$$

where

$$p_0 = \frac{m}{\sqrt{n^2 - 1}}, \quad (6)$$

Table 7. Particle threshold momenta for various particle types assuming an index of refraction of $n=1.00144$, the effective value for an isobutane radiator.

Particle Cherenkov Thresholds				
Particle	e	μ	π	K
$p_0(\text{GeV}/c)$	0.055	1.98	2.60	9.4

and m and p are the mass and momentum of the particle, respectively. The particle begins to generate Cherenkov light at the momentum of p_0 . The values of p_0 for various particles are shown in Table 7.

In order to estimate the number of photoelectrons produced in the Cherenkov counter phototube one must add up the contributions from each of the accessible frequencies, taking into account the dispersive nature of the gas $n = n(\nu)$. The number of photoelectrons per unit path length may then be written as

$$\frac{dN_{p.e.}}{dl} = \int \frac{d^2N}{dl d\nu} \cdot \epsilon(\nu) \cdot d\nu \quad (7)$$

where $\epsilon(\nu) = T(\nu) \cdot R(\nu) \cdot Q(\nu)$, the quantum efficiency of the system, is the product of the gas transmissivity, the mirror reflectivities, and the quantum efficiency of the photomultiplier photocathode, respectively. The result of the integration in Equation 7 may then be expressed in the form

$$\frac{dN_{p.e.}}{dl} = \frac{dN_{\beta=1}}{dl} \cdot \left[1 - \frac{p_0^2}{p^2} \right] \quad (8)$$

where $p_0 = m/\sqrt{n_{eff}^2 - 1}$. The effects of dispersion in the gas, reflectivity of the mirrors, and quantum efficiency of the photomultiplier are then incorporated into

the two parameters $dN_{\beta=1}/dl$, the number of photoelectrons per unit path length for a $\beta = 1$ particle, and n_{eff} , the effective index of refraction for the system. The average photo electron yield versus momentum is shown in Fig. 31.

Good Cherenkov efficiency is crucial to the kaon identification in this analysis. Cherenkov inefficiencies can be the result of Poisson fluctuations in the number of photoelectrons produced at the photocathode of the photomultiplier tube. The mean number of photoelectrons is given by the product of the number of photoelectrons per unit length, $dN_{p.e.}/dl$, with the path length of the particle in the radiator, Δl , $N_{p.e.} = dN_{p.e.}/dl \cdot \Delta l$. The Poisson inefficiency is then given by

$$1 - \epsilon = \sum_{n=0}^{N_{p.e.}^{cut}} \frac{(N_{p.e.})^n}{n!} \cdot e^{-N_{p.e.}} \quad (9)$$

where ϵ is the Cherenkov counter efficiency and $N_{p.e.}^{cut}$ is the photoelectron cut used on the phototube pulseheight. In the case of the DELCO Cherenkov counter, the ellipsoidal shape of the mirrors makes the path length vary, primarily as a function of $\cos\theta$, over the acceptance of the counter.

A convenient set of data for studying the Cherenkov response is the set of electron tracks from Bhabha events. This data set is unbiased in that the Cherenkov counter was not required in the selection of the data and the tracks cover the entire fiducial acceptance of the counter utilized for kaon identification. The electron track sample contained more than 50,000 tracks and spanned the entire run period used in the analysis. The average photoelectron yield as a function of $\cos\theta$ is shown in Figure 32. The inefficiency of the counter for pions can then be estimated from these values as a function of momentum and path length (*i.e.*, $\cos\theta$). The resulting pion efficiency versus pion momentum is shown in Figure 32 b).

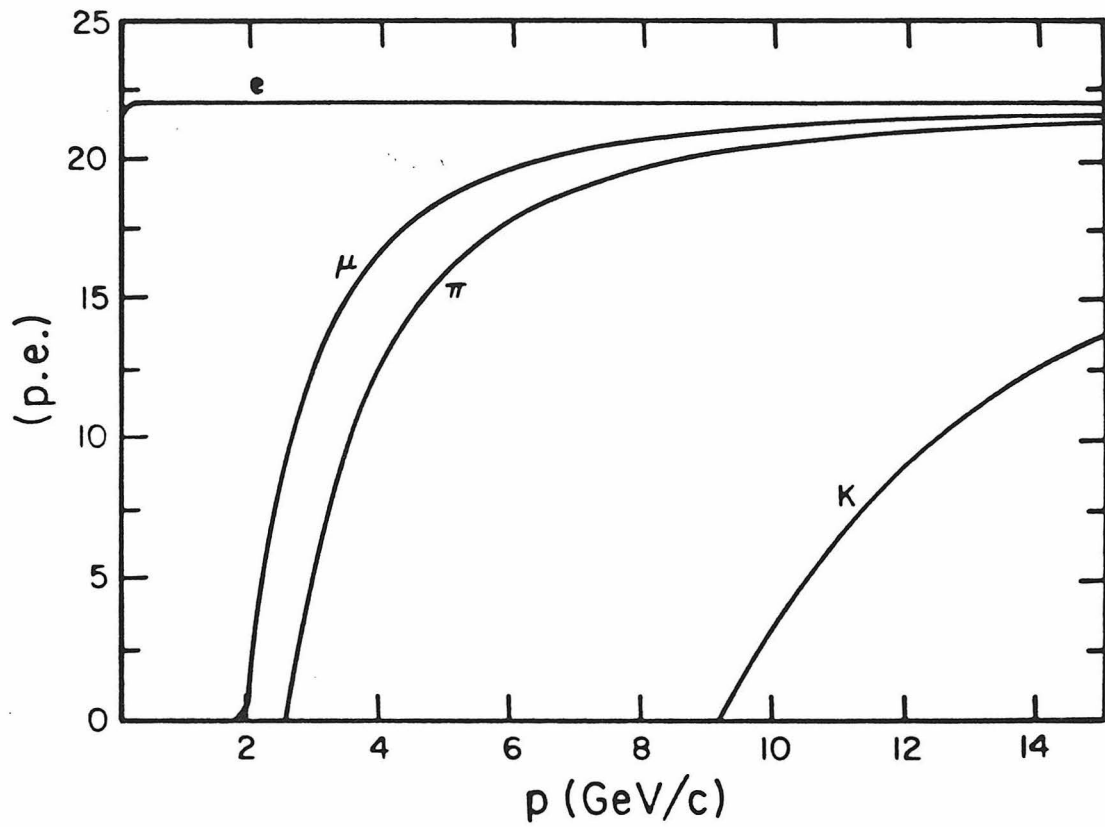


Figure 31. Cherenkov photoelectron yield vs momentum for $n_{eff} = 1.00144$. The response is shown for several particles.

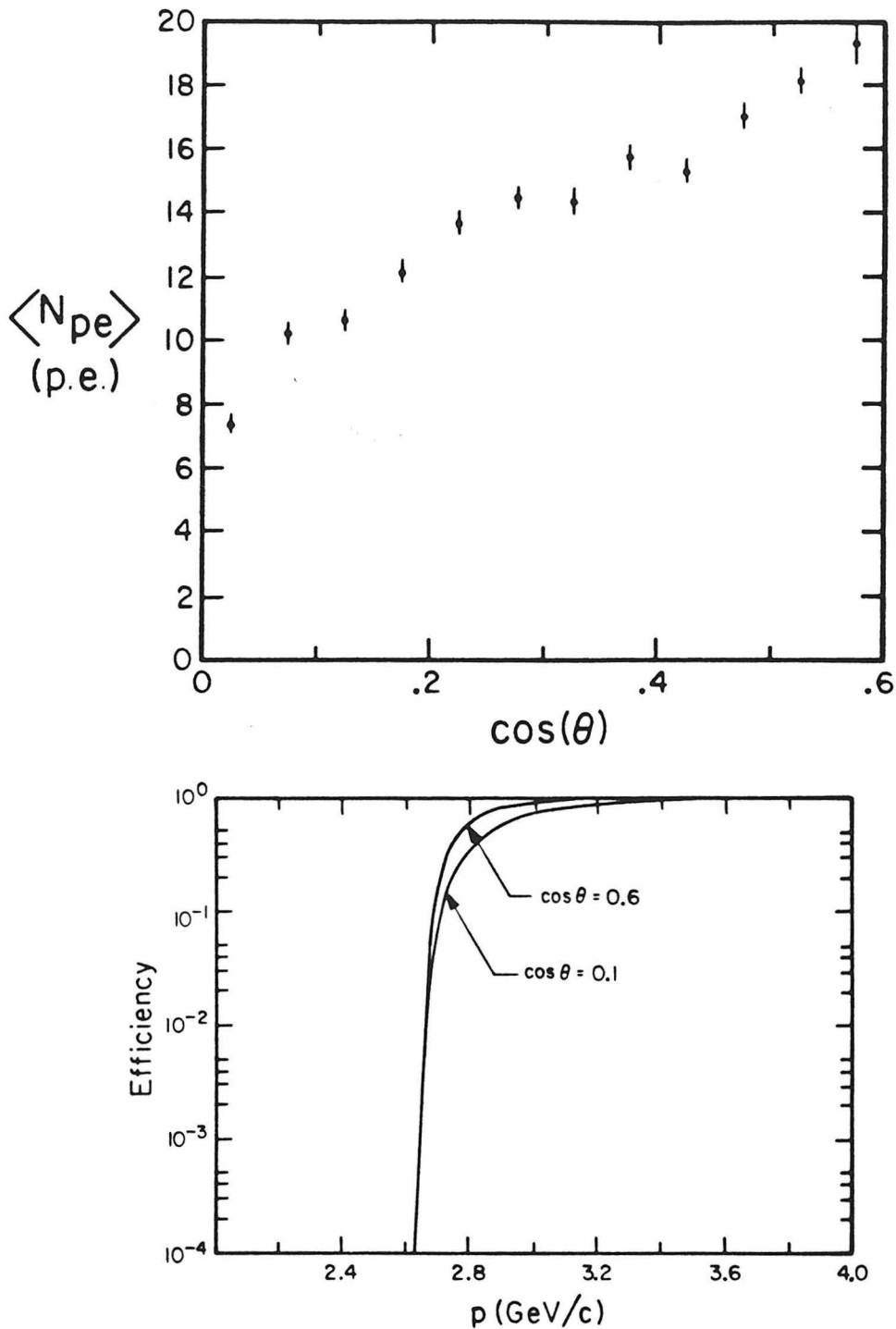


Figure 32. a) The average photoelectron yield as a function of $\cos\theta$ for electrons from the Bhabha scattering process. b) The Cherenkov pion efficiency versus pion momentum as calculated from the measured Bhabha pulseheight for $\cos\theta = 0.1$ and 0.6.

§§4.3.2 Track Quality and Momentum Resolution

A potentially serious cause of contamination from pions in the kaon is momentum mismeasurement. It is of interest therefore to determine the form of the momentum resolution function. To define a track in the spectrometer, a number of track quality cuts which are made to insure good reconstruction of the track momentum are described. Next, the effect of momentum smearing on Cherenkov pion rejection is demonstrated.

Track quality was determined by the wire composition in each of the chambers and by global properties of the track. The wire composition of tracks was broken down into groups of z (axial) wires and $u - v$ (paraxial) wires for each of the three chambers IDC, CDC, and PDC. A majority of the wires in each group was required to be present on a track in order for it to have been called a good track. In addition the total number of wires on the track was required to be greater than fourteen. Table 8 summarizes these track quality cuts. Table 9 shows the relative population distribution for each category of wire type in the IDC, CDC, and PDC. The cuts shown in Table 8 were determined by these efficiencies. The track was also required to have come within 2.5 mm of the beam axis to remove a few spuriously found tracks. Finally, the software which makes a fit of the track parameters to the wire hit positions was required to have made a successful fit completion, *i.e.*, to have converged properly on the final parameters. The efficiencies of these cuts are dependent on the particular analysis and will be discussed later.

The width of the spectrometer momentum resolution function depends upon the momentum of the particle being measured. At momenta higher than 2.5 GeV/c drift chamber measurement errors dominate because the curvature of the tracks becomes vanishingly small. At low momenta ($\leq 2.5 GeV/c$) the momentum resolution is dominated by multiple scattering effects. The resolution function at

Table 8. The track quality cuts required of kaon candidates including both wire cuts and global track cuts.

Kaon Identification Track Quality Cuts	
Wire Content Requirement:	
IDC z	≥ 1
IDC $u - v$	≥ 2
CDC z	≥ 3
CDC $u - v$	≥ 2
PDC z	≥ 2
PDC $u - v$	≥ 1
Global Track Requirement:	
Radial Vertex	$\leq 0.3\text{cm}$
Number of wires	≥ 14

high momentum may be found by looking at $\mu^+\mu^-$ events which provide a source of muons with a well-defined momentum of $14.5 \text{ GeV}/c$, neglecting radiative effects. Furthermore, there is almost no ambiguity as to the sign of the curvature as long as only events with two opposite sign muons are used. A good variable to use when studying the resolution is the inverse momentum, $\frac{1}{p}$, because the momentum smearing is nearly Gaussian in $\frac{1}{p}$. Figure 33 shows the $\mu^+\mu^-$ distribution in $\left(\frac{1}{p} - \frac{1}{14.5}\right) (\text{GeV}/c)^{-1}$. The lower half of the distribution comes from tracks where the measured momentum is greater than $14.5 \text{ GeV}/c$. This cannot be attributed to radiative effects, as might be the case on the upper half of the distribution ($p < 14.5 \text{ GeV}/c$), but can only be explained by measurement errors. The lower half of this distribution may be folded over to yield a symmetric resolution function for the apparatus. This distribution may be represented for our purposes as a

Table 9. The percentage of tracks containing the designated number of wires for each wire sector. The track sample was taken from single prong jets inside the Cherenkov fiducial volume used in kaon identification.

Wire Hit Distribution, %						
Number of	Chamber Sector					
Wires Hit	IDC		CDC		PDC	
	z	$u - v$	z	$u - v$	z	$u - v$
0	1.4	0.3	0.0	0.0	0.0	3.5
1	31.8	0.6	0.3	0.8	0.0	12.9
2	66.7	14.4	0.0	12.4	5.5	83.6
3		36.6	6.9	30.3	24.5	
4		48.2	13.3	56.5	69.7	
5			26.9			
6			52.6			

sum of two Gaussians. The first Gaussian fits the central distribution and has a width of $\sigma_1 \approx .025(GeV/c)^{-1}$ and the second, wider Gaussian with a width of $\sigma_2 \approx .05(GeV/c)^{-1}$ includes the tail of the resolution function in Fig. 33. This must then be added in quadrature with the error due to multiple scattering in the material of the spectrometer.

The multiple scattering contribution can be best calculated using the Monte Carlo simulation of the detector. However, one may accurately approximate it for DELCO as a Gaussian in $\frac{1}{p}$ with a momentum dependent width:

$$\sigma_{\frac{1}{p}}^{m.s.} = .07 \times \frac{1}{p} (GeV/c)^{-1} \quad (10)$$

where the .07 has been obtained from Monte Carlo simulation of the detector.

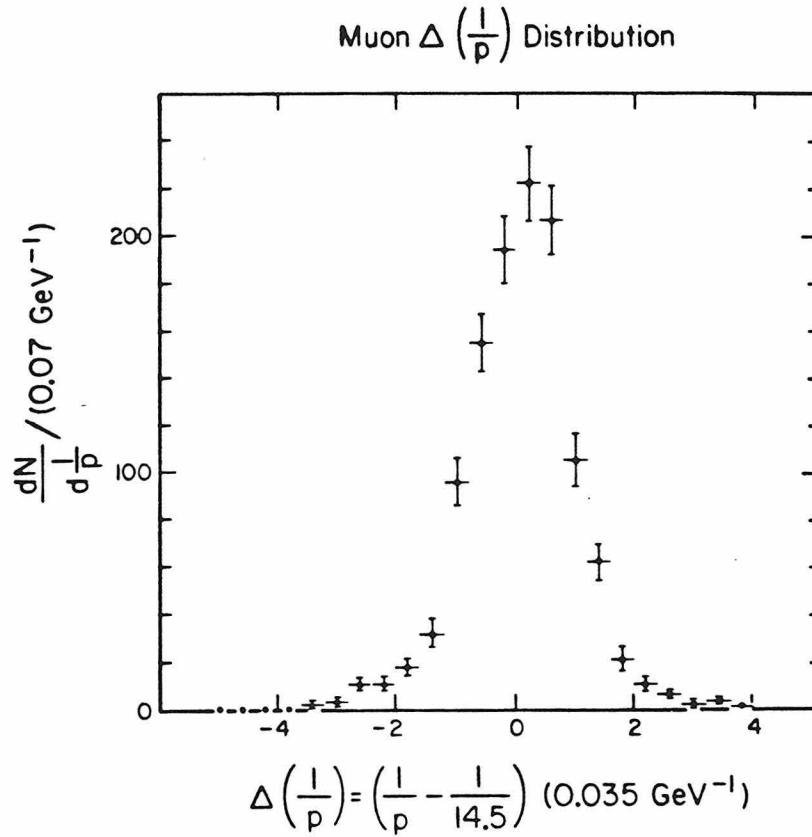


Figure 33. The distribution in $\frac{1}{p} - \frac{1}{14.5 \text{ GeV}/c}$ for muon tracks from the reaction $e^+e^- \rightarrow \mu^+\mu^-$. The lower half of the curve is exactly the resolution function of the spectrometer due to measurement error.

The complete resolution function is a combination of the contributions from measurement error and multiple scattering. Their errors add incoherently and may be combined in quadrature.

The effect of the momentum smearing on the pion threshold can be seen by calculating the pion attenuation factor versus momentum for a momentum cut of $3.5 \text{ GeV}/c$. The pion attenuation is the probability that at a pion produced at a momentum P_{true} is called a kaon and may be expressed as the product of the Cherenkov inefficiency times the probability that the pion has a measured momentum above $3.5 \text{ GeV}/c$. Figure 34 shows the pion attenuation for two values of $\cos\theta$ which are at the limits of acceptance for kaon identification. The background from any source of pions may be calculated by multiplying the appropriate momentum distribution times the attenuation for any value of $\cos\theta$ factor shown in Fig. 34. The result of this calculation suggests that, in the present case, where the expected ratio of pions to kaons is approximately 20:1, the momentum cut needed to limit the contamination to a level of a few percent is $3.5 \text{ GeV}/c$. In the following analysis we use the data in order to obtain an estimate of the true pion contamination to the kaon sample.

§4.4 Single Prong Decays

With the tools that have been developed so far, it is possible to proceed with selection of the final data sample of $\tau^+\tau^-$ events. Here, the interesting decays contain a single prong which is a charged kaon. These decays contain the modes $\tau^\pm \rightarrow K^\pm \nu_\tau$ and $\tau^\pm \rightarrow K^\pm \nu_\tau + n\pi^0$. At the outset no distinction is made between

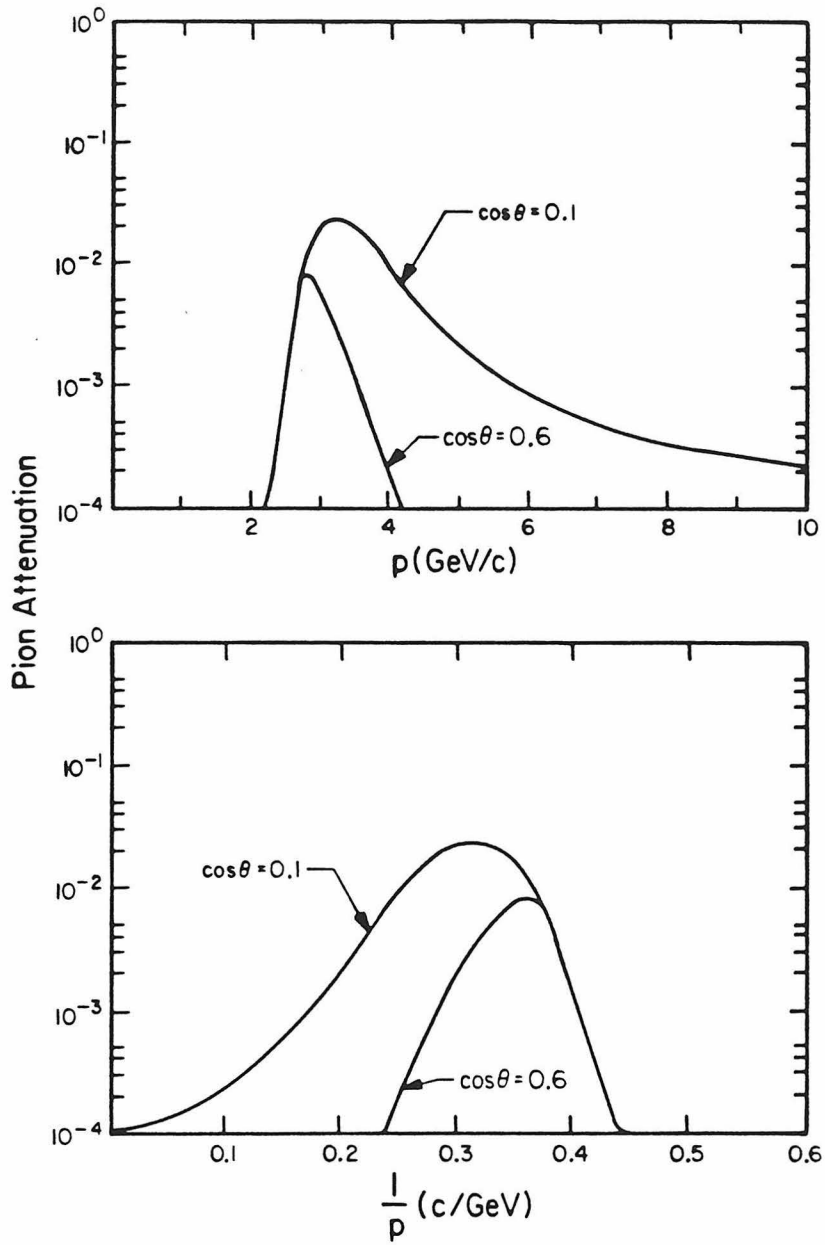


Figure 34. Pion attenuation as a function of momentum for a momentum cut of 3.5 GeV/c and a photoelectron cut of 1.5 p.e.. Two values of $\cos\theta$ are shown, 0.1 and 0.6.

these two types of decays. Only at the end will the two decay modes be separated by using the shower counters. This will allow the determination of the exclusive branching ratio for the process $\tau^\pm \rightarrow K^\pm \nu_\tau$.

§§4.4.1 *Single Prong Data Selection*

To begin with, the events have passed through the first pass filter as described in Sec. 2 of this chapter. These filters have a very high efficiency for $\tau^+\tau^-$ events. The resulting data sample numbers about 30,000 events, a large fraction of which are 2-prong radiative Bhabha events which pass the acoplanarity cut in the first pass filter. Some hadronic events, $\mu^+\mu^-$ events, and $\gamma\gamma$ events also remain in the sample.

The first step of the data selection separates the decay products of the two τ 's in the event. This is conveniently done by forming the thrust³⁰ axis of the event. This axis, which passes through the e^+e^- interaction point, closely follows the original $\tau^+\tau^-$ flight direction. The event is divided into two hemispheres by the plane which is normal to the thrust axis and which passes through the interaction point. Because of the high velocity of the τ parents, the decay products of the τ^+ will fall into one hemisphere and the decay products of the τ^- into the other. Since this is the situation almost all (98%) of the time, the charge of the individual parent τ 's may be determined by the charge of the decay products. These hemispheres are referred to as 'jets'. The τ^- jet will contain the decay products of the τ^- while the τ^+ jet will contain the decay products of the τ^+ .

At this point the kaon selection criteria is applied to all of the single prong

jets. The first part consists of placing acceptance and track quality cuts on the candidate tracks. Once this has been done the Cherenkov photo-electron cut and momentum cut select the kaons from the single prong jet sample. The efficiencies of the latter two cuts may be reliably calculated using the Monte Carlo simulator. The acceptance cuts, being largely geometric, may also be calculated using the monte carlo simulation to the needed 5% level of accuracy. To evaluate the track quality selection efficiency a sample of single prong jets, whose tracks were inside the acceptance, is taken. The momenta of the tracks are required to be between 2.5 and 10.0 GeV/c to enhance the fraction of $\tau^+\tau^-$ events ($\approx 70\%$). A similar set of simulated tracks is also taken. The track quality cuts are then performed sequentially on both the real tracks and the simulated tracks. The resulting efficiencies are compared in Table 10 on a cut by cut basis. The monte carlo gives reasonable agreement with the data. The overall efficiencies have a 5% systematic error from from uncertainty in the track quality cut.

A hadronic event can mimic a $\tau^+\tau^-$ event if some fraction of the particles in the event travel into the pole tip region of the detector. These regions are instrumented with the pole-tip and luminosity monitor shower counters which detect photons from π^0 decays as well as charged particles. These are so used to veto hadronic events of this nature. The shower counters are, however, susceptible to background noise from synchrotron radiation. A study of events of the $\mu^+\mu^-$ category shows that the probability per event of having a random latch trigger due to this source is $(5 \pm 1)\%$. In addition, $\tau^+\tau^-$ events occasionally, $(3 \pm 1)\%$ of the time, contain a photon which impacts the pole-tip shower counter module. A somewhat looser definition is therefore required to insure high efficiency for $\tau^+\tau^-$ selection. Thus, three or more out of the 36 pole-tip and 12 luminosity monitor modules or two nonadjacent modules are required to veto the event as a hadronic event. This cut proves to be greater than $(99 \pm 1)\%$ efficient for $\tau^+\tau^-$ events and rejected most of the unwanted hadronic events.

Three prong τ decays also distinguish themselves from three prong hadronic

Table 10. Track quality efficiencies found in single prong jets for both real and simulated tracks.

Single Prong Track Quality Cut Efficiencies		
Cut	Data	Monte Carlo
Radial Vertex*	0.9900	0.9993
N_{tot}^{wires}	0.9728	0.9850
IDC z	0.9923	0.9944
IDC $u - v$	0.9987	0.9986
CDC x	0.9981	1.000
CDC $u - v$	0.9953	0.9916
PDC x	0.9965	0.9916
PDC $u - v$	0.9822	0.9837
Total	0.9185 ± 0.0056	0.9550 ± 0.005
* corrected for cosmic ray contribution		

jets because in the case of the τ decay the invariant mass of the three prongs is constrained to be less than the τ mass, which is not the case in hadronic events. Most ($(98 \pm 1)\%$) of the three prong τ decays are three pions. If one uses the pion mass for each track in the decay to calculate the invariant mass of the three prongs, the distribution, in the case of the τ 's, is peaked at $1.2 GeV/c^2$ with $(99 \pm 1)\%$ below $2.1 GeV/c^2$. The same distribution for hadrons is much broader with a significant fraction above $2.1 GeV/c^2$. Consequently, the invariant mass of the three prong system is required to be less than $2.1 GeV/c^2$.

The final step is to require that the multiplicity of the jet opposite the kaon jet be less than or equal to three prongs. The number of $\tau^+\tau^-$ events which are

Table 11. Event efficiencies for each stage of the event selection. The two decay mode classes $-\tau^\pm \rightarrow K^\pm \nu_\tau$ and $\tau^\pm \rightarrow K^\pm \nu_\tau + n\pi^0$ are shown separately. The number of events which remain in the data at each stage of the selection is also shown.

Single Prong Event Selection Efficiencies				
Cut	Data (events)	Efficiency		
		$\tau^\pm \rightarrow K^\pm \nu_\tau$	$\tau^\pm \rightarrow K^\pm \nu_\tau \pi^0$	$\tau^\pm \rightarrow K^\pm \nu_\tau + 2\pi^0$
Pre-Filter	-	0.3899	0.3797	0.3845
1-Prong Jet	25,035	1.000	0.9919	0.9780
Track Acceptance	18,640	0.8333	0.8075	0.8033
Track Quality	16,983	0.9574	0.9709	0.9668
Counter Timing	14,408	0.8450	0.7751	0.7704
$p > 3.5 \text{ GeV}/c$	10,897	0.9684	0.9791	0.9726
Photoelectron	71	0.4666	0.6741	0.6514
Pole-tip Counter	64	1.000	1.000	1.000
Multiplicity	62	0.9860	0.9835	0.9892
Invariant Mass	59	0.9905	0.9963	1.000
Total	59	0.116 ± 0.01	0.148 ± 0.01	0.141 ± 0.01

expected to be above three prongs is roughly equal to the number of hadronic events. This selection criteria will be discussed further in the next section, where the contribution of hadronic events to the data sample is measured.

There are two types of decays for which efficiencies are required: $\tau^\pm \rightarrow K^\pm \nu_\tau + n\pi^0$ and $\tau^\pm \rightarrow K^\pm \nu_\tau$ where $n=1$, or 2 . These efficiencies, along with the number of observed events at each point, are shown in Table 11.

The data yielded by this event selection procedure may be compared with what is expected from the $e^+e^- \rightarrow \tau^+\tau^-$ process. There are several distributions which distinguish between $\tau^+\tau^-$ events and other processes. In Figure 35, Figure 36, and Figure 37 compare the data and theoretical predictions in several kinematic distributions. In all cases the data are in good agreement with the prediction.

§§4.4.2 Backgrounds

At this point the final data set is at hand. It remains to estimate the level of background in the data sample. There are two types of backgrounds which need to be considered. The first is sources of charged kaons other than $\tau^+\tau^-$ events. The most serious of these is hadronic events from the process $e^+e^- \rightarrow q\bar{q}$ but $e^+e^- \rightarrow e^+e^-q\bar{q}$ is considered also. The second background comes from electrons and pions being identified as kaons. These events are from Bhabha events and $\tau^+\tau^-$ events, respectively.

The backgrounds due to $e^+e^- \rightarrow e^+e^-q\bar{q}$ events have been estimated by simulating the reaction in the detector and then passing the events through the filter described above. Two types of event generators were used, the first used the born approximation to the reaction $\gamma\gamma \rightarrow K^+K^-$ and the second a $\gamma\gamma \rightarrow q\bar{q}$ generator which subsequently fragmented the quarks using the LUND fragmentation scheme. Both of these predict negligible backgrounds of less than 0.05 ± 0.03 events in the data sample from 2γ sources. In addition, there is an empirical limit of 3 events in the data sample due to the fact that there are no K^+K^- events in the data sample.

The most serious contamination to the sample is from hadronic events. A

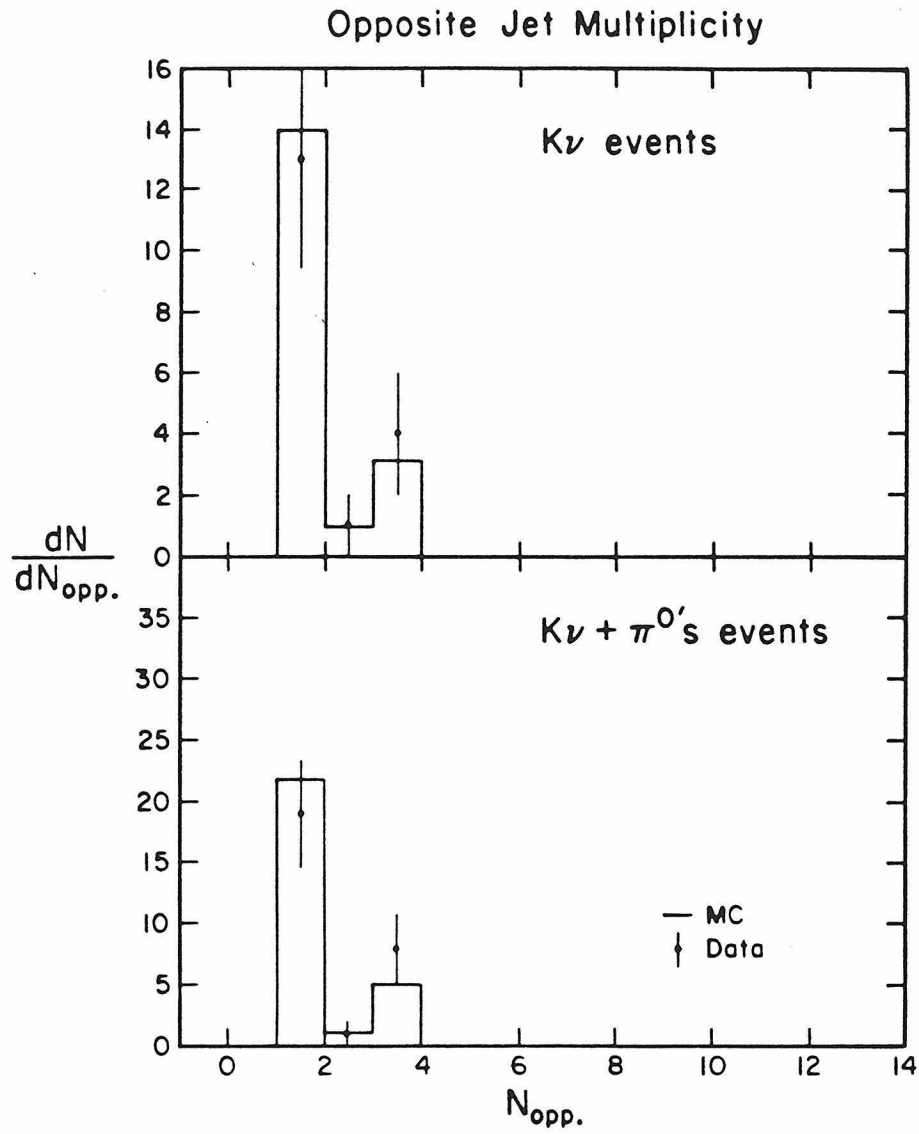


Figure 35. The opposite jet multiplicity in the single prong kaon events. The distributions are in agreement with that which is expected from $\tau^+\tau^-$ events.

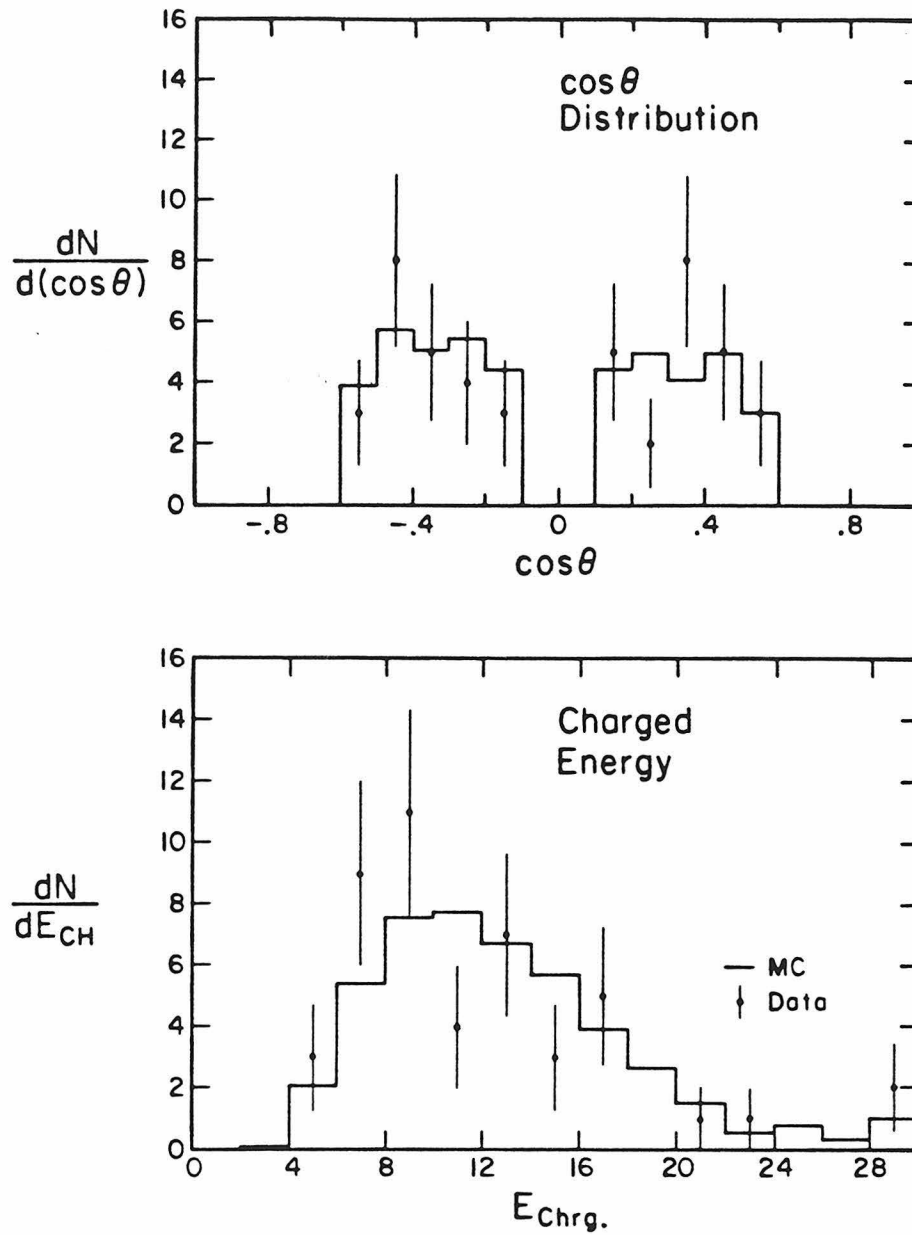


Figure 36. The $\cos \theta$ and charged energy distributions for single prong kaon events. The monte carlo prediction for the reaction $e^+e^- \rightarrow \tau^+\tau^-$ is shown by the solid line.

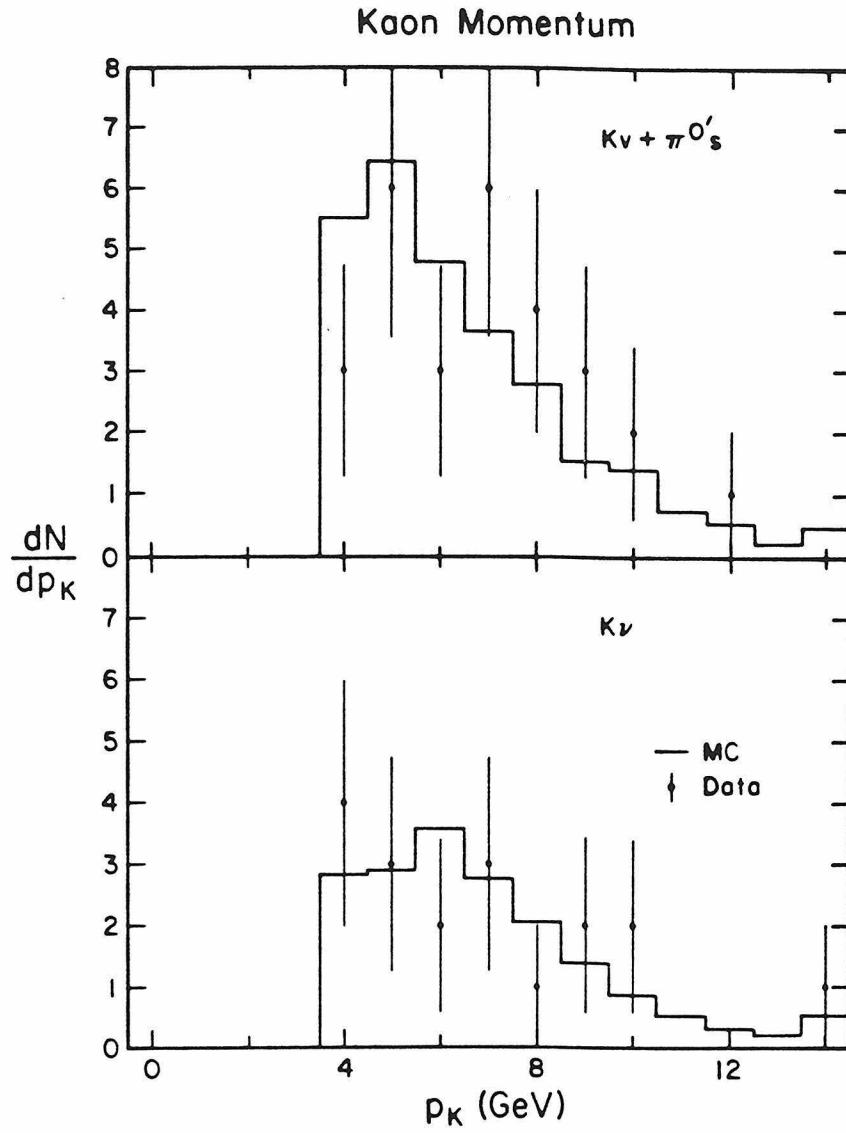


Figure 37. The momentum distribution for the identified charged kaons for the $\tau^\pm \rightarrow K^\pm \nu_\tau$ and $\tau^\pm \rightarrow K^\pm \nu_\tau + n\pi^0$ category events.

Careful consideration of the background due to this source is therefore necessary. The LUND Monte Carlo can be used to predict the contribution of hadronic events to the sample. However, because a measurable amount is predicted, a more careful analysis is required. As mentioned previously, the multiplicity distribution of hadron jets differs greatly from that of τ decays. This fact can be used to estimate the hadronic contribution to the sample.

By removing the multiplicity cut of less than three tracks in the jet opposite the kaon, the opposite jet multiplicity, N_{opp} , in the data can be compared to that which is predicted for $\tau^+\tau^-$ events and that which is predicted for hadronic events. This distribution is shown in Fig. 38. Half of the hadronic events are expected to be above $N_{opp}=3$. By normalizing the predicted hadronic distribution to the number of observed events in the data above $N_{opp} > 3$, an extrapolation can be made into the signal region of $N_{opp} = 1, 2$, and 3. The number of hadronic events predicted to be in the sample is 3.2 ± 2.3 events.

The next source of background events is from particle misidentification. The level of background from Bhabha events which pass the kaon due to Cherenkov inefficiency is, from the measured inefficiency of 0.2×10^{-4} , 0.5 events. In the data sample there is one event which has a 50% chance of being a Bhabha event with an inefficient Cherenkov counter and a 50% chance of being a $\tau^+\tau^-$ event. The expected number of events due to Bhabha's is therefore 0.5 ± 0.5 events.

The remaining source of background events is from τ decays where a pion in the final state is misidentified as a kaon just above pion threshold. This problem was discussed in the previous section; however, a direct estimate of the background is needed for this data set. In order to make an accurate estimation of the background from pion misidentification, all single prong jets which pass all cuts -acceptance, track quality, Cherenkov photo-electron, multiplicity, shower counter latches, and invariant mass cuts- except the momentum cut are selected. These events are predominantly $\tau^+\tau^-$ events and have a single prong jet whose Cherenkov cell does

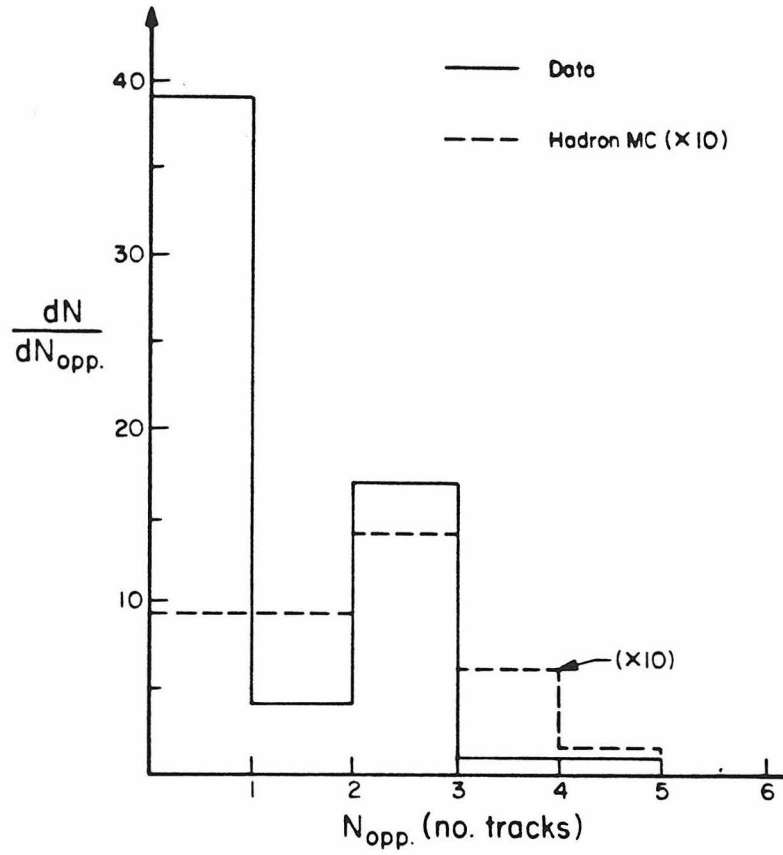


Figure 38. The multiplicity distribution of the jet opposite the kaon jet after all cuts have been placed on the data except the multiplicity cut. The solid curve is the data and the dashed curve is the prediction for hadronic events (LUND).

not have a positive signal. The distribution of the tracks in these jets in $\frac{1}{p}$, where p is the track momentum, shows the behavior at Cherenkov threshold (see Fig. 39). An extrapolation of the Monte Carlo prediction of the pion threshold fall off is used to predict the number of background events in the data sample to be 0.5 ± 0.5 events.

§§4.4.3 Single Prong Branching Ratios

The branching ratios of interest here are the total inclusive branching ratio for the decay $\tau^\pm \rightarrow K^\pm \nu_\tau + n\pi^0$ and the branching ratio for the decay $\tau^\pm \rightarrow K^\pm \nu_\tau$ which is a subset of the former decay. In order to separate the $\tau^\pm \rightarrow K^\pm \nu_\tau$ events from the rest it is necessary to employ the photon detection capability of the barrel shower counter system. This divides the sample into two classes of decays, those decays with associated shower energy and those without associated shower energy. From these two classes of events one may unfold the number of $\tau^\pm \rightarrow K^\pm \nu_\tau$ events. Once this has been accomplished the known efficiencies and the known luminosities lead directly to the desired branching ratios, $\tau^\pm \rightarrow K^\pm \nu_\tau + n\pi^0$ and $\tau^\pm \rightarrow K^\pm \nu_\tau$.

The first task is to divide the events into two classes using the shower counters. This is achieved by summing the pulse height response in the barrel shower counters within a 45° azimuthal angle of the kaon track. If this pulse height sum is above a level equivalent to the response of 3 minimum ionizing particle responses (*i.e.*, 3 *mips*), signifying the presence of a photon shower, then it falls into the E_0 class. If the pulse height sum falls below 3 *mips*, signifying no photon shower, then it falls into the $\overline{E_0}$ class. It remains to be determined how much of each type of decay, those with π^0 's and those without, remain in each class. In order to see this,

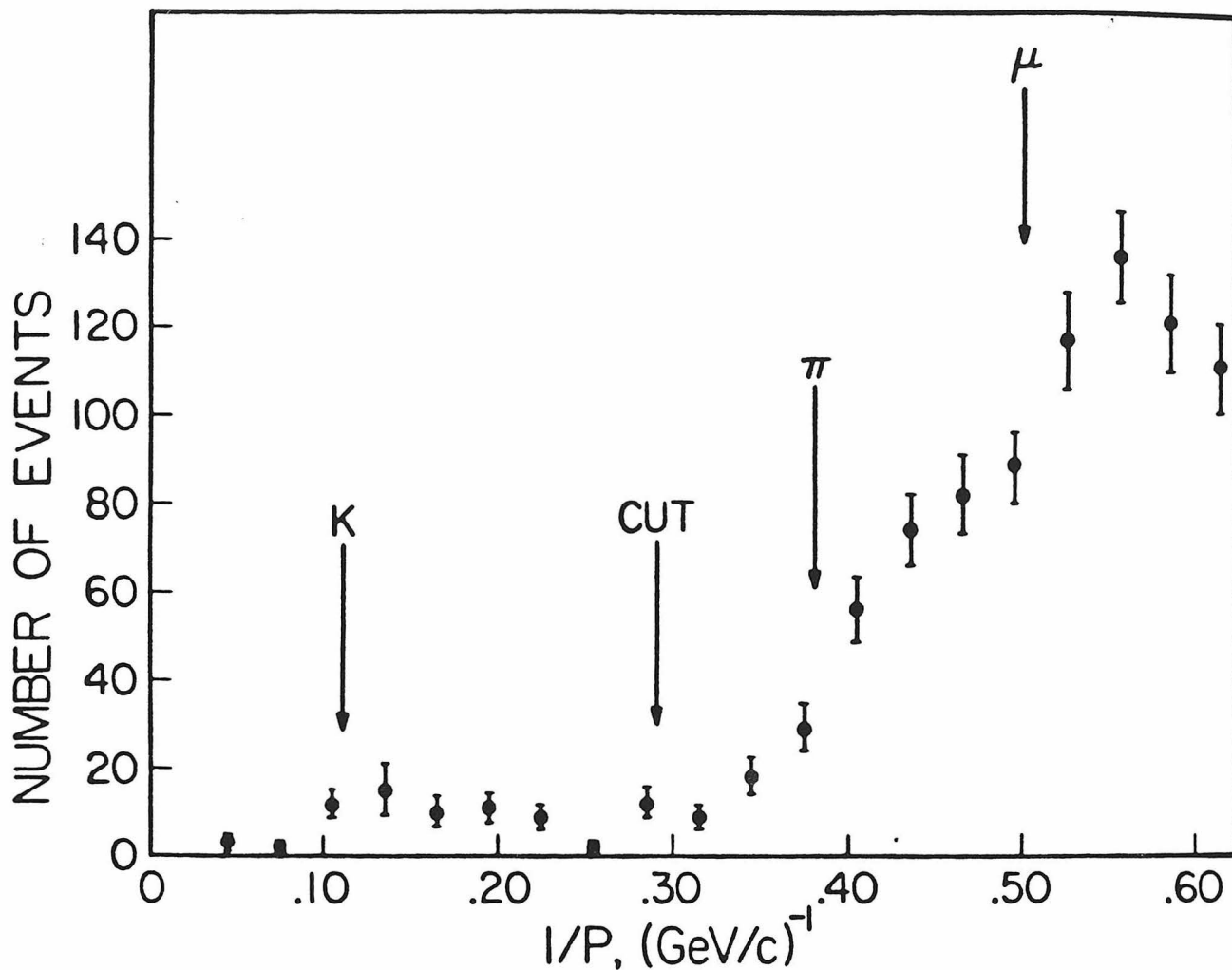


Figure 39. The $\frac{1}{p}$ distribution of all single prong jets passing all event cuts, acceptance cuts, track quality cuts, and photo-electron cuts. The kaon, pion, muon thresholds are visible at $\frac{1}{p} = 0.11, 0.38, \text{ and } 0.51$, respectively. The prediction for $\tau^\pm \rightarrow K^\pm \nu_\tau + n\pi^0$ (dashed line) and the prediction for general $\tau^+\tau^-$ decays not containing charged kaons (dotted line) are shown with the data.

the distribution of shower pulseheight responses is plotted for muon tracks from $\mu^+\mu^-$ events (see Fig. 40). The pulse height distributions of kaons differs from that of muons due to nuclear interactions in the counter material. This is related to the total nuclear cross section times the probability that a π^0 is produced in the interaction. The distribution of pulse heights for 1-2 GeV/c pions in the shower counters in Fig. 40 shows a 12% inefficiency for a 3 MIP cut. Kaons will have a similar inefficiency with the same cut. This is because the nuclear cross section is nearly the same in the energy range of interest, 3-10 GeV/c^2 . This means that $(11.4 \pm 5.2)\%$ of the $\tau^\pm \rightarrow K^\pm \nu_\tau$ decays are put into the E_0 class and $(88.6 \pm 5.2)\%$ are put into the $\overline{E_0}$ class.

The photons from the π^0 's in the decays $\tau^\pm \rightarrow K^\pm \nu_\tau + n\pi^0$ miss the shower counters $(17.1 \pm 0.3)\%$ of the time. Thus $(82.9 \pm 0.3)\%$ of the decays $\tau^\pm \rightarrow K^\pm \nu_\tau + n\pi^0$ are put into the E_0 class. The rest fall into the $\overline{E_0}$ class.

After a background subtraction of $(5.4 \pm 3.8)\%$ events from the E_0 and $\overline{E_0}$ classes there is the following number of events in each class:

$$\begin{aligned} N_{E_0} &= (34.05 \pm 1.70) \\ N_{\overline{E_0}} &= (21.75 \pm 1.09) \quad . \end{aligned} \tag{11}$$

In order to unfold the number of $\tau^\pm \rightarrow K^\pm \nu_\tau$ decays, N_K , and the number of $\tau^\pm \rightarrow K^\pm \nu_\tau + n\pi^0$ decays, $N_{K+\pi^0's}$, from N_{E_0} and $N_{\overline{E_0}}$ it is necessary to invert the equations :

$$\begin{aligned} N_{E_0} &= f_K^{E_0} \cdot N_K + f_{K+\pi^0's}^{E_0} \cdot N_{K+\pi^0's} \\ N_{\overline{E_0}} &= f_K^{\overline{E_0}} \cdot N_K + f_{K+\pi^0's}^{\overline{E_0}} \cdot N_{K+\pi^0's} \end{aligned} \tag{12}$$

where: $f_K^{\overline{E_0}}$ ($= 0.886 \pm 0.052$) and $f_K^{E_0}$ ($= 0.114 \pm 0.052$) are the fraction of $\tau^\pm \rightarrow K^\pm \nu_\tau$ events which fall into the $\overline{E_0}$ and E_0 class, respectively, and $f_{K+\pi^0's}^{\overline{E_0}}$ ($= 0.171 \pm 0.030$) and $f_{K+\pi^0's}^{E_0}$ ($= 0.829 \pm 0.030$) are the fraction of $\tau^\pm \rightarrow K^\pm \nu_\tau + n\pi^0$

Shower Counter Pulse Height

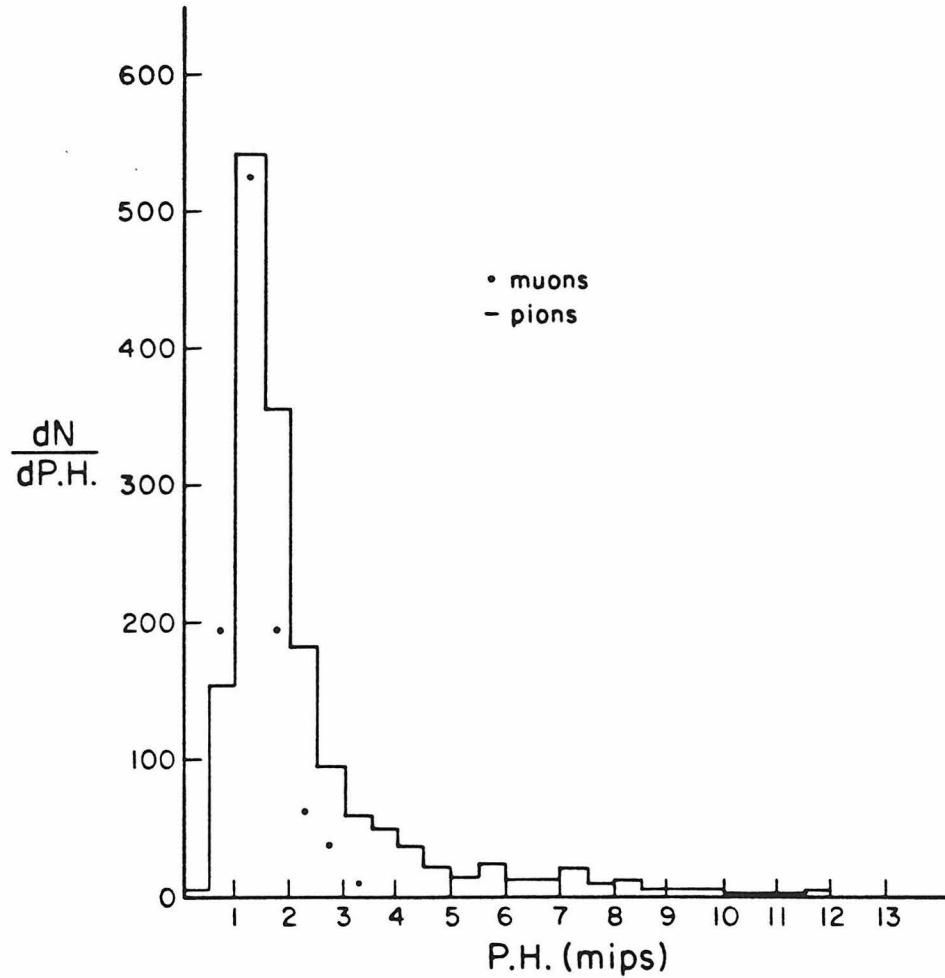


Figure 40. Shower counter pulse height distribution for muons selected from $e^+e^- \rightarrow \mu^+\mu^-$ events. The response from 1-2 GeV/c pions is also shown by the solid line. The value chosen for the separation of $\tau^\pm \rightarrow K^\pm \nu_\tau$ events is 3 MIPS. At this value the efficiency for muons is 99% while for pions it is 88%. Kaons have nearly the same nuclear cross section as pions in the energy range of interest, 3-10 GeV/c^2 .

decays which fall into the \overline{E}_0 and E_0 classes, respectively. The result is that:

$$\begin{aligned} N_{K+\pi^0's} &= (38.73 \pm 1.94) \\ N_K &= (17.07 \pm 0.85) \end{aligned} \quad (13)$$

The next step is to relate the branching ratios to the number of observed events. The branching ratio is given by the formula:

$$BR = \frac{N_{observed}}{2 \cdot L \cdot (\sigma \cdot \epsilon)} \quad (14)$$

where: the 2 in the denominator results from there being two τ 's in each event, L ($= 95 \pm 5$) pb^{-1} is the luminosity for the event sample used, and $(\sigma \cdot \epsilon)$ is the product of the generated cross section ($= 0.136pb$) times the efficiency of the mode being considered. When calculating the efficiency for the decays $\tau^\pm \rightarrow K^\pm \nu_\tau + n\pi^0$ it is necessary to use the measured branching ratios of the $\tau^\pm \rightarrow K^{*\pm}(890)\nu_\tau$ and $\tau^\pm \rightarrow Q^\pm(1300)\nu_\tau$ decay modes^{31,32} to obtain the relative $K + 1\pi^0$ to $K + 2\pi^0$'s ratio in the $\tau^\pm \rightarrow K^\pm \nu_\tau + n\pi^0$ channel. The answer is not sensitive to this ratio, however.

The efficiencies are calculated using the event monte carlo simulator. They are: (0.116 ± 0.01) for the decay mode $\tau^\pm \rightarrow K^\pm \nu_\tau$ and (0.147 ± 0.01) for the decay mode $\tau^\pm \rightarrow K^\pm \nu_\tau + n\pi^0$. By putting into Eqn. 14 the results in Eqn. 13 the branching ratios are then:

$$\begin{aligned} BR(\tau^\pm \rightarrow K^\pm \nu_\tau + n\pi^0, n > 0) &= (1.02 \pm 0.16 \pm 0.08)\% \\ BR(\tau^\pm \rightarrow K^\pm \nu_\tau) &= (0.57 \pm 0.14 \pm 0.04)\% \end{aligned} \quad (15)$$

The errors are dominated by the statistical error introduced by the number of events in the sample. The systematic errors induced by the background subtraction/unfolding procedure are 5%. An additional 3% systematic uncertainty comes from acceptance calculations. Finally, there is a 5% uncertainty in the luminosity leaving the total systematic uncertainty at 8%.

§4.5 Multi Prong Decays

The study of single prong decays in the previous section lead to methods for identifying charged kaons and determining the associated backgrounds in the final data sample. These methods may be extended to the 3-prong decays of the τ lepton which is the subject of this section. Many of the event selection criteria used in the single prong selection can be carried over directly to the multi-prong case. The rest require slight modifications which will be discussed presently.

The objective of this analysis is two-fold. As in the previous section the branching ratios are measured. In the present case the decays of interest are the Cabibbo-suppressed decay $\tau^\pm \rightarrow K^\pm \pi^+ \pi^- \nu_\tau (\pi^0)$ and the Cabibbo-favored decay $\tau^\pm \rightarrow K^+ K^- \pi^\pm \nu_\tau$ which may be separated from each other by virtue of the relationship between the charges of the parent τ and the daughter kaon. The second goal of this section is to obtain an upper bound on the τ neutrino mass by using the invariant mass of the $KK\pi$ system from the decay $\tau^\pm \rightarrow K^+ K^- \pi^\pm \nu_\tau$. This requires the identification of both kaons in the decay in order to correctly identify the particles for the invariant mass calculation of the $KK\pi$ system.

§§4.5.1 Multi-Prong Data Selection

The event selection proceeds in much the same way as the in the single prong analysis. The first pass cuts as described in Section 2 of this chapter produce the data set which is used as a starting point in this analysis. As in the previous

section the efficiencies for these cuts may be calculated using the Monte Carlo event simulator.

The events are divided into two hemispheres (jets) and then classified according to the number of tracks from charged particles found in each hemisphere (jet). Events from the reaction $e^+e^- \rightarrow \tau^+\tau^-$ will fall into the 1-3 category (topology); *i.e.* , one jet contains one track and the other contains three tracks, and, events will fall into the 3-3 category (topology); *i.e.* , 3 tracks in each jets. Since the backgrounds from hadronic events are large in the 3-3 topology only the 1-3 events are used in this analysis. This gives a topological acceptance of 86% for all 3-prong decays of the τ .

In order to further reduce the background from hadronic events in the 1-3 topology the invariant mass of the 3-prong decay is required to be consistent with being less than the τ mass (since there is a neutrino in the final state the mass is always less than the τ mass), *i.e.* , less than $2.1 \text{ GeV}/c^2$. The particles are all assumed to be pions in the calculation of the invariant mass. This is a conservative estimate of the true invariant mass since in the decays of interest, $\tau^\pm \rightarrow K^+K^-\pi^\pm\nu_\tau$ and $\tau^\pm \rightarrow K^\pm\pi^+\pi^-\nu_\tau(\pi^0)$, there is at least one kaon present in the final state. This requirement is $(99.0 \pm 0.5)\%$ efficient for the decays $\tau^\pm \rightarrow K^+K^-\pi^\pm\nu_\tau$ and $\tau^\pm \rightarrow K^\pm\pi^+\pi^-\nu_\tau(\pi^0)$.

The final step in the event selection is the identification of a charged kaon in the 3-prong decay. The kaon identification criteria involve three classes of cuts: track acceptance, track quality, and the Cherenkov photo-electron and track momentum cuts. These have some modifications specific to the multi-prong decays which will be discussed here.

The acceptance cuts remain the same as in the single prong case. A kaon candidate track is required to be in the $\cos\theta$ range $0.1 \leq |\cos\theta| \leq 0.59$ and is also required to impact a barrel shower counter inside the fiducial volume of the barrel shower counter system . These acceptance requirements are the same as those used to select the Bhabha track sample which were used to study the efficiency of the

Cherenkov counter.

The track quality selection requirements are essentially the same as in the last section. It is necessary to make them more stringent with regard to the outer chamber wire requirements. It is also necessary to introduce a way to assure a good spacial separation of the kaon candidate from other tracks to minimize tracking confusion.

The outer chamber wire requirements change because the addition of two more tracks in the event causes confusion in the track reconstruction. This confusion is eliminated by requiring both U-V wires in the outer chambers to be associated with the track. The efficiency calculation for this and all other track quality cuts is checked by comparing a known set of track efficiencies found in $\tau^\pm \rightarrow 3\pi^\pm(\pi^0)\nu_\tau$ decays to the efficiencies found in a similar set of Monte Carlo generated tracks. These efficiencies are shown in Table 12 and show good agreement ($\pm 5\%$) between the Monte Carlo and the data.

In order to isolate the kaon track from other tracks in the decay the difference in the ϕ angles of the kaon track with the other two tracks in the decay, when multiplied by the charge (± 1) of the other track (Q_{track}), is required to be in the range:

$$-80mr \leq Q_{track} \cdot (\phi_{track} - \phi_K) \leq 50mr \quad .$$

The reason for the apparent asymmetry in the cut is due to the track's curvature being away or toward the kaon candidate track. The Monte Carlo efficiency is in good agreement with that found in the data as seen in Table 12.

The final kaon identification requirements are the photoelectron cut and momentum cut as discussed in Section 3 of this chapter. These requirements remain the same as in the case of the single prong analysis. The $\frac{1}{p}$ distribution of tracks with no Cherenkov pulse height from events which pass all cuts is shown in Fig. 41. Extrapolating the pion fall off into the signal region gives a pion background of (0.7 ± 0.4) . With a momentum cut of $3.5 GeV/c$ there are 9 events which pass

Table 12. A comparison of the efficiencies for the track quality cuts used in the multi-prong event selection. The data are compared to the Monte Carlo prediction in the case of $\tau^\pm \rightarrow 3\pi^\pm(\pi^0)\nu_\tau$.

Multi-prong Track Quality Cut Efficiencies		
Cut	MonteCarlo	Data
Radial Vertex	$(100.0 \pm 0.1)\%$	$(99.8 \pm 0.2)\%$
Total Wire	$(99.7 \pm 0.1)\%$	$(97.7 \pm 0.5)\%$
IDC z	$(99.1 \pm 0.1)\%$	$(97.3 \pm 0.7)\%$
IDC $u - v$	$(99.9 \pm 0.1)\%$	$(98.3 \pm 0.6)\%$
CDC z	$(100.0 \pm 0.1)\%$	$(99.4 \pm 0.4)\%$
CDC $u - v$	$(99.5 \pm 0.5)\%$	$(98.8 \pm 0.5)\%$
PDC z	$(99.0 \pm 0.3)\%$	$(99.4 \pm 0.4)\%$
PDC $u - v$	$(92.7 \pm 0.8)\%$	$(93.0 \pm 1.2)\%$
Total	$(89.2 \pm 1.5)\%$	$(84.4 \pm 0.4)\%$
$\Delta\phi$	$(78.5 \pm 1.5)\%$	$(82.0 \pm 1.8)\%$

all selection criteria. A summary of the efficiencies for each of the cuts and a summary of the amount of data at each stage are shown in Table 13. In Table 14 the efficiencies for the entire selection procedure are shown.

The amount of hadronic background in the sample may be determined from the multiplicity distribution in the data by comparing it with the prediction for hadronic events. In the case of the multi-prong decay, it is of interest to find the background in the 1-3 topology channel. To accomplish this the 1-5, 3-3, and 3-5, topology channels are employed by comparing the data to the hadron Monte Carlo predictions. These topologies are dominated by hadronic events and give a

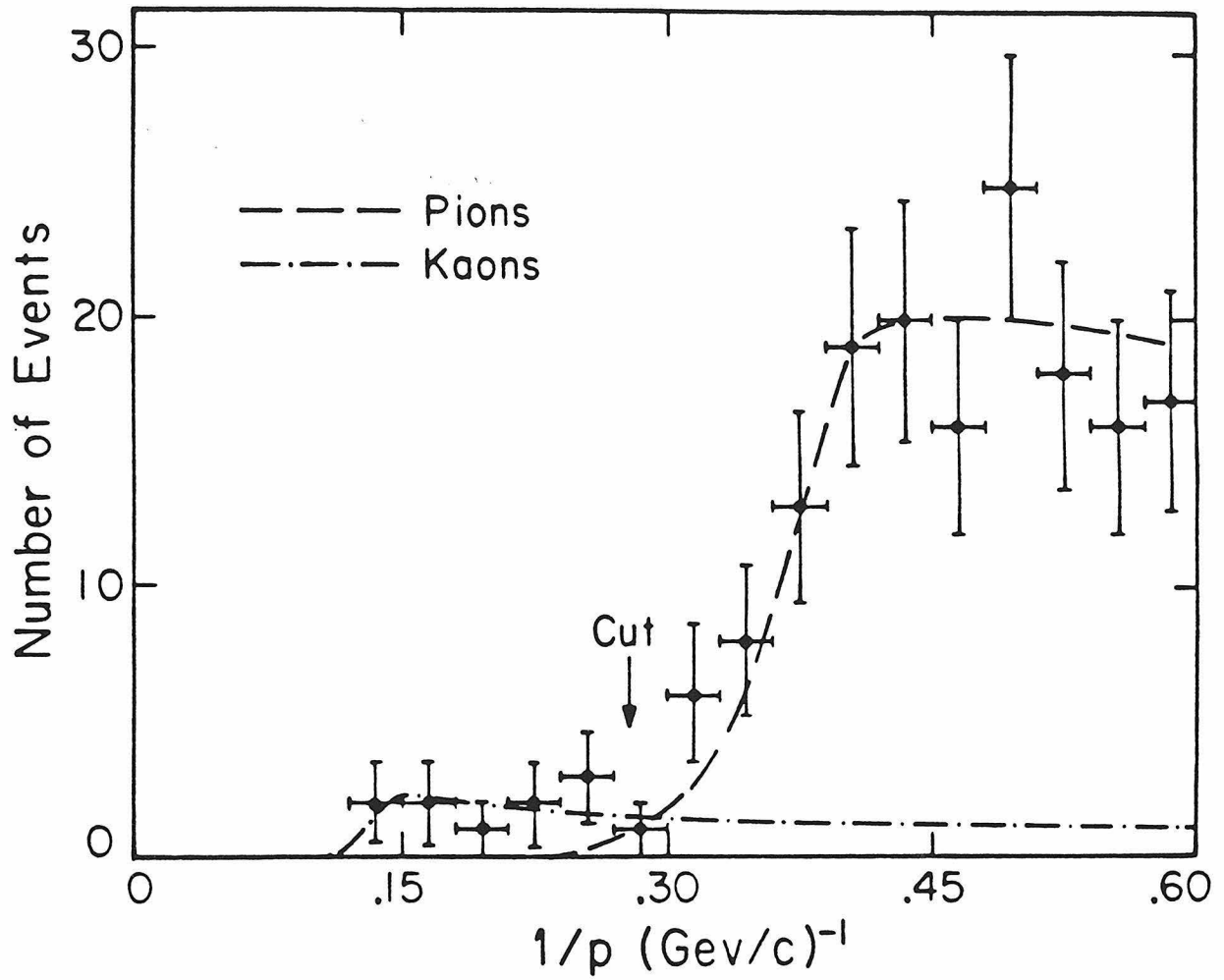


Figure 41. The $\frac{1}{p}$ distribution of tracks which pass all cuts except the momentum cut (*i.e.*, no Cherenkov light). The dashed line is the prediction for kaons in 3-prong τ decays and the dotted line is the prediction for $\tau^\pm \rightarrow 3\pi^\pm(\pi^0)\nu_\tau$ decays. The background from pion misidentification is (0.7 ± 0.4) events.

Table 13. The efficiencies for the kaon identification cuts used in the multi-prong analysis. The efficiencies are shown for two decay channels, $\tau^\pm \rightarrow K^+K^-\pi^\pm\nu_\tau$ and $\tau^\pm \rightarrow K^\pm\pi^+\pi^-\nu_\tau(\pi^0)$.

Multi-prong Kaon Identification Efficiencies			
Cut	Final State (MC)		Data
	$\tau^\pm \rightarrow K^\pm\pi^+\pi^-\nu_\tau(\pi^0)$	$\tau^\pm \rightarrow K^+K^-\pi^\pm\nu_\tau$	N_{ev}
Multi-prong jet	$(81.5 \pm 0.8)\%$	$(81.1 \pm 0.8)\%$	6077
Sub. Jet Momentum	$(99.9 \pm 0.1)\%$	$(99.9 \pm 0.1)\%$	4420
Track Acceptance	$(90.7 \pm 0.7)\%$	$(89.3 \pm 1.0)\%$	4079
Track Quality	$(81.9 \pm 0.7)\%$	$(77.9 \pm 1.0)\%$	2976
Momentum	$(60.3 \pm 1.1)\%$	$(65.5 \pm 1.7)\%$	1172
Photo Electron	$(35.9 \pm 1.4)\%$	$(65.3 \pm 2.2)\%$	115
Pole-Tip Counter	$(100. \pm 0.1)\%$	$(100. \pm 0.1)\%$	90
Topology (1-3)	$(78.2 \pm 1.4)\%$	$(81.2 \pm 2.9)\%$	14
Invariant Mass	$(99.6 \pm 0.6)\%$	$(97.3 \pm 1.2)\%$	10
Total	$(10.2 \pm 0.5)\%$	$(19.1 \pm 0.9)\%$	9

normalization for the hadron Monte Carlo prediction. This procedure is the same as that used in in the single prong case of the last section. The normalized prediction for the hadronic background in the 1-3 channel is then (0.8 ± 0.4) events as shown in Table 15. A summary of the data and associated backgrounds is shown in Table 16.

Table 14. The efficiencies for the event selection cuts used in the multi-prong analysis. The efficiencies are shown for two decay channels, $\tau^\pm \rightarrow K^+K^-\pi^\pm\nu_\tau$ and $\tau^\pm \rightarrow K^\pm\pi^+\pi^-\nu_\tau(\pi^0)$.

Multi-Prong Filter Efficiency Summary		
Filter	$\tau^\pm \rightarrow K^+K^-\pi^\pm\nu_\tau$	$\tau^\pm \rightarrow K^\pm\pi^+\pi^-\nu_\tau(\pi^0)$
PASS1	$(56.0 \pm 1.0)\%$	$(60.3 \pm 1.0)\%$
Trigger	$(80.1 \pm 1.5)\%$	$(79.9 \pm 1.4)\%$
Classification	$(87.6 \pm 1.8)\%$	$(85.0 \pm 1.8)\%$
1 - K	$(19.1 \pm 0.7)\%$	$(10.2 \pm 0.5)\%$
total	$(7.5 \pm 0.3)\%$	$(4.2 \pm 0.2)\%$

Table 15. The contribution of hadrons to the multi-prong τ decays containing charged kaons.

Hadronic Backgrounds			
Source	Topology		
	(1-3)	(1-4) , (1-5)	(3-3) , (3-5)
Data	9	1	18
Tau MC	9.0	0.0	2.3
LUND MC	0.8 ± 0.4	1.3	15.4

§§4.5.2 Multi Prong Branching Ratios

The multi-prong decays of the τ which contain charged kaons are expected to come from two sources, the Cabibbo-favored decay, $\tau^\pm \rightarrow K^+K^-\pi^\pm\nu_\tau$, and the

Table 16. A summary of the data and backgrounds from the multi-prong τ decays containing charged kaons. The charge correlation between the parent τ and the daughter kaon is also shown.

Multiprong Data Summary					
Number of	Background		Charge Correlation Category		
Events	π 's	Hadrons	$Q_K = Q_\tau$	$Q_K = -Q_\tau$	2K
9	(0.9 ± 0.3)	(0.8 ± 0.4)	6	2	1

Cabibbo-suppressed decay, $\tau^\pm \rightarrow K^\pm \pi^+ \pi^- \nu_\tau(\pi^0)$. In the data sample selected so far there are 9 decays. In six of these decays, the charge of the kaon is the same as the charge of the parent τ , whose charge is determined by that of the jet. These decays can come from either the $\tau^\pm \rightarrow K^+ K^- \pi^\pm \nu_\tau$ decay or the $\tau^\pm \rightarrow K^\pm \pi^+ \pi^- \nu_\tau(\pi^0)$ decay because, in either case, a kaon of that charge exists in the final state. Two of the decays have a kaon whose charge is opposite that of the parent τ . These can only come from the decay $\tau^\pm \rightarrow K^+ K^- \pi^\pm \nu_\tau$. The event with two kaons in the decay can also only come from the $\tau^\pm \rightarrow K^+ K^- \pi^\pm \nu_\tau$ decay.

The efficiencies for each of the modes to fall into the three charge combinations ($Q_\tau = Q_K$, $Q_\tau = -Q_K$, and $Q_\tau = \pm Q_K(2 \text{ kaons})$) is shown in Table 17.

In order to determine the branching ratios for the decay modes $\tau^\pm \rightarrow K^+ K^- \pi^\pm \nu_\tau$ and $\tau^\pm \rightarrow K^\pm \pi^+ \pi^- \nu_\tau(\pi^0)$, a Poisson likelihood fit is performed to the number of events in the three charge categories. The fit uses the branching ratios, $BR_{KK\pi}$ and $BR_{K\pi\pi}$, as free parameters. The number of observed opposite sign events ($Q_\tau = -Q_K$), N_{1K}^{os} , the number of observed same sign events ($Q_\tau = Q_K$), N_{1K}^{ss} , and the number of observed events with two identified kaons, N_{2K} , each have Poisson probability distributions. The Poisson means of these distributions

Table 17. The efficiencies for each of the charge categories used to determine the branching ratios for the decays $\tau^\pm \rightarrow K^+K^-\pi^\pm\nu_\tau$ and $\tau^\pm \rightarrow K^\pm\pi^+\pi^-\nu_\tau(\pi^0)$.

Multiprong Efficiencies			
Mode	Event Category		
	$Q_\tau = Q_K$	$Q_\tau = -Q_K$	2-kaons
$\tau^\pm \rightarrow K^+K^-\pi^\pm\nu_\tau$	$(2.92 \pm 0.85)\%$	$(2.92 \pm 0.85)\%$	$(1.65 \pm 0.14)\%$
$\tau^\pm \rightarrow K^\pm\pi^+\pi^-\nu_\tau(\pi^0)$	$(4.2 \pm 0.6)\%$	0.0	0.0

are given by:

$$\begin{aligned}
\langle N_{1K}^{os} \rangle_{Poisson} &= 2 \cdot L \cdot \sigma \cdot \left[\epsilon_{KK\pi}^{1K} \cdot \frac{BR_{KK\pi}}{2} \right] \equiv \frac{\mu_{KK\pi}^{1K}}{2} \\
\langle N_{1K}^{ss} \rangle_{Poisson} &= 2 \cdot L \cdot \sigma \cdot \left[\epsilon_{K\pi\pi}^{1K} \cdot BR_{K\pi\pi} + \epsilon_{KK\pi}^{1K} \cdot \frac{BR_{KK\pi}}{2} \right] \\
&\equiv \left(\mu_{K\pi\pi}^{1K} + \frac{\mu_{KK\pi}^{1K}}{2} \right) \\
\langle N_{2K} \rangle_{Poisson} &= 2 \cdot L \cdot \sigma \cdot \left[\epsilon_{KK\pi}^{2K} \cdot BR_{KK\pi} \right] \equiv \mu_{KK\pi}^{2K}
\end{aligned} \tag{16}$$

where L is the luminosity, σ is the cross section used to calculate the efficiencies, and the ϵ correspond to the efficiencies in Table 17. The likelihood, L , that a data sample contains the observed numbers of events N_{1K}^{os} , N_{1K}^{ss} , and N_{2K} , is given by the formula:

$$\begin{aligned}
L(N_{1K}^{os}, N_{1K}^{ss}, N_{2K}) &= \frac{1}{N_{1K}^{os}! N_{1K}^{ss}! N_{2K}!} \times \\
&e^{-(\mu_{KK\pi}^{1K} + \mu_{K\pi\pi}^{1K} + \mu_{KK\pi}^{2K})} \\
&\left(\frac{\mu_{KK\pi}^{1K}}{2} \right)^{N_{1K}^{os}} \times (\mu_{KK\pi}^{2K})^{N_{2K}} \\
&\left(\mu_{K\pi\pi}^{1K} + \frac{\mu_{KK\pi}^{1K}}{2} \right)^{N_{1K}^{ss}} \times
\end{aligned} \tag{17}$$

A maximization of this function, using the MINUIT³³ minimization program, with free parameters $BR_{KK\pi}$ and $BR_{K\pi\pi}$, is performed. The most probable branching fractions are:

$$\begin{aligned} BR(\tau^\pm \rightarrow K^+ K^- \pi^\pm \nu_\tau) &= (0.22_{-0.11}^{+0.17})\% \\ BR(\tau^\pm \rightarrow K^\pm \pi^+ \pi^- \nu_\tau (\pi^0)) &= (0.22_{-0.13}^{+0.16})\% \end{aligned} \quad (18)$$

where the errors are statistical only and the errors in Eqn. 18 are the correlated errors. Figure 42 demonstrates that the branching ratios are correlated.

The largest systematic error is due to the uncertainty in the amount of background. This contributes a 20% systematic uncertainty to the branching ratios which is, however, much less than the statistical error of the measurement. In addition there are contributions from uncertainties in the efficiency determination (5%), the luminosity (7%), and the single prong branching ratio 2%.

§§4.5.3 *Determination of an Upper Bound on m_{ν_τ}*

The previous section was concerned with measuring the branching ratios of the decay modes $\tau^\pm \rightarrow K^+ K^- \pi^\pm \nu_\tau$ and $\tau^\pm \rightarrow K^\pm \pi^+ \pi^- \nu_\tau (\pi^0)$. The selection criteria developed for this purpose must be modified for the purpose of identifying the second kaon in the decay $\tau^\pm \rightarrow K^+ K^- \pi^\pm \nu_\tau$. Fortunately, since the kaons each have a relatively high mass of $0.494 GeV/c^2$, there is a high probability ($\approx 40\%$) that both of the kaons will be above pion threshold. Of the nine events found, one event has a second kaon identified with the kaon identification requirements as developed for the branching ratio analysis. It is not necessary to require as high a pion rejection on the second kaon as was required of the first kaon in the event. This is because

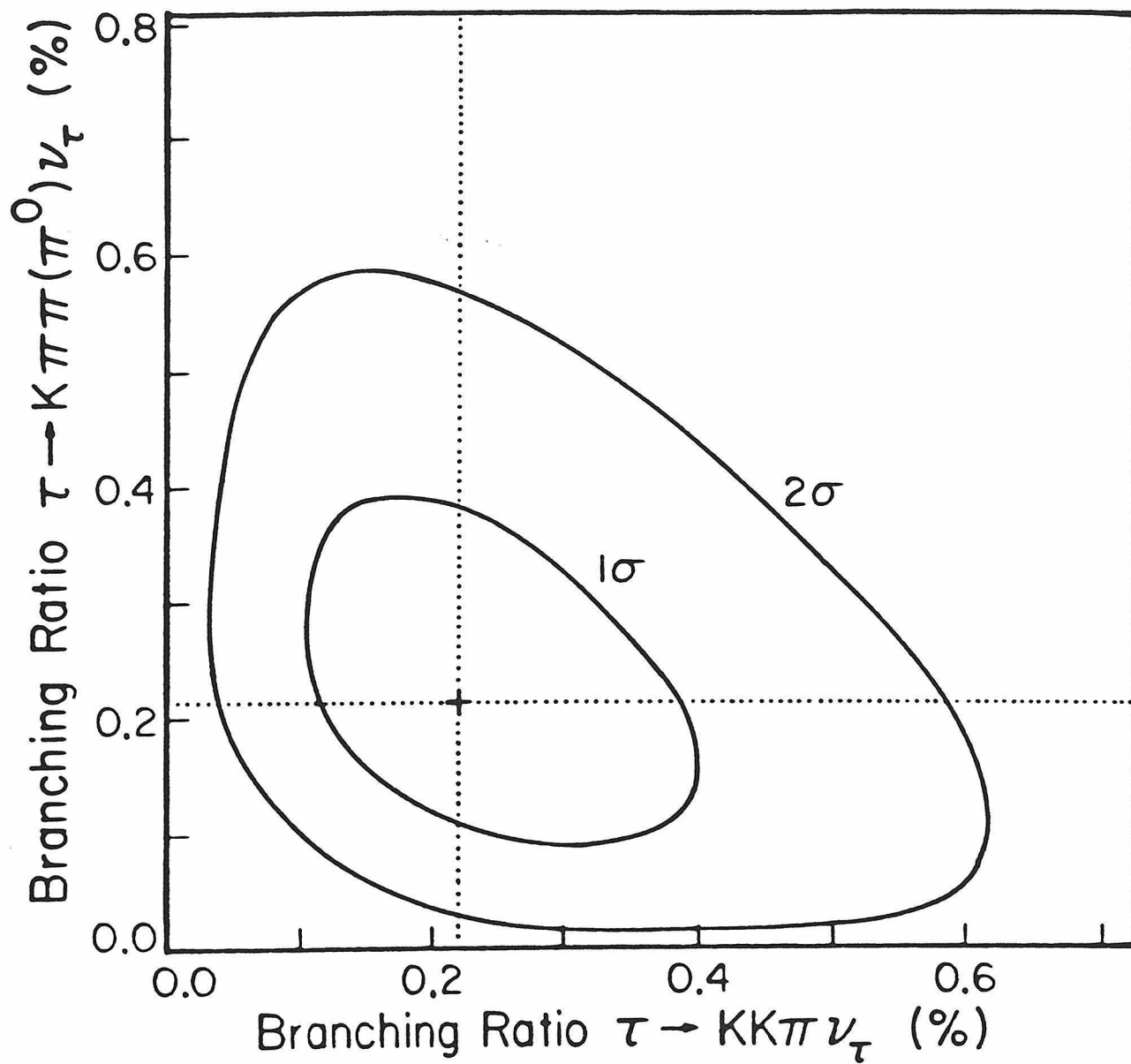


Figure 42. The 1σ , 2σ , and 3σ contours of the likelihood function used in the branching ratio fit. The correlations between the two branching ratios are demonstrated in this graph.

the misidentification probability for the second track is uncorrelated with that of the first so that the total pion rejection is the product of the two individual track pion rejections. Hadronic events are also suppressed because of the requirement that there be two kaons at high momentum. The dominant background comes from pion misidentification in the events from $\tau^\pm \rightarrow K^\pm \pi^+ \pi^- \nu_\tau (\pi^0)$ decay, which has a very small branching ratio.

To see how to make the kaon requirement less stringent, the Cherenkov misidentification probability defined section is useful:

$$P_{miss} = \sum_{n=0}^{N_{cut}} \frac{1}{n!} (\mu_{pe})^n e^{-\mu_{pe}} \quad (19)$$

where

$$\mu_{pe} = \begin{cases} \overline{N}_{pe}^{Bhabha}(\cos\theta) \cdot \left(1 - \frac{p_0^2}{p^2}\right) & p \geq p_0 \\ 0 & p < p_0 \end{cases} .$$

In this formula the Poisson mean for the number of photo-electrons expected for a pion with momentum p is given by μ_{pe} and the photo-electron cut is given by N_{cut} . This mean, μ_{pe} , is taken as the mean measured for Bhabha electrons, $\overline{N}_{pe}^{Bhabha}(\cos\theta)$, multiplied by the threshold momentum dependence, $\left(1 - \frac{p_0^2}{p^2}\right)$ where $p_0 = 2.65 \text{ GeV}/c$. P_{miss} is the probability that a pion at momentum p and angle $\cos\theta$ yields to a Cherenkov pulseheight below the photo-electron cut. This variable may be plotted for all pairs of tracks in the above 9 events, regardless of momentum. It is known, however, that only kaons of opposite charge can be true candidates for the decay $\tau^\pm \rightarrow K^+ K^- \pi^\pm \nu_\tau$, and also that misidentified pions will yield both same sign and opposite sign kaon pairs. Figure 43 shows the scatter plot of P_{miss} for all pairs of tracks in the candidate events. The identified $K^+ K^-$ pairs appear in the opposite sign scatter plot with $P_{miss} \approx 0$ for both tracks. After requiring that all tracks have $P_{miss} < 0.1$ there are four events remaining as two kaon candidates. The three events which are known to be from the decay $\tau^\pm \rightarrow K^+ K^- \pi^\pm \nu_\tau$, ie the 2 kaon event and the two opposite sign events, are found to have a second kaon

present. A fourth event comes from the same sign category. The backgrounds from pion misidentification are, from Monte Carlo predictions, $(.03 \pm 0.02)$ events. The hadronic background, estimated as in the previous section by using the number of events observed in the topological classes 1-5, 3-3, and 3-5 to extrapolate the hadron Monte Carlo prediction into the 1-3 topology, is found to be (0.03 ± 1.5) . The steeply falling momentum distributions in hadronic events give a suppression of events containing two kaons at high momentum.

The four events are shown in Fig. 44, Fig. 45, Fig. 46, Fig. 47 along with some of the properties of each event.

In order to determine an upper bound on m_{ν_τ} it is necessary to have knowledge about the decay mechanism responsible for the process $\tau^\pm \rightarrow K^+K^-\pi^\pm\nu_\tau$. Specifically, $\Gamma_{KK\pi}(q, m_{\nu_\tau})$, the decay rate for $\tau^\pm \rightarrow K^+K^-\pi^\pm\nu_\tau$, must be known, where q is the mass of the $KK\pi$ system and m_{ν_τ} is the τ neutrino mass. On one extreme, the model that the $KK\pi$ invariant mass is produced with a phase space distribution can be assumed. This, it turns out, gives the lowest bound on the neutrino mass. The theoretically favored model¹⁵ involves a resonant $\rho'(1600)$ as an intermediate state which then decays into $KK\pi$ via a $K^*(890)\bar{K}$ intermediate state. In this case $BR(\tau^\pm \rightarrow K^+K^-\pi^\pm\nu_\tau)$ may be calculated by using CVC as an assumption and gives the result $BR(\tau^\pm \rightarrow K^+K^-\pi^\pm\nu_\tau) = (0.24 \pm 0.10)\%$, in good agreement with the observed value of $(0.22_{-0.11}^{+0.17})$. This model is used in the final analysis because it gives the most conservative (*i.e.*, the highest) upper bound on m_{ν_τ} . The form of $\Gamma_{KK\pi}(q, m_{\nu_\tau})$ is shown in Figure 48.

A comparison of the theoretically predicted decay rate to the measured invariant mass distribution may be made if one has a knowledge of the mass resolution of the apparatus. Since the resolution functions are inherently non-Gaussian, it is necessary to take some care in evaluating them. The invariant mass of the $KK\pi$ system is determined by the momentum vectors of the three tracks. In the apparatus the directions are well determined and the resolution in the invariant mass is dominated by the smearing in the momentum measurement. This has the

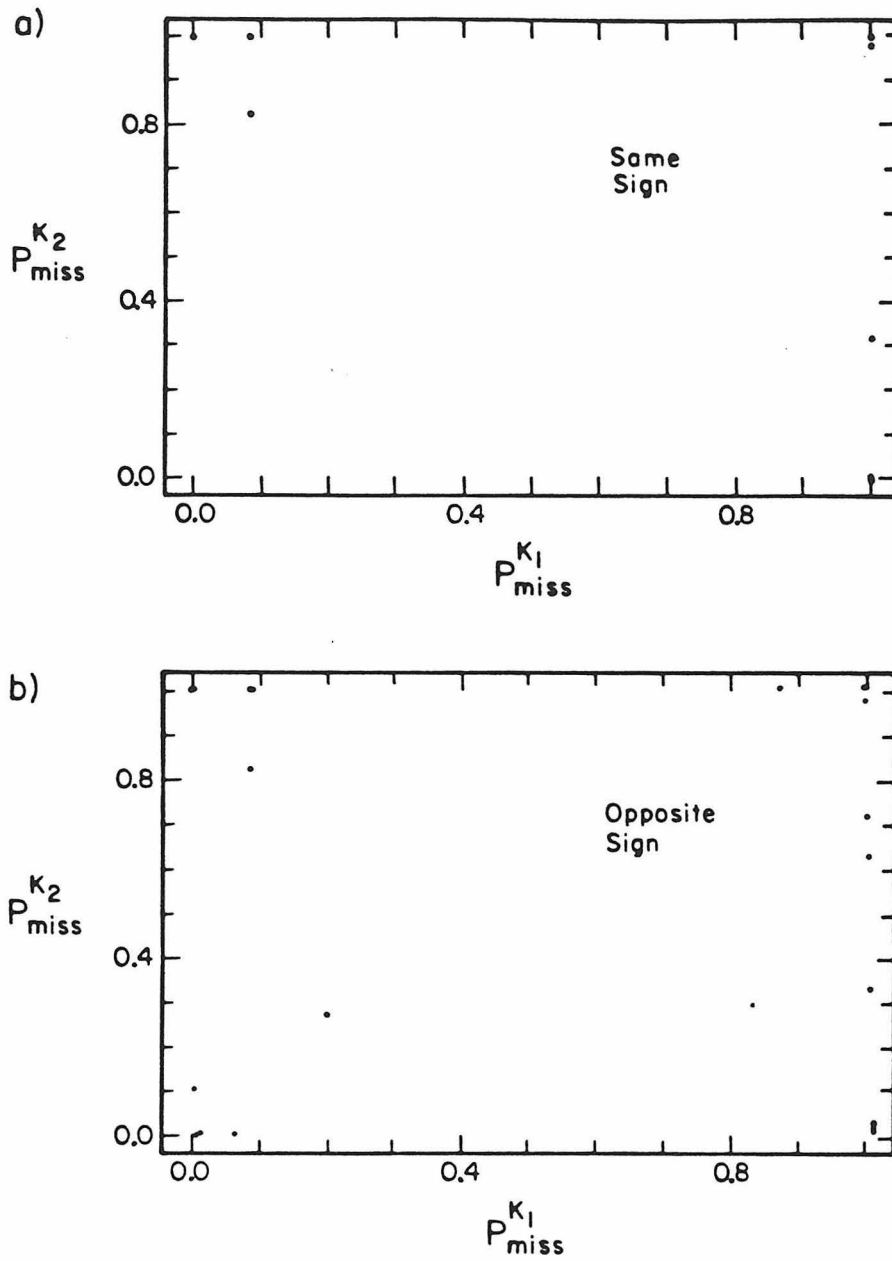


Figure 43. The scatter plots of P_{miss} for opposite-sign and same-sign pairs of tracks (Cherenkov off) from the 9 multi-prong kaon events. The signal from true K^+K^- pairs is seen in the lower left hand corner of the opposite sign scatter plot.

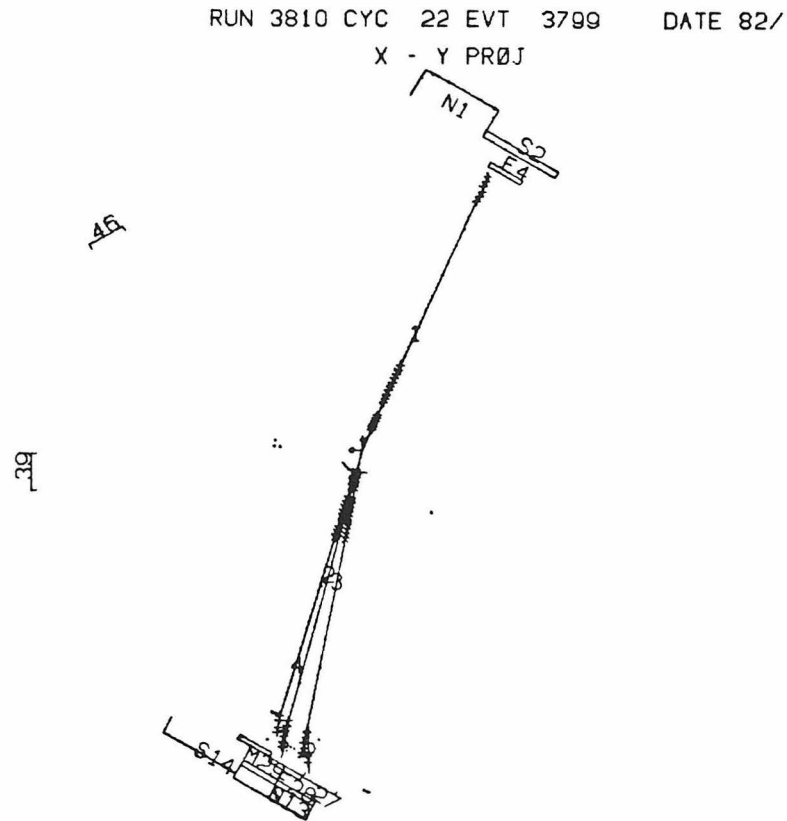


Figure 44. Event 1.

- $K^+K^-\pi$: tracks 2,3, and 4
 - 1 : $p = 2.18 \text{ GeV}/c$, 0.0 *p.e.*
 - 2 : $p = 5.14 \text{ GeV}/c$, 0.0 *p.e.* (K)
 - 3 : $p = 4.75 \text{ GeV}/c$, 0.0 *p.e.* (K)
 - 4 : $p = 1.90 \text{ GeV}/c$, 0.0 *p.e.*

RUN 4343 CYC 22 EVT 4157 DATE 82/
X - Y PROJ

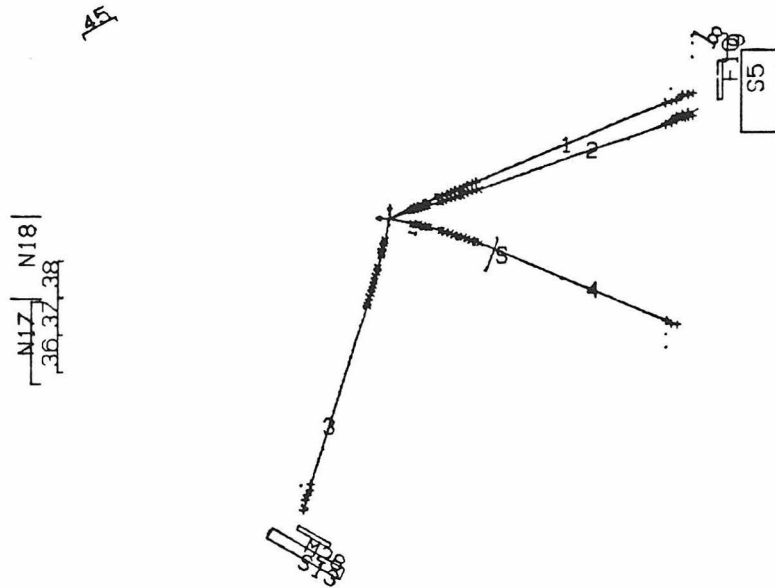


Figure 45. Event 2.

- $K^+K^-\pi$: tracks 1,2, and 4
 - 1 : $p = 4.70 \text{ GeV}/c$, 0.0 p.e. (K)
 - 2 : $p = 2.93 \text{ GeV}/c$, 0.0 p.e. (K)
 - 3 : $p = 0.71 \text{ GeV}/c$. 0.0 p.e.
 - 4 : $p = 0.48 \text{ GeV}/c$. 0.0 p.e.

RUN 5139 CYC 53 EVT 3773 DATE 83/
X - Y PROJ

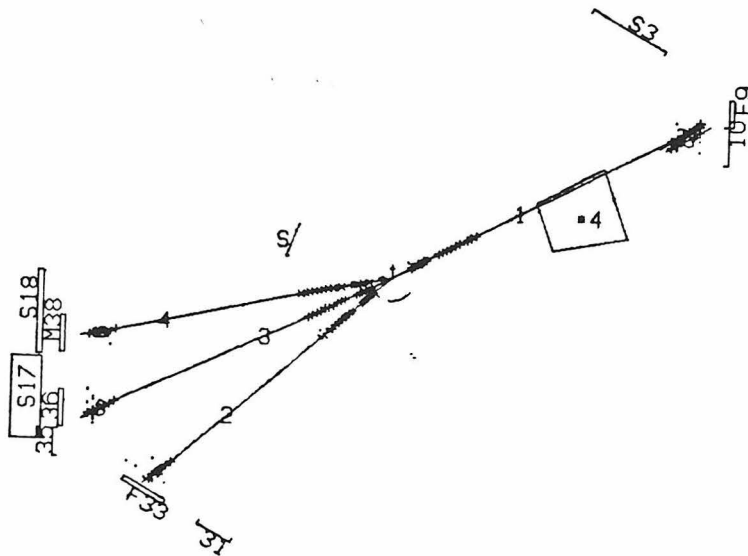


Figure 46. Event 3.

- $K^+K^-\pi$: tracks 2,3, and 4
 - 1 : $p = 3.82 \text{ GeV}/c$, 11.5 p.e. (K)
 - 2 : $p = 4.91 \text{ GeV}/c$, 0.0 p.e. (K)
 - 3 : $p = 4.05 \text{ GeV}/c$. 0.0 p.e.
 - 4 : $p = 1.01 \text{ GeV}/c$. 0.0 p.e.

RUN 7769 CYC 165 EVT 11513 DATE 84/
X - Y PROJ

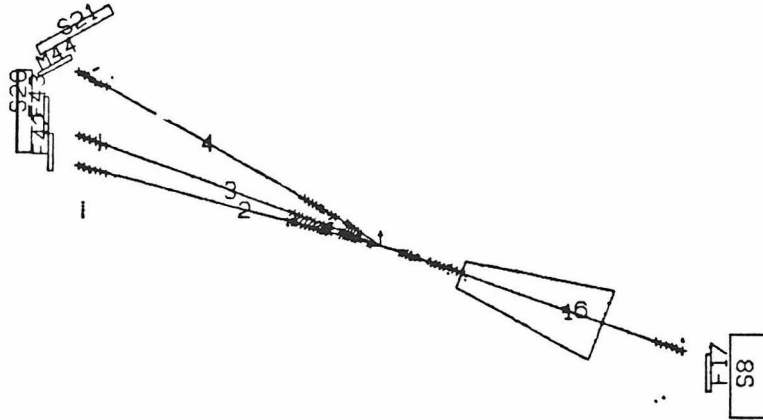


Figure 47. Event 4.

- $K^+K^-\pi$: tracks 2,3, and 4
 - 1 : $p = 5.61 \text{ GeV}/c$, 44.5 p.e. (K)
 - 2 : $p = 4.10 \text{ GeV}/c$, 0.0 p.e. (K)
 - 3 : $p = 6.01 \text{ GeV}/c$. 0.0 p.e.
 - 4 : $p = 0.91 \text{ GeV}/c$. 0.0 p.e.

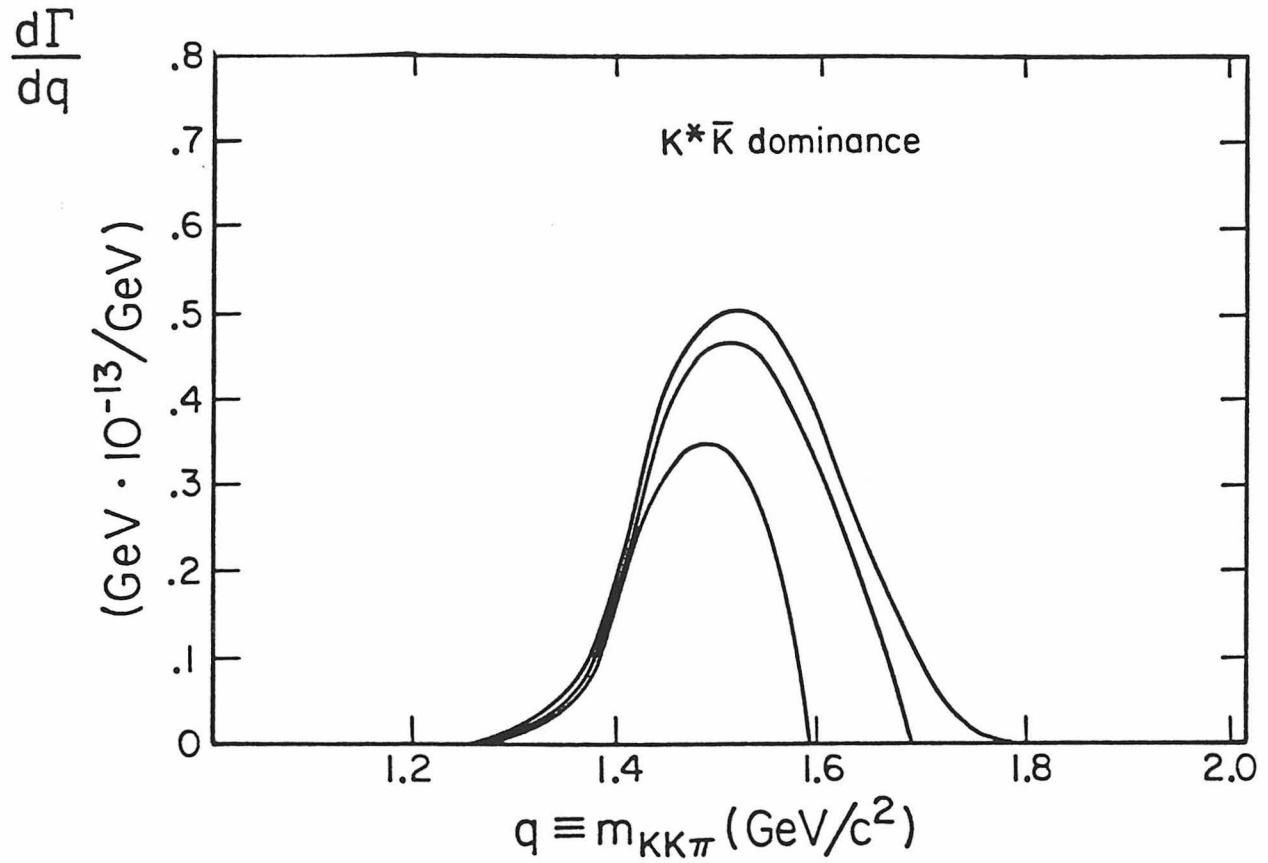


Figure 48. The theoretically predicted decay rate, $\Gamma_{KK\pi}(q, m_{\nu_\tau})$, as a function of the mass of the $KK\pi$ system, q . Note that the end point of the distribution is determined by the mass of the τ minus the mass of the τ neutrino.

effect of making the resolution functions asymmetric and also not centered about zero. To accurately calculate these effects the measured momentum vectors of the tracks for each of the four events are used as input to the Monte Carlo event simulator. The simulator included randomly the effects of drift chamber resolution, measurement error, multiple scattering, and wire noise and inefficiencies. Each event is then simulated many times and the distribution of measured invariant mass minus the original (input) invariant mass is generated. The results are shown in Figure 49. The histograms thus generated are fit to a functional form which is shown drawn over the histograms in Fig. 49. In the end, the likelihood fit is not sensitive to the precise widths of the resolutions.

It is now possible to construct a likelihood function for m_{ν_τ} given the four observed events with measured invariant masses m_i . The probability $P(q, m_i, m_{\nu_\tau})$ that an event is produced with a $KK\pi$ mass of q which is then measured to have a mass of m_i is a function of m_{ν_τ} and given by:

$$P(q, m_i, m_{\nu_\tau}) = \frac{\Gamma_{KK\pi}(q, m_{\nu_\tau})}{\Gamma_{KK\pi}^{tot}(m_{\nu_\tau})} \times R(q, m_i) \times \epsilon(q) \quad (20)$$

where $\Gamma_{KK\pi}(q, m_{\nu_\tau})$ ($\Gamma_{KK\pi}^{tot}(m_{\nu_\tau})$) is the partial(total) decay rate for the reaction $\tau^\pm \rightarrow K^+K^-\pi^\pm\nu_\tau$, $R(q, m_i)$ is the event resolution function, and $\epsilon(q)$ is the event selection efficiency as a function of q . The efficiency $\epsilon(q)$ is not significantly dependent on q in the range between $1.3\text{GeV}/c^2$ and $1.784\text{GeV}/c^2$ which is of interest and does not affect the likelihood. The likelihood function for the entire sample is the product of the individual event probabilities after integration over the unknown variable q .

$$L(m_{\nu_\tau}) = \prod_{i=\text{events}} \int dq P(q, m_i, m_{\nu_\tau}) \quad (21)$$

The maximum of $L(m_{\nu_\tau})$ thus determines the most probable value of m_{ν_τ} . The most probable value is zero with a 95% CL upper bound of $157\text{MeV}/c^2$ for m_{ν_τ} .

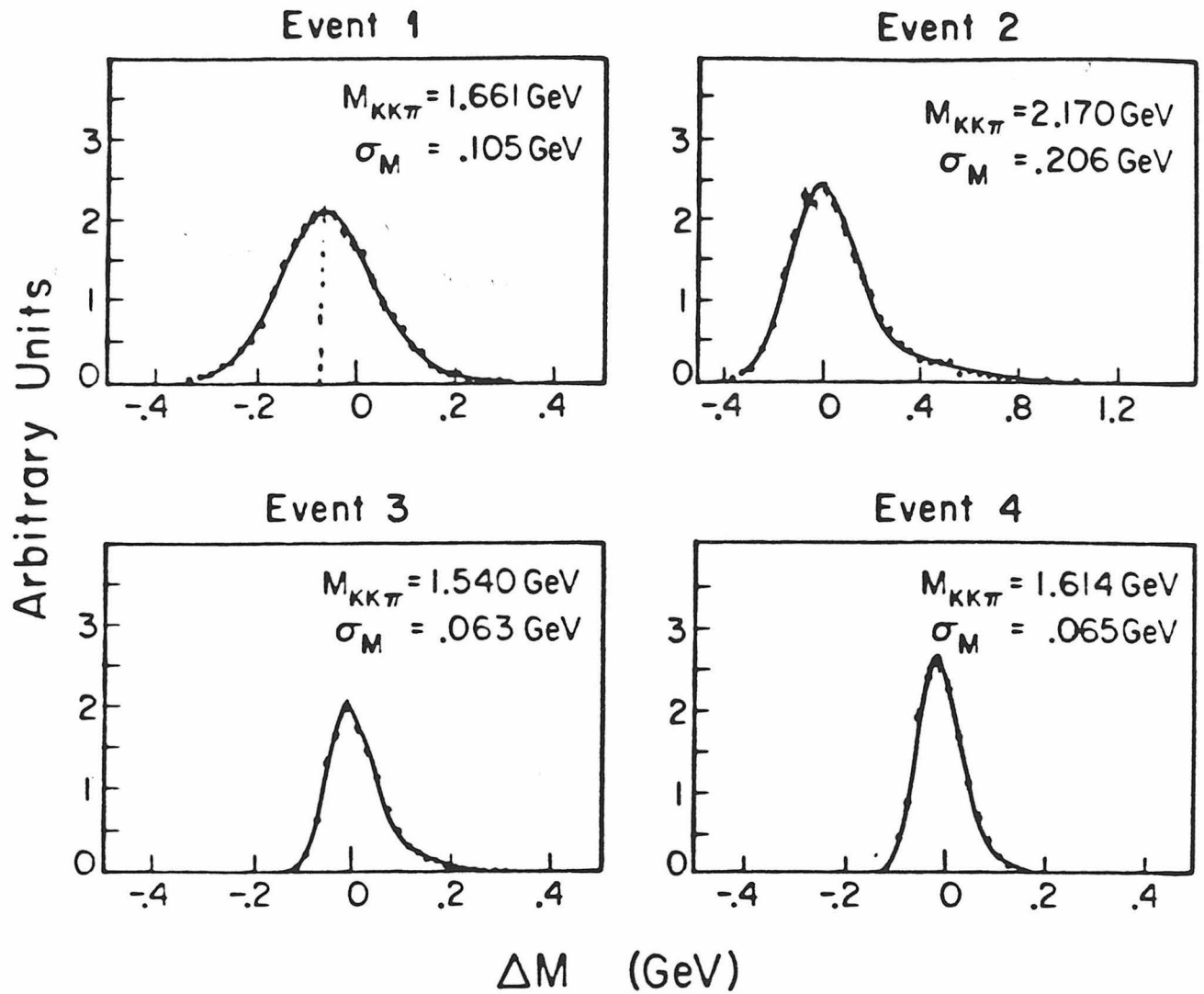


Figure 49. The invariant mass resolution functions for the four events used in the neutrino mass likelihood fit.

As mentioned previously the fit is insensitive to variations in the widths of the resolution functions. The decay model which is theoretically favored, $\tau^\pm \rightarrow \rho^\pm(1580)\nu_\tau \rightarrow K^*\bar{K} \rightarrow K^+K^-\pi^\pm$, also gives the most conservative mass limit of the two models. The momentum scale has been measured using $\mu^+\mu^-$ events and $\rho^0(770) \rightarrow \pi^+\pi^-$ decays from τ decays. These verify that the momentum scale is as expected from magnetic field measurements.

Chapter 5. Results and Conclusion

This chapter discusses the results of the analysis in the previous chapter. In the case of the decay $\tau^\pm \rightarrow K^\pm \nu_\tau$ very accurate theoretical predictions of the decay rate allow for a stringent test of lepton universality. The decays $\tau^\pm \rightarrow K^\pm \nu_\tau + n\pi^0$, $\tau^\pm \rightarrow K^+ K^- \pi^\pm \nu_\tau$, and $\tau^\pm \rightarrow K^\pm \pi^+ \pi^- \nu_\tau (\pi^0)$ are less certain theoretically. However, these modes allow for the testing of some of the SU(3) sum rules³⁴, which relate the decay rates of the τ into hadronic resonances to each other.

The first section discusses the decays involving the lowest pseudoscalar mesons, π and K , which may be related to π and K decay into lighter leptons. This provides a direct test of the universality of pseudoscalar hadrons with the leptonic currents.

The second section discusses the decay of the τ into vector hadronic states. The consideration of these decays allows one to predict the decay branching ratios for the multi-particle hadronic final states such as $\tau^\pm \rightarrow K^\pm \nu_\tau + n\pi^0$, $\tau^\pm \rightarrow K^\pm \pi^+ \pi^- \nu_\tau (\pi^0)$, and $\tau^\pm \rightarrow K^+ K^- \pi^\pm \nu_\tau$. These provide tests for the theoretical input of the Weinberg-Das-Mathur-Okubo sum rules for V-A currents in weak interactions.

The last section discusses the theoretical model for the $\tau^\pm \rightarrow K^+ K^- \pi^\pm \nu_\tau$ decay in the context of a massive τ neutrino. This model was used to determine an upper bound on m_{ν_τ} in the previous chapter. Finally, the significance of massive neutrinos is touched upon from the experimental point of view and also from the point of view of astrophysics.

§5.1 Decays Involving the Pseudoscalars π and K

The charged current interactions of the pseudoscalar mesons π and K with all three leptons, the $e\bar{\nu}_e$, $\mu\bar{\nu}_\mu$, and $\tau\bar{\nu}_\tau$, have now been determined. These provide an important test of lepton universality which is free of theoretical uncertainty involving the strong interactions. Because these interactions take place at a fixed q^2 , namely the pion and kaon masses, the strong interaction dynamics between the quarks inside the meson are completely taken into account by a constant, f_π or f_K , representing the vacuum expectation value for producing the pion or the kaon, respectively.

The diagrams for the decays are shown in Figure 50. The decay rates for these diagrams have been calculated^{15,12} and can be written,

$$\Gamma_{\pi^\pm \rightarrow l^\pm \nu_l}^{pred} = \frac{G^2 f_\pi^2 \cos^2 \theta_c}{8\pi} m_\pi m_l^2 \left(1 - \frac{m_l^2}{m_\pi^2}\right)^2 \quad (22)$$

where G is the Fermi coupling, f_π is the pion form factor, θ_c is the Cabibbo angle, and l may be either an electron (e) or muon (μ). The related τ decay rate may be written

$$\Gamma_{\tau^\pm \rightarrow \pi^\pm \nu_\tau}^{pred} = \frac{1}{2} \frac{G^2 f_\pi^2 \cos^2 \theta_c}{8\pi} m_\tau^3 \left(1 - \frac{m_\pi^2}{m_\tau^2}\right)^2 \quad (23)$$

It is important to note that f_π is the same in all cases, since it is only a function of $q^2 = m_\pi^2$.

Similarly,

$$\Gamma_{K^\pm \rightarrow l^\pm \nu_l}^{pred} = \frac{G^2 f_K^2 \cos^2 \theta_c}{8\pi} m_K m_l^2 \left(1 - \frac{m_l^2}{m_K^2}\right)^2 \quad (24)$$

and

$$\Gamma_{\tau^\pm \rightarrow K^\pm \nu_\tau}^{pred} = \frac{1}{2} \frac{G^2 f_K^2 \cos^2 \theta_c}{8\pi} m_\tau^3 \left(1 - \frac{m_K^2}{m_\tau^2}\right)^2 \quad (25)$$

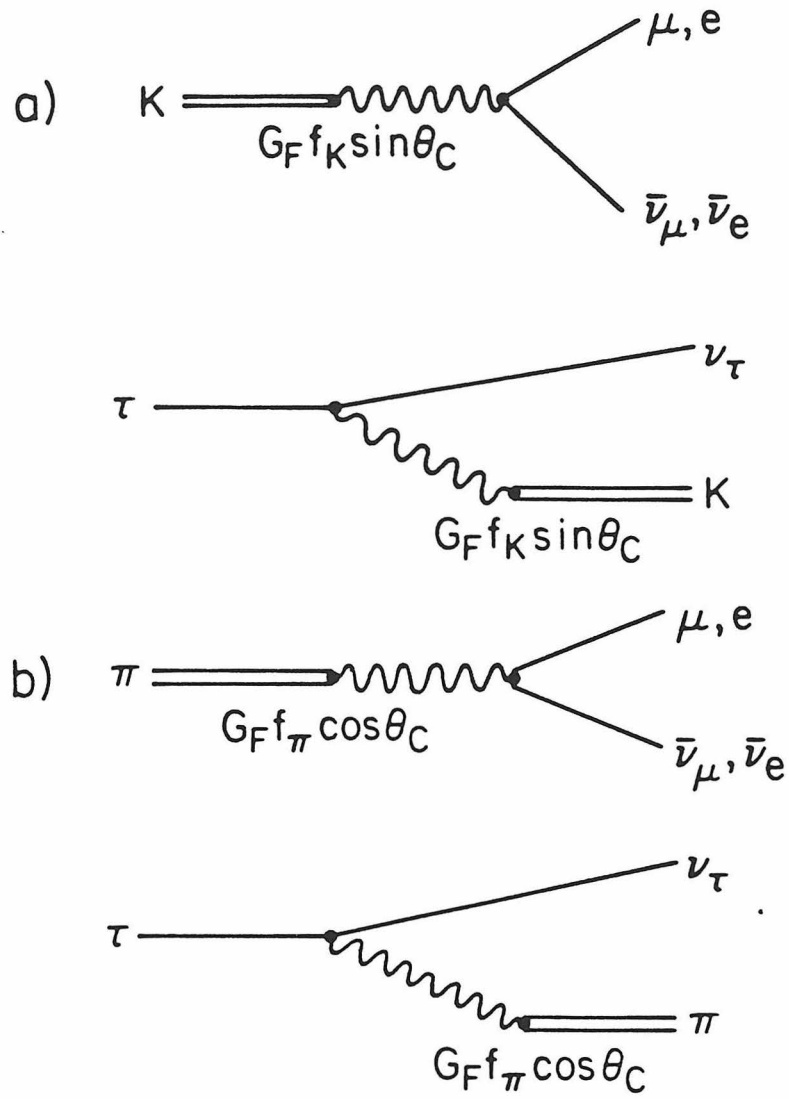


Figure 50. Feynman diagrams for $\tau^\pm \rightarrow K^\pm \nu_\tau$, $\tau^\pm \rightarrow \pi^\pm \nu_\tau$, $K^\pm \rightarrow l^\pm \nu_l$, and $\pi^\pm \rightarrow l^\pm \nu_l$. The same form factor f_K or f_π appears in each decay.

In order to compare the theoretical predictions to experiment it is convenient to cast all of the rates into a normalized form. The crucial question to be addressed is the relative strength of the interactions between leptons, *i.e.*, lepton universality. By normalizing all of the measured rates, $\Gamma_{Xl\nu}^{meas}$ to the measured muon rate $\Gamma_{X\mu\bar{\nu}_\mu}^{meas}$ and then dividing by the corresponding theoretically predicted ratio, $\Gamma_{Xl\nu}^{pred}/\Gamma_{X\mu\bar{\nu}_\mu}^{pred}$, the parameter ρ may be formed:

$$\rho_{Xl} = \frac{\Gamma_{Xl\nu}^{meas}/\Gamma_{X\mu\bar{\nu}_\mu}^{meas}}{\Gamma_{Xl\nu}^{pred}/\Gamma_{X\mu\bar{\nu}_\mu}^{pred}} \quad (26)$$

where $X = \pi$ or K and $l = e, \mu$, or τ . If lepton universality holds then ρ should be consistent with 1 in all cases (by construction it is equal to 1 in the case of $l = \mu$).

Since one does not directly measure the decay rates, the decay rate must be formed from the branching ratio of the given decay and the lifetime of the decaying particle using the standard formulae,

$$\Gamma_{A \rightarrow B} = \frac{\hbar}{\tau_A} b_{A \rightarrow B}$$

where τ is the lifetime and b is the branching ratio of the process. Therefore, the lifetimes and branching ratios are needed for the pion, kaon, and τ particles.

First consider the pion. The lifetime is measured by Ayres et al.³⁵ and found to be $(2.604 \pm 0.002) \times 10^{-10} s$ by using a decay-in-flight technique. The most accurate measurement of the branching ratio $b_{\pi e \bar{\nu}_e}$ of the pion into electron and electron neutrino was made by Bryman et al.³⁶. They find $b_{\pi e \bar{\nu}_e} = (1.218 \pm 0.024) \times 10^{-4}$ by a method using stopped pions. The branching ratio to muons³⁷ is 0.999975 ± 0.00001 obtained by using $b_{\pi \mu \bar{\nu}_\mu} = 1 - b_{\mu \nu_\mu \gamma} - b_{e \bar{\nu}_e}$. As for the kaon, Ott et al.³⁸ have measured the kaon lifetime using kaons at rest to be $(12.380 \pm 0.016) \times 10^{-9} s$. The kaon has many final states so that $b_{K \mu \bar{\nu}_\mu}$ and $b_{K e \bar{\nu}_e}$ must be measured independently. The best measurement of $b_{K \mu \bar{\nu}_\mu}$ is by Chaing et al.³⁹, who find $b_{K \mu \bar{\nu}_\mu} = (63.24 \pm 0.44)\%$. The ratio $b_{K e \bar{\nu}_e}/b_{K \mu \bar{\nu}_\mu}$ has been

measured by Heintz et al.⁴⁰, and found to be $(2.42 \pm 0.11) \times 10^{-5}$. This results in $b_{Ke\bar{\nu}_e} = (1.530 \pm 0.070) \times 10^{-5}$.

The measurements on τ decay are not as precise as in the case of π and K decay due to the small numbers of events which have been produced to date. The $\tau^\pm \rightarrow \pi^\pm \nu_\tau$ branching ratio has been measured by two groups, Behrend et al.⁴¹ and by Blocker et al.,⁴², to comparable accuracy. The weighted average of the measurements (which are consistent with each other) is $b_{\pi\tau\nu_\tau} = (10.3 \pm 1.2)\%$. The most accurate measurement of the branching ratio of the decay $\tau^\pm \rightarrow K^\pm \nu_\tau$ is one of the results of this thesis, $b_{K\tau\nu_\tau} = (0.57 \pm 0.14)\%$ ⁴³. Finally, the τ lifetime has been measured to be $\tau_\tau = (2.86 \pm 0.30) \times 10^{-13}$ by Jaros et al.⁴⁴. A summary of the experimental measurement is shown in Table 18. The parameter ρ_{Xl} , as given in Equation 26, is sensitive to couplings which distinguish between the three leptons. After using the measured rates to calculate the $\Gamma_{Xl\nu_l}^{meas}$ in Equation 26 and using the predicted values to calculate the $\Gamma_{Xl\nu_l}^{pred}$ one obtains ρ_{Xl} for the six different combinations of the leptons (l) and pseudoscalar mesons (X). These values are shown in Figure 51. The $\tau^\pm \rightarrow K^\pm \nu_\tau$ point is the contribution of this experiment and is a major step in confirming the τ lepton's universality with the electron and muon.

In order to see quantitatively what this measurement means in terms of universality, a simple extension of the standard weak interaction picture can provide the necessary tools. The most reasonable way of making this extension would be to suppose that there exists an additional axial vector/scalar coupling with the Fermi interaction strength multiplied by a coupling of this model, g . The parameter g may depend upon which particle or lepton is involved. The weak currents for such a process may be written as

$$\begin{aligned}
 J_\mu &= \frac{G_F}{\sqrt{2}} \{ \cos\theta_c \bar{u}\Gamma d + \sin\theta_c \bar{u}\Gamma s + \bar{\nu}_l\Gamma l \} \\
 &+ \frac{G_F}{\sqrt{2}} \{ g_{q1} \bar{u}\Gamma' d + g_{q2} \bar{u}\Gamma' s + g_l \bar{\nu}_l\Gamma' l \}
 \end{aligned} \tag{27}$$

Table 18. These measurements represent the best numbers available. They determine the pseudoscalar couplings to the three lepton currents. (see text for references)

Lifetimes and Branching Ratios	
Particle	Measurement
π	$\tau_\pi = (26.04 \pm 0.02) \times 10^{-9} s$ $b_{\pi\mu\bar{\nu}_\mu} = 1 - 2.5 \times 10^{-4}$ $b_{\pi e\bar{\nu}_e} = (1.218 \pm 0.024) \times 10^{-4}$
K	$\tau_K = (12.380 \pm 0.016) \times 10^{-9} s$ $b_{K\mu\bar{\nu}_\mu} = (63.24 \pm 0.44)\%$ $b_{K e\bar{\nu}_e} = (1.530 \pm 0.070) \times 10^{-5}$
τ	$\tau_\tau = (2.86 \pm 0.30) \times 10^{-13} s$ $b_{\pi\tau\bar{\nu}_\tau} = (10.3 \pm 1.2)\%$ $b_{K\tau\bar{\nu}_\tau} = (0.57 \pm 0.14)\%$

where: l corresponds to one of the leptons: e , μ , or τ ; Γ' corresponds to the additional axial vector/scalar coupling matrix; and finally, g_{q_1} , g_{q_2} , and g_l correspond to the various couplings with the quarks and leptons involved in the decays. By squaring this current one obtains the interaction Lagrangian and interference between the standard terms and the additional terms present. This interference term has the effect of increasing the decay rate over the predicted value of $b_{K\tau\bar{\nu}_\tau} = (0.71 \pm 0.11)\%$ which is obtained by using the muon lifetime and the measured branching ratio for the decay $\tau^\pm \rightarrow e^\pm \bar{\nu}_e \nu_\tau$. The result, which assumes $g_{q_2} \ll \sin\theta_c$, is that

$$(g_\tau - g_\mu) < 0.08 \quad \text{at } 95\% \text{ CL} \quad . \quad (28)$$

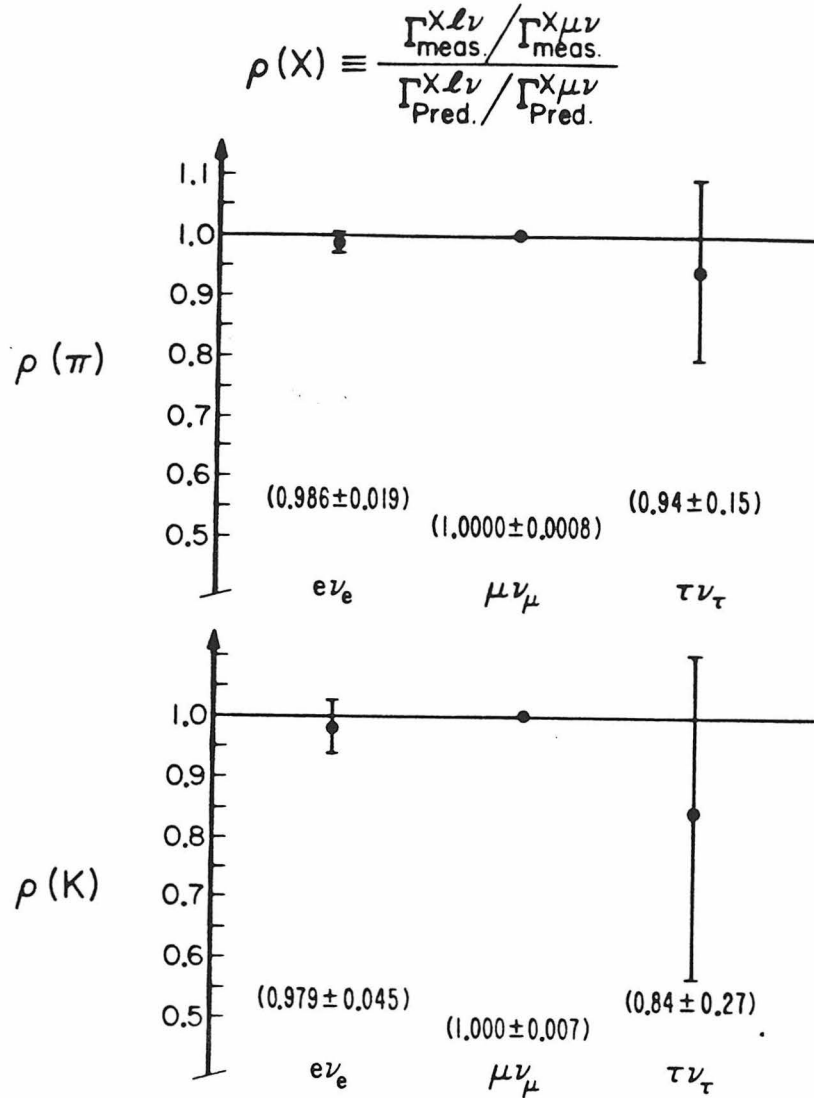


Figure 51. This figure compares the measured decay rates for the decays $\pi^\pm \rightarrow e^\pm \nu_e$, $\pi^\pm \rightarrow \mu^\pm \nu_\mu$, and $\tau^\pm \rightarrow \pi^\pm \nu_\tau$ in the Cabibbo-favored channel and compares the measured decay rates for the decays $K^\pm \rightarrow e^\pm \nu_e$, $K^\pm \rightarrow \mu^\pm \nu_\mu$, and $\tau^\pm \rightarrow K^\pm \nu_\tau$ in the Cabibbo-suppressed channel. The quantity plotted, ρ , is normalized so that it is equal to unity if lepton universality holds.

In other words, the presence of an additional interaction is limited to 8% of the weak interaction strength. This corresponds to a mass scale of roughly 300 GeV, assuming that the particle couples with the standard weak coupling strength.

§5.2 Multiprong Decays

The decay of the τ into final states containing more than one hadron is thought to be dominated by vector resonances and axial vector resonances. The decay rates for these processes can be predicted from SU(3) sum rules.

The decay rate may be written¹²

$$\Gamma(\tau \rightarrow \text{hadrons} + \nu_\tau) = \frac{G^2}{(2\pi)^2 (2m_\tau)^3} \int_0^{m_\tau^2} dq^2 (m_\tau^2 - q^2)^2 \times$$

$$\left[\{(m_\tau^2 + 2q^2)(v_1(q^2) + a_1(q^2)) + m_\tau^2 a_0(q^2)\} \cos\theta_c + \right.$$

$$\left. \{(m_\tau^2 + 2q^2)(v_1^S(q^2) + a_1^S(q^2)) + m_\tau^2 a_0^S(q^2)\} \sin\theta_c \right]. \quad (29)$$

The spectral functions are given by: $v_1(q^2)$, the vector component; $a_1(q^2)$, the axial vector component; $a_0(q^2)$, the pseudoscalar component; $v_1^S(q^2)$, the strange vector component; $a_1^S(q^2)$, the strange axial vector component; $v_0^S(q^2)$, the strange scalar component; and finally $(a_0^S(q^2))$, the strange pseudoscalar component. Table 19 shows the various hadronic states which couple to the spectral functions.

The decay spectral function $v_1(q^2)$ may be related via CVC to the e^+e^- cross section for the like channel in the I=1 state:

$$v_1(q^2) = \frac{q^2 \sigma_{I=1}^{e^+e^-}(q^2)}{4\pi^2 \alpha^2} . \quad (30)$$

This allows one to predict the decay rates for the $\tau^\pm \rightarrow \rho^\pm \nu_\tau$ and $\tau^\pm \rightarrow \rho^\pm(1580) \nu_\tau$ channels. The π and K form factors f_π and f_K are related to a_0 and a_0^S , respectively.

There are relations which exist between the various spectral functions, even though SU(3) is not an exact symmetry^{12,45}. These relations take the form of sum rules where one integrates over the q^2 range $0 \rightarrow \infty$. The first set of relations, due

Table 19. The hadronic spectral functions which govern the decays of the τ lepton into various quantum states.

Hadronic Spectral Functions	
Spectral Function	Particle States
v_1	$\rho(770), \rho(1570)$
a_1	$A_1(1300)$
a_0	$\pi, \pi(1300)$
v_1^S	$K^*(890)$
a_1^S	$Q_1(1280), Q_2(1400)$
v_0^S	$\kappa(1350)$
a_0^S	K

to Weinberg⁴⁶, relate the v_1 and a_1 spectral functions:

$$\int_0^{\infty} [v_1(q^2) - a_1(q^2)] dq^2 = 2\pi f_\pi^2$$

$$\int_0^{\infty} q^2 [v_1(q^2) - a_1(q^2)] dq^2 = 0 .$$
(31)

If delta functions are assumed for the spectral functions

$$v_1(q^2) = 2\pi \frac{f_\rho^2}{m_\rho^2} \delta(q^2 - m_\rho^2)$$

and

$$a_1(q^2) = 2\pi \frac{f_A^2}{m_A^2} \delta(q^2 - m_A^2)$$

then one finds $f_A^2 = f_\rho^2$. The second set of relations, due to Das, Mathur, and Okubo³⁴ relate v_1^S , a_1^S , and v_1 :

$$\begin{aligned} \int_0^\infty [v_1^S(q^2) - a_1^S(q^2)] dq^2 &= 2\pi f_K^2 \\ \int_0^\infty [v_1(q^2) - v_1^S(q^2)] dq^2 &= 0 \\ \int_0^\infty q^2 [v_1^S(q^2) - a_1^S(q^2)] dq^2 &= 0 \end{aligned} \quad (32)$$

These imply, assuming δ function contributions from the Q , K^* , and ρ , that

$$\frac{f_\rho^2}{m_\rho^2} = \frac{f_{K^*}^2}{m_{K^*}^2} = \frac{f_Q^2}{m_{K^*}^2} .$$

Thus, if the decay rate of the reaction $\tau^\pm \rightarrow \rho^\pm \nu_\tau$ is given by¹²

$$\Gamma(\tau^\pm \rightarrow \rho^\pm \nu_\tau) = \frac{G^2 m_\tau^3}{2^6 \pi^2} \cos^2 \theta_c m_\rho^2 \left(1 - \frac{m_\rho^2}{m_\tau^2}\right)^2 \left(1 + \frac{2m_\rho^2}{m_\tau^2}\right)$$

then the decay rates for the reactions $\tau^\pm \rightarrow K^{*\pm}(890)\nu_\tau$ and $\tau^\pm \rightarrow Q^\pm(1300)\nu_\tau$ are given by

$$\begin{aligned} \Gamma(\tau^\pm \rightarrow K^{*\pm}(890)\nu_\tau) &= \frac{G^2 m_\tau^3}{2^6 \pi^2} \sin^2 \theta_c m_\rho^2 \left(1 - \frac{m_{K^*}^2}{m_\tau^2}\right)^2 \left(1 + \frac{2m_{K^*}^2}{m_\tau^2}\right) \\ \Gamma(\tau^\pm \rightarrow Q^\pm(1300)\nu_\tau) &= \frac{G^2 m_\tau^3}{2^6 \pi^2} \sin^2 \theta_c m_\rho^2 \frac{m_{K^*}^2}{m_Q^2} \left(1 - \frac{m_{K^*}^2}{m_\tau^2}\right)^2 \left(1 + \frac{2m_{K^*}^2}{m_\tau^2}\right) \end{aligned} \quad (33)$$

Finally, the branching ratios are related by :

$$\begin{aligned}
b(\tau^\pm \rightarrow K^{*\pm}(890)\nu_\tau) &= b(\tau^\pm \rightarrow \rho^\pm \nu_\tau) \cdot \tan^2 \theta_c \cdot \frac{\left(1 - \frac{m_{K^*}^2}{m_\tau^2}\right)^2 \left(1 + \frac{2m_{K^*}^2}{m_\tau^2}\right)}{\left(1 - \frac{m_\rho^2}{m_\tau^2}\right)^2 \left(1 + \frac{2m_\rho^2}{m_\tau^2}\right)} \\
b(\tau^\pm \rightarrow Q^\pm(1300)\nu_\tau) &= b(\tau^\pm \rightarrow \rho^\pm \nu_\tau) \cdot \tan^2 \theta_c \cdot \frac{\left(1 - \frac{m_Q^2}{m_\tau^2}\right)^2 \left(1 + \frac{2m_Q^2}{m_\tau^2}\right)}{\left(1 - \frac{m_\rho^2}{m_\tau^2}\right)^2 \left(1 + \frac{2m_\rho^2}{m_\tau^2}\right)} \cdot \frac{m_{K^*}^2}{m_Q^2} .
\end{aligned} \tag{34}$$

This thesis has presented measurements of the channels $\tau^\pm \rightarrow K^\pm \nu_\tau + n\pi^0$ $n > 0$, $\tau^\pm \rightarrow K^\pm \pi^+ \pi^- \nu_\tau (\pi^0)$, and $\tau^\pm \rightarrow K^+ K^- \pi^\pm \nu_\tau$. The first of the above decay modes is inclusive and is a combination of several channels. It is expected that this channel will be dominated by the decay $\tau^\pm \rightarrow K^{*\pm}(890)\nu_\tau$ but will also contain a small fraction of the decay $\tau^\pm \rightarrow Q^\pm(1300)\nu_\tau$. It is possible to infer a measurement of the $\tau^\pm \rightarrow K^{*\pm}(890)\nu_\tau$ branching ratio by subtracting the measured contribution from the $\tau^\pm \rightarrow Q^\pm(1300)\nu_\tau$ channel. To do this it is necessary to use the relative rates for the decays $Q \rightarrow K\pi\pi(\pi^0)$ and $Q \rightarrow K^\pm + n\pi^{0'}$ s and also the branching ratios for the decays $\rho(1580) \rightarrow K^+ K^- \pi$ and $\rho(1580) \rightarrow K^- + n\pi^{0'}$ s. These processes are well measured⁴⁷ and given by:

$$\begin{aligned}
b(Q \rightarrow K\pi\pi(\pi^0)) &= 33.0\% \\
b(Q \rightarrow K + n\pi^{0'}s) &= 13.1\% \\
b(\rho(1580) \rightarrow K\pi\pi(\pi^0)) &= 33.0\% \\
b(\rho(1580) \rightarrow K + n\pi^{0'}s) &= 22.0\%
\end{aligned} \tag{35}$$

where, in the case of the Q , the values for the Q_1 resonance were assumed (if instead, the values for the Q_2 are assumed, it does not change the result significantly) and in the case of the ρ' , the K_L^0 particles are not observed in the apparatus. The expected amount of background to the $\tau^\pm \rightarrow K^{*\pm}(890)\nu_\tau$ channel is shown in Table 20.

Table 20- The background sources which are subtracted from the $\tau^\pm \rightarrow K^\pm \nu_\tau + n\pi^0$ measured signal to find the $\tau^\pm \rightarrow K^{*\pm}(890)\nu_\tau$ branching ratio.

K^* Backgrounds in the $\tau^\pm \rightarrow K^\pm \nu_\tau + n\pi^0$ Channel		
Source	Subtraction	
	Q_1	Q_2
Q	$(0.087 \pm 0.055)\%$	$(0.054 \pm 0.034)\%$
$\rho(1580)$	$(0.054 \pm 0.034)\%$	
total	$(0.23 \pm 0.11)\%$	$(0.20 \pm 0.10)\%$

The K^* branching ratio is then given by the relation:

$$\begin{aligned}
 b(\tau^\pm \rightarrow K^{*\pm}(890)\nu_\tau) &= \left(b(\tau^\pm \rightarrow K^\pm \nu_\tau + n\pi^0, (n > 0)) - \right. \\
 &\quad \left. b(\tau \rightarrow Q \text{ or } \rho') \rightarrow K\nu_\tau + n\pi^{0's}) \right) \\
 &\quad \times \frac{1}{b(K^* \rightarrow K^-\pi^0)} \\
 &= (2.67 \pm 0.37)\%
 \end{aligned} \tag{36}$$

which assumes that the Q decay proceeds via the Q_1 channel and uses the measured value $b(\tau^\pm \rightarrow K^\pm \nu_\tau + n\pi^0, n > 0) = (1.12 \pm 0.34)\%$. The predicted branching ratio from Equation 36 is $(1.02 \pm 0.16)\%$ where the measured branching ratio for the decay $\tau^\pm \rightarrow \rho^\pm \nu_\tau$ of $(22.1 \pm 2.4)\%$ was used.

The results of the branching ratio measurements are shown in Table 21 along with the theoretical predictions. The agreement is fairly good except in the case of the K^* decay. It is evident that there is room for another source of $\tau^\pm \rightarrow K^\pm \nu_\tau + n\pi^0$. The logical channel would be the $\tau \rightarrow \kappa(1350)\nu_\tau$ decay through the s-wave channel. However the significance of this result does not warrant a definitive assignment.

Table 21. The branching ratios for multiparticle decay modes of the τ containing charged kaons. The channels were assumed to be dominated by the resonant states $K^*(890)$, q , and $\rho(1580)$.

Resonance Branching Ratios		
Mode	Measured	Predicted
$\tau^\pm \rightarrow K^{*\pm}(890)\nu_\tau$	$(2.67 \pm 0.63)\%$	$(1.11 \pm 0.12)\%$
$\tau^\pm \rightarrow Q^\pm(1300)\nu_\tau$	$(0.22^{+0.16}_{-0.13})$	$(0.11 \pm 0.02)\%$
$\tau^\pm \rightarrow \rho^\pm(1580)\nu_\tau$	$(0.22^{+0.17}_{-0.11})$	$(0.24 \pm 0.03)\%$

§5.3 The τ Neutrino Mass

In this section the τ neutrino mass measurement is discussed. In the analysis of the τ neutrino mass limit in the previous chapter a model was used to describe the expected decay rate for the decay $\tau^\pm \rightarrow K^+K^-\pi^\pm\nu_\tau$. This is next pursued in more detail. Following this, the implications of a massive neutrino in experimental physics and in the context of astrophysics are touched on.

§§5.3.1 The $\tau^\pm \rightarrow K^+K^-\pi^\pm\nu_\tau$ Decay

The decay $\tau \rightarrow \rho(1580)\nu_\tau \rightarrow K^+K^-\pi\nu_\tau$ can be calculated, as mentioned in Chapter 2, by using the CVC assumption which has been verified in the decay

$\tau^\pm \rightarrow \rho^\pm \nu_\tau$. CVC relates the cross section for $e^+e^- \rightarrow \rho(1580)$ to the decay $\tau^\pm \rightarrow \rho^\pm \nu_\tau$. Figure 52 shows how the various components of the amplitudes are related. In making this comparison it is necessary to use the $I=1$ part of the $\sigma_{e^+e^-}$ cross section only; however, since the isoscalar cross section is relatively small, it is not a serious problem. The relation is given by:

$$\begin{aligned} \Gamma(\tau \rightarrow \rho(1580)) &= \frac{G^2 \cos^2 \theta_c}{96\pi^3 m_\tau^3} \int_0^{(m_\tau^2 - m_{\nu_\tau}^2)} dq^2 \\ &\times [m_\tau^4 + m_{\nu_\tau}^4 + q^4 - 2m_{\nu_\tau}^2 m_\tau^2 - 2m_{\nu_\tau}^2 q^2 - 2m_\tau^2 q^2]^{\frac{1}{2}} \\ &\times [m_\tau^4 + m_{\nu_\tau}^4 - 2q^4 - 2m_{\nu_\tau}^2 m_\tau^2 + m_{\nu_\tau}^2 q^2 + m_\tau^2 q^2] \\ &\times \frac{\sigma_{e^+e^-}^{I=1}(q^2)}{\sigma_{e^+e^-}^{\mu^+\mu^-}}. \end{aligned} \quad (37)$$

The cross section $\sigma_{e^+e^-}^{I=1}$ can be represented as a modified Breit-Wigner for the $\rho(1580)$ which takes into account the phase space threshold for the $K^*\bar{K}$ system:

$$\sigma(e^+e^- \rightarrow K^*\bar{K})(q^2) = 12\pi \frac{\Gamma_{\rho'ee} \Gamma_{\rho'K^*\bar{K}}(q^2)}{(q^2 - m_{\rho'}^2)^2 + \Gamma_{\rho'}^2 m_{\rho'}^2} \quad (38)$$

where

$$\begin{aligned} \Gamma_{\rho'K^*\bar{K}}(q^2) &= N \times \frac{\pi^2}{4q^2} \int_{(m_K + m_\pi)^2}^{(q - m_K)^2} \frac{ds_2}{s_2} \times \\ &[(s_2 - q^2 - m_K^2)^2 - 4q^2 m_K^2]^{\frac{1}{2}} [(s_2 - m_\pi^2 - m_K^2)^2 - 4m_\pi^2 m_K^2]. \end{aligned} \quad (39)$$

The normalization, N , is obtained by integrating $\sigma_{e^+e^-}^{I=1}$ over the range of the $\rho(1580)$ resonance and setting the branching ratio for the $\rho \rightarrow K^*\bar{K}$ decay equal to the measured⁴⁷ value of $(9 \pm 1)\%$.

$$\int \sigma(e^+e^- \rightarrow K^*\bar{K})(q^2) dq^2 = 12\pi^2 \Gamma_{\rho'ee} \Gamma_{\rho'} \times b(\rho' \rightarrow K^*\bar{K})$$

The $\sigma_{e^+e^-}$ cross sections were obtained from the ORSAY results¹⁶ which unfolded the I=1 channel of the $K^*\bar{K}$ cross section from the I=0 isoscalar component. These measurements have been available only in the last few years.

The result of the decay rate calculation is shown in Figure 53. The two distributions in this figure show the difference between a three-body phase space assumption for the $KK\pi$ system and the assumption of the $\rho(1580)$ dominance as predicted by CVC. These are each shown for varying values of m_{ν_τ} .

The likelihood fit for the τ neutrino mass uses this decay rate, after being smeared with the detector resolution. The model dependence of the fit has been checked by performing the fit using both the phase space model and the $\rho(1580)$ dominance. The neutrino mass limit is sensitive, being $139 \text{ MeV}/c^2$ at 95 CL, in the case of the phase space model and $157 \text{ MeV}/c^2$ at 95 CL, in the case of the $\rho(1580)$ model. The most conservative limit is the limit which uses the $\rho(1580)$ dominance model, which is also favored on the basis of the CVC hypothesis.

§§5.3.2 *Cosmological Implications*

The importance of neutrinos in the evolution of the universe has been known for some time. The masses of neutrinos play a crucial role in the early universe and can have drastic effects on the outcome of the Big Bang. Of course the outcome is well known; thus, knowledge about neutrino properties merely provides insight into the development of the early universe.

There are several properties which are known about the neutrinos today but much information is missing. It is known that there are at least three neutrinos

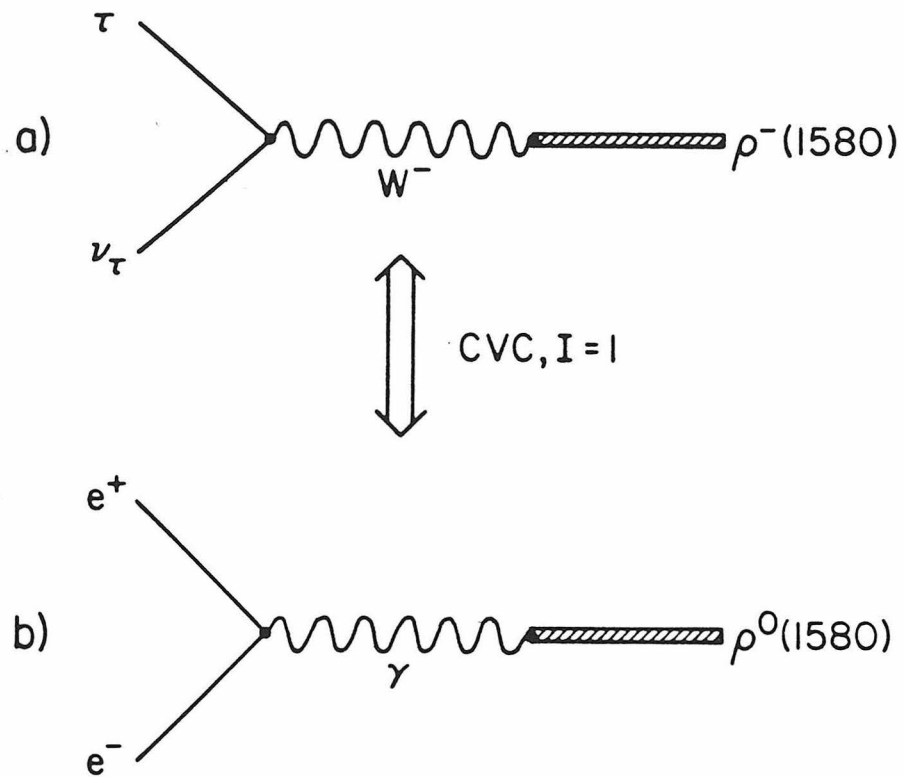


Figure 52. The CVC hypothesis relates the $I = 1$ channel of e^+e^- scattering into hadrons to the isovector decay amplitude in τ decay. As can be seen in the above diagrams the substitution of the e^+e^- current and the γ in the first diagram by a $\tau\nu_\tau$ current and W^- and rotating the isospin of the hadronic system from $I_z = 0$ to $I_z = -1$ turns the first diagram into the second.

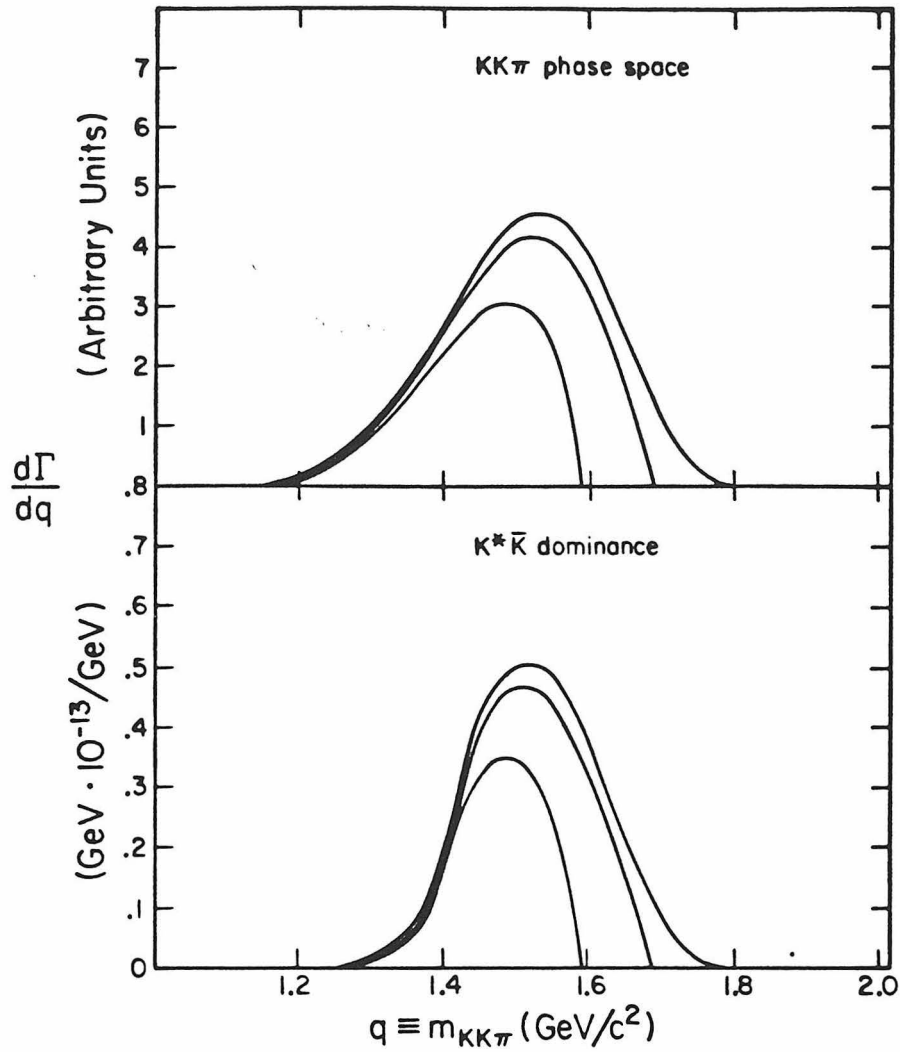


Figure 53. The decay of the τ into $KK\pi\nu_\tau$ is predicted to proceed through the intermediate channel $K^*\bar{K}$ as is seen in $e^+e^- \rightarrow \text{hadrons}$. The effect of this assumption is compared to a pure phase space distribution for the $KK\pi$ system and is shown in this figure. The decay rate for several neutrino mass assumptions is shown for each case.

corresponding to the three known leptons: ν_e , ν_μ , and ν_τ . It is also known that the neutrinos interact with the standard weak interactions so that their decays may be predicted. However, the question of whether the neutrinos are Dirac or Majorana particles is still open. It is also not known whether the neutrinos are massive, and the amount of mixing between the the three neutrino species is still an unknown.

There are many models of the evolution of the universe and, to make the argument concrete, a particular viewpoint will be followed here in discussing the implications of both particle physics and cosmology on bounds of the τ neutrino mass and lifetime. The arguments presented here follow the work of Ref. 48 where the same arguments are presented in much more detail.

§§§5.3.2.1 *Neutrino Decays*

The decays of neutrinos depend upon several parameters. Assuming lepton number conservation but not necessarily individual $e - \mu - \tau$ lepton number conservation it is possible to have decays if the neutrinos both mix and have mass⁴⁹. There are two regimes for standard weak neutrino decay processes. The first is when the mass of the neutrino is less than twice the mass of the electron, $m_{\nu_\tau} \leq 2m_e$. In this case the two dominant decay mechanisms are the radiative decays $\nu_\tau \rightarrow \nu\gamma$ and $\nu_\tau \rightarrow \nu\gamma\gamma$. These decays are suppressed because of a GIM like mechanism in the first case and in the second case the diagrams are of higher order. These decays lead to very long lifetimes. The second case is when $m_{\nu_\tau} > 2m_e$. This means that the τ neutrino may decay via the channel $\nu_\tau \rightarrow e^+e^-\nu$ which is a first-order weak decay and hence has a relatively short lifetime compared to the radiative decays. The

diagrams for these decays are shown in Figure 54. The consequences of having such a short neutrino lifetime on the development of the early universe can be dramatic and are discussed next.

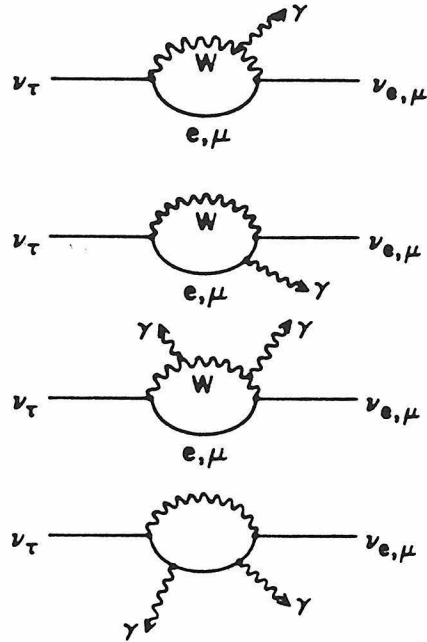
§§§5.3.2.2 *Cosmological Constraints*

There are four main constraints on heavy neutrino masses and lifetimes in cosmology. These have all been discussed in various places^{48,50,51,52}. The first constraint is that no stable neutrino can exist with a mass greater than 100 eV. This is because of the observed limit on dark matter in the universe which has been obtained by studying galaxy and other cosmological dynamics. Additional heavy neutrinos ($m_\nu > 100eV$) would make the universe too dense to be compatible with observations.

The second constraint is from the abundance of deuterium (D) and helium (4He) found in the universe today. If a heavy neutrino were to decay after the formation of D and 4He , then the high energy photons produced in the decay will cause the photofission of D and 4He to occur, thus depleting them to levels below that which are presently observed. Since the lifetime depends on the mass, of the neutrino the constraint thus imposed is a function of both the mass and the lifetime of the neutrino. Figure 55 shows the regions which are allowed by these constraints on the mass and lifetime of ν_τ .

The third constraint comes from the effects that a decaying neutrino has on the synthesis of nuclei in the early universe. The upper limit on the abundance of 4He observed today is related to the temperature of the universe at the time

a) $m_{\nu_\tau} \lesssim 2m_e$:



b) $m_{\nu_\tau} \gtrsim 2m_e$:

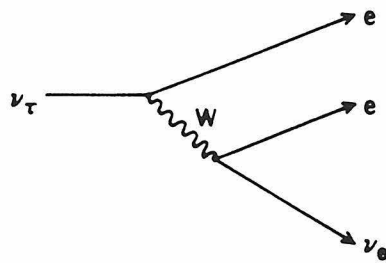


Figure 54. The radiative decays, a), of the neutrino are the only available decay channel if the mass of the neutrino is less than $2m_e$. If the mass of the neutrino is above $2m_e$ then the channel in b) is available and will dominate the decay.

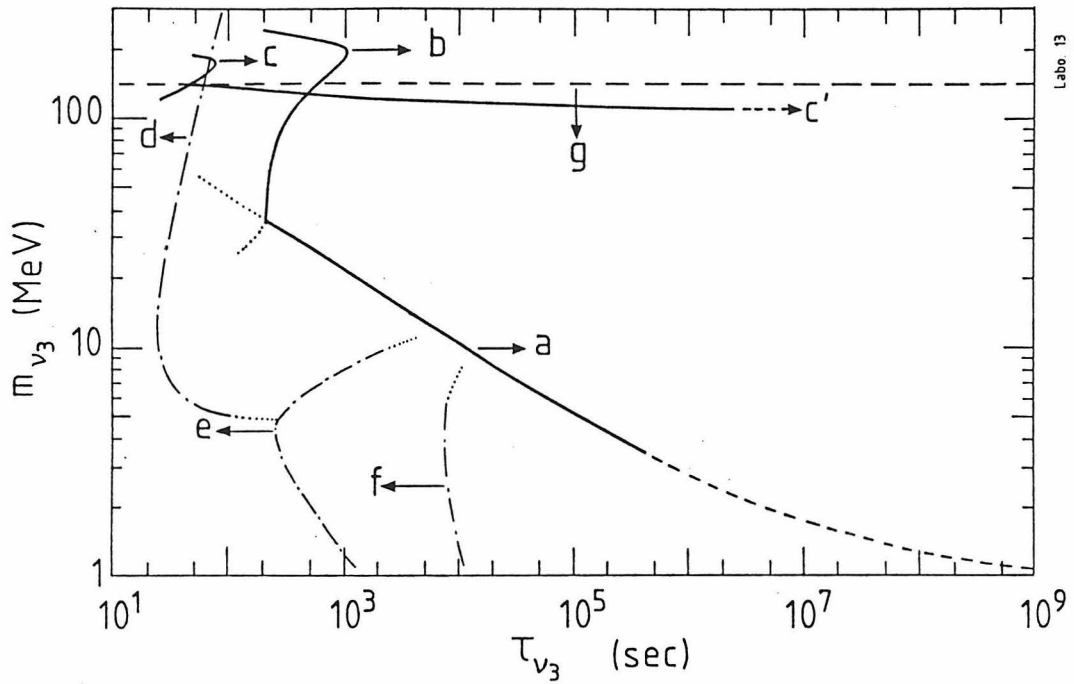


Figure 55. The constraints imposed on the τ neutrino mass and lifetime from particle physics experiments and from cosmological considerations. This figure is reproduced from Reference 48. The allowed region is illustrated by the arrows.

- a) $\frac{\pi \rightarrow e\nu_e}{\pi \rightarrow \mu\nu_\mu}$
- b) $\nu_\tau \rightarrow e^+e^-$, decay in flight
- c) $\nu_\tau \rightarrow \mu e\nu$, neutrino interactions
- c') $K \rightarrow \pi\nu$, peak search
- d) Deuterium photofission
- e) Primordial Nucleosynthesis
- f) Blackbody Background Radiation Distribution
- g) Mass limit on m_{ν_τ}

at which the neutrino decays, and hence is related to the time at which the decay occurs. This then limits both the lifetime and the mass of the τ neutrino.

The fourth cosmological constraint comes from the shape of the observed blackbody background radiation observed today. If a heavy neutrinos had decayed late enough the energy transferred to the photon spectrum would have severely distorted it from the present spectrum. The constraints imposed on the mass and lifetime by these arguments are shown in Figure 55.

There are also results from particle physics experiments which limit the lifetime and mass of the τ neutrino. These are also shown in Figure 55.

The end result of these limits is that it is most likely, accepting these arguments, that m_{ν_τ} is less than $1 \text{ MeV}/c^2$ (with the caveat that the decay $\nu_\tau \rightarrow \mu e \nu$ is unlikely but not completely ruled out). With a mass this low, the available decay channels give ν_τ a very long lifetime since the radiative decay modes are unable to generate a short enough lifetime. This means that the τ neutrino falls under the shadow of the dark matter limit of 100 eV . So one may conclude that, given all the above arguments, $m_{\nu_\tau} < 100 \text{ eV}$. This conclusion is not substantiated on firm experimental grounds, however, in the context of cosmology and the Big Bang, it has important implications.

§5.4 Conclusion

In conclusion, the decays of the τ neutrino which contain charged kaons have been studied by using the DELCO apparatus at the PEP e^+e^- storage ring. This apparatus uses a large solid angle coverage isobutane gas threshold Cherenkov counter to identify charged kaons from τ decays. The measurement of the branching ratio of the decay $\tau^\pm \rightarrow K^\pm \nu_\tau$ lead to an important test of $e - \mu - \tau$ universality. The measurement of the branching ratios of multihadronic decays of the τ showed agreement with theoretical expectations employing SU(3) symmetry sum rules. The use of exclusive $\tau^\pm \rightarrow K^+ K^- \pi^\pm \nu_\tau$ events allowed the determination of an upper bound on the mass of the τ neutrino.

Appendix A.

This appendix gives a summary of the theoretical treatment of the production and decay of $\tau^+\tau^-$ pairs in high energy e^+e^- collisions. The results are taken from several references ^{12,15,53} .

These results were employed to construct an event generator which was used to calculate the efficiencies for the results in this thesis. The generator proved versatile and useful for understanding the aspects of the analysis.

§A.1 $\tau^+\tau^-$ Production

At PEP energies of $14.5 \text{ GeV}/c^2$ $\tau^+\tau^-$ pairs are produced dominantly through a virtual photon with a small extra contribution due to interference of the photon with the weak neutral vector boson, Z_0 . PEP also ran with unpolarized beams so that the cross section must be averaged over initial spin states.

The differential cross section for the process $e^+e^- \rightarrow \tau^+\tau^-$ is a function of the polarization vector of the two τ 's (ϵ^\pm) in their rest frames, the direction of the τ^- in the lab system (CM system of the initial e^+e^-), and the center of mass energy

\sqrt{s} . It is given by

$$\frac{d\sigma_{\tau^+\tau^-}}{d\Omega} = \frac{\alpha^2}{16s} \beta_\tau \left[(1 - rg_V^2)t_1 + rg_V g_A(t_3 - t_4) + rg_A^2 t_2 \right] \quad (40)$$

where

$$\begin{aligned} t_1 &= 1 + \cos^2\theta + \frac{\sin^2\theta}{\gamma^2} \\ &\quad + \epsilon_x^- \epsilon_z^+ \left[1 + \cos^2\theta - \frac{\sin^2\theta}{\gamma^2} \right] \\ &\quad + \epsilon_x^- \epsilon_x^+ \left(1 + \frac{1}{\gamma^2} \right) \sin^2\theta - \epsilon_y^- \epsilon_y^+ \beta^2 \sin^2\theta \\ &\quad - (\epsilon_x^- \epsilon_z^+ + \epsilon_z^- \epsilon_x^+) \frac{\sin 2\theta}{\gamma} \quad , \\ t_2 &= -2\beta \cos\theta - 2\epsilon_z^- \epsilon_z^+ \beta \cos\theta \\ &\quad (\epsilon_x^- \epsilon_z^+ + \epsilon_z^- \epsilon_x^+) \frac{\beta \sin\theta}{\gamma} \quad , \\ t_3 &= 2(\epsilon_z^- + \epsilon_z^+) \cos\theta - 2(\epsilon_x^- + \epsilon_x^+) \frac{\sin\theta}{\gamma} \quad , \\ t_4 &= -(\epsilon_x^- + \epsilon_x^+) \beta (1 + \cos^2\theta) + (\epsilon_z^- + \epsilon_z^+) \frac{\beta}{2\gamma} \sin 2\theta \quad , \\ r &= \frac{G_F s}{\pi \sqrt{2} \alpha} \frac{1}{1 - \frac{s}{m_Z^2}} \approx 0.337 \quad , \end{aligned} \quad (41)$$

and where $g_V = \frac{1}{2} - 2\sin^2\theta_W$ and $g_A = \frac{1}{2}$. This cross section demonstrates the spin correlation induced by producing the $\tau^+\tau^-$ pair through a spin one intermediate state.

§A.2 The τ Decay Rate

The decay of a polarized τ^- is a quasi-two-body decay. The τ^- decays into a

ν_τ plus another system which has a net charge of -1. This second system may also contain neutrinos if it is a leptonic decay. Since we do not observe the neutrinos it is necessary to integrate the decay rate over their momenta. The result is that all decays of interest can be thought of as producing, from an initial τ^- with polarization vector η_μ and a momentum q_μ , a negatively charged particle of momentum k_μ . This decay rate can be written generally as

$$\frac{q_0^-}{m_\tau} k_0^- \frac{d^3 \Gamma_i}{d^3 k^-} = \Gamma_i C_i^- \left[A_i + B_i (k^- \cdot n^-) \right] \quad (42)$$

where Γ_i is the partial decay rate for the final state i and the A_i^- , B_i^- , and C_i^- are determined by the type of decay. For a positively charged τ the substitutions $A_i^+ = A_i^-$, $B_i^+ = -B_i^-$, and $C_i^+ = C_i^-$ give the appropriate decay rate. For pseudoscalar decays the above constants are given by:

$$\begin{aligned} A^- &= \frac{m_\tau^2 - M^2}{2m_\tau} \delta(m_\tau^2 + M^2 - 2k^- \cdot q^-) \\ B^- &= -\delta(m_\tau^2 + M^2 - 2k^- \cdot q^-) \\ C^- &= \frac{2m_\tau^3}{\pi(m_\tau^2 - m_\pi^2)^2} \end{aligned} \quad (43)$$

where M is the mass of the pseudoscalar (π or K). For vector particles:

$$\begin{aligned} A^- &= \frac{m_\tau^2 - M^2}{2m_\tau} \delta(m_\tau^2 + M^2 - 2k^- \cdot q^-) \\ B^- &= \frac{m_\tau^2 - 2M^2}{m_\tau^2 + 2M^2} \delta(m_\tau^2 + M^2 - 2k^- \cdot q^-) \\ C^- &= \frac{2m_\tau^3}{\pi(m_\tau^2 - m_\pi^2)^2} \end{aligned} \quad (44)$$

where M is the mass of the vector particle, *i.e.* the ρ , A_1 , K^* , or Q . For leptonic

decays, after integrating over the neutrino momentum,

$$\begin{aligned}
 A^- &= -2\eta^2 + 3(1 + 9\eta^2) \frac{k^- \cdot q^-}{m_\tau^2} - 4(1 + 8\eta^2) \left(\frac{k^- \cdot q^-}{m_\tau^2} \right)^2 \\
 B^- &= \frac{1}{m_\tau} \left[-1 - 11\eta^2 + 4(1 + 8\eta^2) \frac{k^- \cdot q^-}{m_\tau^2} \right] \\
 C^- &= \frac{4}{\pi m_\tau^2}
 \end{aligned} \tag{45}$$

where $\eta = \frac{m_l}{m_\tau}$ contains the lepton mass (e or μ). Thus, the differential decay rate of the τ determines the momentum distribution of the charged decay product.

§A.3 Radiative Corrections

Corrections to the cross section for $e^+e^- \rightarrow \tau^+\tau^-$ enter at the several percent level from the process $e^+e^- \rightarrow \tau^+\tau^-\gamma$. The dominant contribution comes from initial state radiation shown in Fig. 56 a) where the incoming electron radiates energy prior to annihilation. There is also a 4% contribution to the total cross section from virtual loop corrections shown in Fig. 56b), which does not change the differential cross section. The diagrams in Fig. 56a) do change the differential cross section, primarily in $\cos \theta$, because the photons are primarily radiated along the beam direction. After selecting the data as in Chapter 4 the net effect is nearly a 10% increase in the product of the cross section and efficiency, depending the specific selection criteria.

The calculation of these corrections has been performed^{54,10} and incorporated into a Monte Carlo event generator. The energy distribution of the radiated photon is shown in Figure 57 where one can see the $\frac{1}{k}$ dependence of the brehmsstrahlung

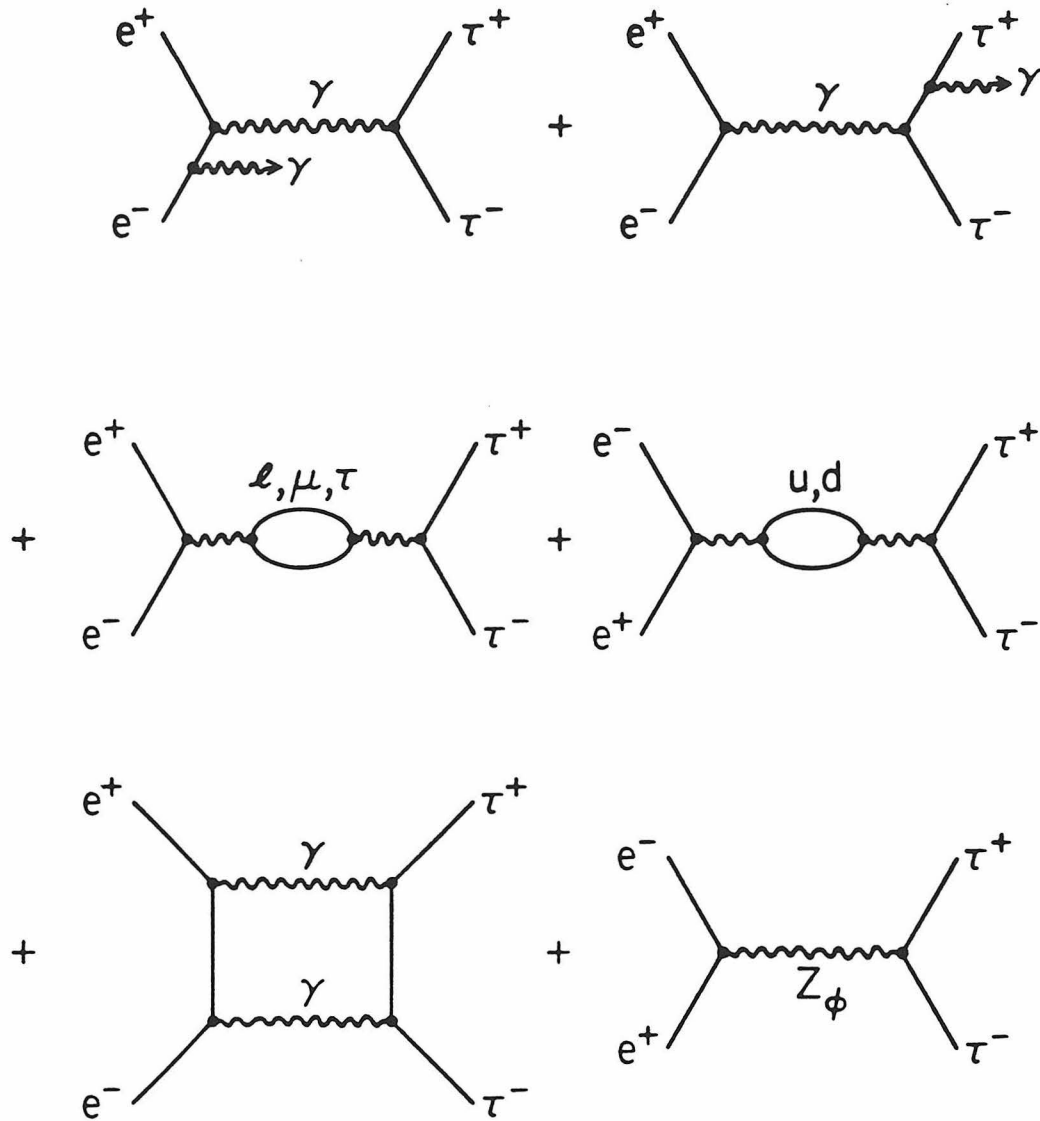


Figure 56. The diagrams which give the dominant contributions to the higher order corrections to the process $e^+e^- \rightarrow \tau^+\tau^-$.

component and also the increase at $E_\gamma \approx E_{beam}$ due to the $\frac{1}{E_\gamma - E_{beam}}$ term in the amplitude.

§A.4 Monte Carlo Event Generation

In order to use the detector simulation to calculate efficiencies an accurate event generator is needed. It must include all processes which affect efficiencies at levels larger than a percent or so. This was also the practical limit on accuracy imposed by the amount of computer time needed to generate Monte Carlo statistics.

Events were generated by first generating a $\tau^+\tau^-$ pair plus a radiated photon using the programs mentioned previously¹⁰. The polarizations of the τ^+ and τ^- were then obtained using Equation 40 at fixed $\cos\theta$. The polarized τ 's are then allowed to decay according to Equation 42. The branching ratios are chosen to agree with the measured values and are shown in Table 22. In the case of the multi-prong decays that do not proceed via a vector resonance, a multibody S-wave phase space distribution is used for the decay.

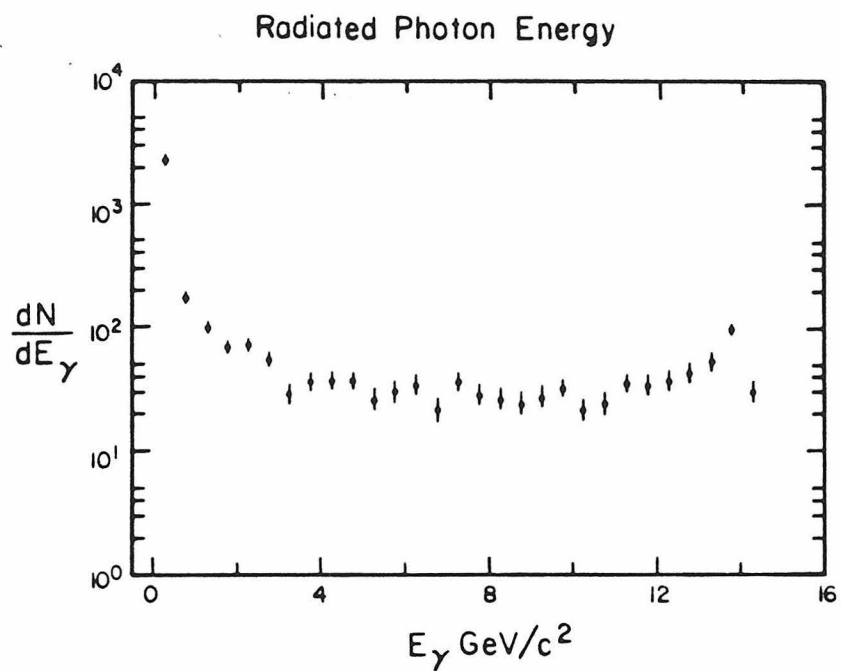


Figure 57. The calculated energy distribution of radiated photons from the reaction $e^+e^- \rightarrow \tau^+\tau^-\gamma$.

Table 22. The branching ratios used in generating Monte Carlo events used in calculating event efficiencies.

Branching Ratios Used MC Event Generation	
Decay Mode	Generated Branching Ratio
$\tau^\pm \rightarrow e^\pm \bar{\nu}_e \nu_\tau$	17.7%
$\tau^\pm \rightarrow \mu^\pm \bar{\nu}_\mu \nu_\tau$	17.2%
$\tau^\pm \rightarrow \pi^\pm \nu_\tau$	10.9%
$\tau^\pm \rightarrow \rho^\pm \nu_\tau$	22.3%
$\tau^\pm \rightarrow A_1^\pm \nu_\tau$	15.1%
$\tau^\pm \rightarrow K^\pm \nu_\tau$	0.52%
$\tau^\pm \rightarrow K^{*\pm}(890) \nu_\tau$	1.0%
$\tau^\pm \rightarrow Q^\pm(1300) \nu_\tau$	0.76%
$\tau^\pm \rightarrow \pi^\pm 3\pi^0 \nu_\tau$	6.0%
$\tau^\pm \rightarrow \pi^\pm 4\pi^0 \nu_\tau$	0.5%
$\tau^\pm \rightarrow 3\pi^\pm \pi^0 \nu_\tau$	6.9%
$\tau^\pm \rightarrow 3\pi^\pm 2\pi^0 \nu_\tau$	0.5%
$\tau^\pm \rightarrow 5\pi^\pm \nu_\tau$	0.5%

REFERENCES

1. M. Perl et al., Phys. Rev. Lett. 35:1489, 1975
2. S. Herb et al., Phys. Rev. Lett. 39:252, 1977
3. M. Perl, Ann. Rev. Nucl. Part. Sci. 30:299, 1980
4. With the exception of the TASSO detector, which had a limited solid angle coverage Cherenkov counter system with a substantial amount of material in front of the Cherenkov apparatus. This made it an inefficient counter system.
5. C. Blocker et al., Phys. Rev. Lett. 48:1586, 1982
6. V. Lubimov et al., Int. Conf. HEP: Brighton, 386-390, 1983
7. W. Bacino et al., Phys. Rev. Lett. 42:749, 1979
8. see B. Wiik and G. Wolf, *Electron-Positron Interactions*, Berlin, Germany, Springer-Verlag, 1979 for a review of older e^+e^- physics
9. F. Berends et al., Nuc. Phys. B68:541, 1974
10. R. Kleiss, Ph.D. thesis, Leiden preprint RX-988, 1982
11. L. Michel, Proc. Phys. Soc.(London) A63:514, 1950
12. Y. Tsai, Phys. Rev. D4:2821, 1971
13. J. Dorfan et al., Phys. Rev. Lett. 46:215, 1981
14. for a review see W. Ruckstuhl, Caltech preprint: CALT-68-1232 1985
15. F. Gilman & S. Rhie, SLAC-PUB-3444, 1984, F. Gilman & D. Miller. Phys. Rev. D17:1846, 1978
16. B. Delcourt et al., Proceedings of the Lepton Photon Symposium, Bonn, p.205, 1981
17. R. Mohapatra and G. Senjanovic, Phys. Rev. D23:165, 1981
18. see T. Sjostrand, Comput. Phys. Commun. 28:229, 1983
19. M. Sands, SLAC-PUB-0121, 1970
20. R. Helms et al., SLAC-PUB-3070, 1983
21. W. Herrmannsfeldt, SLAC-TN-65-055, 1965 and R. Early, *A Users Guide to POISSON*, PEP-0326(SLAC), 1979
22. C. Prescott, private communication.

23. D.E. Koop, PhD Thesis, Caltech, CALT-68-1149, 1984
24. W. Bacino, PhD Thesis, UCLA, UCLA-A-2000
25. B. Rossi, *High Energy Particles*, Prentice-Hall, N.Y., 1952
26. G. Abshire et al., Nucl. Inst. Meth. 164:67, 1979
27. H.J. Bhabha, Proc. Roy. Soc. (London) A154:195, 1935
28. Rev. Mod. Phys. V56 No.2, Part II, p.S48
29. Jelley, *Cherenkov Radiation*, 1958, Pergamon Press
30. The thrust, T , and the thrust axis, \mathbf{n} , are defined by the relation:

$$T = \text{MAX} \sum_{\text{tracks } i} \frac{|\mathbf{p}_i \cdot \mathbf{n}|}{|\mathbf{p}_i|}$$

where the maximum is over all possible directions \mathbf{n} .

31. J.M.Dorfan *et al.*, Phys. Rev. Lett. 46:215, 1981
32. G.B.Mills *et al.*, CALTECH preprint, CALT-68-1196, 1984
33. MINUIT: a standard function minimization program, see Computer Physics Communications 10:343, 1975
34. T. Das, et al., Phys. Rev. Lett. 18:761, 1967
35. Ayres et al., Phys.Rev. D3:1051, 1971
36. Bryman et al., Phys. Rev. Lett. 50:7, 1983
37. Rev. Mod. Phys. 5B:510, 1984
38. A. Ott et al., Phys. Rev. D3:52, 1969
39. Chaing et al., Phys. Rev. D6:1254, 1972
40. J. Heintze et al., Phys. Lett. 60B:302, 1976
41. F. Berends et al., Phys. Lett. 127B:270, 1983
42. C. Blocker et al., 109B:119, 1982
43. G. Mills et al., Phys. Rev. Lett. 52:1944, 1984
44. J. Jaros et al., SLAC-PUB-3569, 1984
45. G. Aubrecht et al., Phys. Rev. D24:1318, 1981
46. S. Weinberg, Phys. Rev. Lett. 18:507, 1967

47. Rev. Mod. Phys. 56:S18, 1984
48. S. Sarkar and A. Cooper, CERN/EP 84-97, 1984
49. R. Shrock, Phys. Rev. D24:1232, 1981
50. S. Gershtein and Y. Zeldovich, JETP Lett. 4:120, 1966
51. R. Cowsic and J. McClelland, Phys. Rev. Lett. 29:669, 1972
52. D. Dicus, E. Kolb, and V. Teplitz, Phys. Rev. Lett. 39:168, 1977
53. H. Dahmen et al., Z. Physik C5:71, 1980
54. F. Berends et al., Nuclear Physics B177:237, 1981